CARBON AND NITROGEN IN EARTH AND PLANETARY INTERIORS

By

Mingda Lyu

A DISSERTATION

Submitted to
Michigan State University
in partial fulfillment of the requirements
for the degree of

Geological Sciences—Doctor of Philosophy

2021

ABSTRACT

CARBON AND NITROGEN IN EARTH AND PLANETARY INTERIORS

By

Mingda Lyu

Volatile elements, such as carbon (C) and nitrogen (N), play an essential role on Earth in forming living organisms, maintaining a habitable climate, tracing geological processes, and powering the core dynamo. Constraining the distribution and budgets of volatile elements on terrestrial planets, such as the Earth and Mars, holds the key to understanding their formation, evolution, dynamics, and habitability. In this dissertation, I performed a series of experiments to investigate the physical properties and chemical behavior of carbonates and iron nitrides at high pressure and temperature conditions to decipher the role of carbon and nitrogen in the Earth and planetary deep interior.

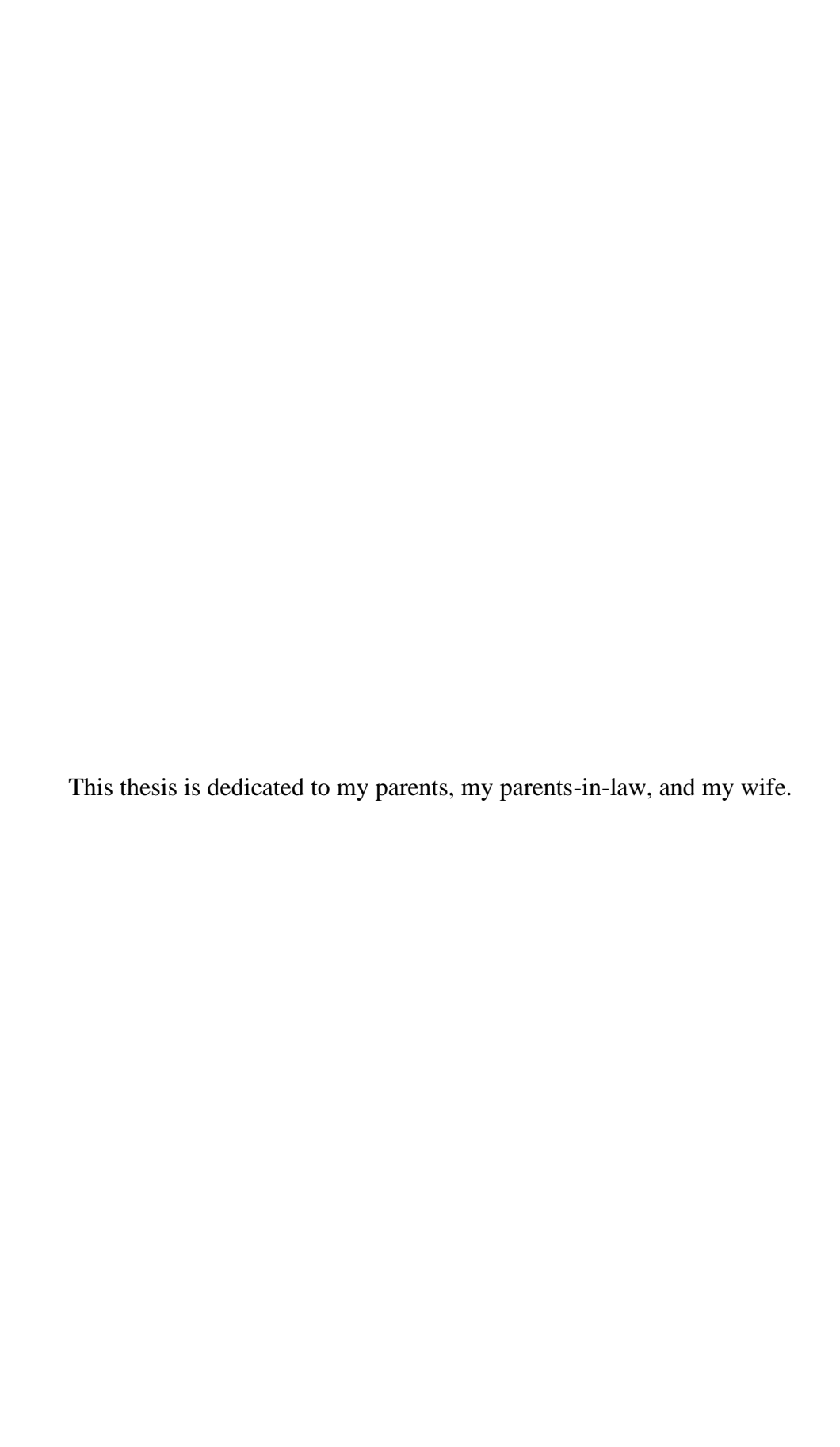
The circulation of carbon between reservoirs on Earth's surface and interior is the key to governing long-term atmospheric CO₂ budget. Carbonates, including calcite (CaCO₃), magnesite (MgCO₃), and dolomite (CaMg(CO₃)₂, are believed to be the major carriers to transport surface carbon to the Earth's mantle at subduction zones. However, the global carbon flux to the convecting lower mantle and the stable format of carbon at mantle conditions remain largely uncertain, due to lack of constraints on thermodynamic properties of subducted carbonates and limited understanding of the fate of carbonates through subduction. In chapter 2, I measured the thermal equation of state of CaCO₃-Pmmn, a stable polymorph of CaCO₃ through much of the lower mantle, using synchrotron X-ray diffraction in a laser-heated diamond-anvil cell up to 75 GPa and 2200 K. Using the newly determined thermodynamic parameters, I modeled the physical properties of CaCO₃-Pmmn and (Ca,Mg)-carbonate-bearing eclogite, showing the presence of

carbonates in the subducted slab is unlikely to be detected by seismic observations, and the buoyancy provided by carbonates has a negligible effect on slab dynamics. In chapter 3, I examined the stability of MgCO₃ and CaCO₃ coexisting with the mantle silicates along mantle geotherm. With in-situ X-ray diffractions and ex-situ electron microscopic analysis, I showed if CaCO₃ can be transported to the deep lower mantle and even the core-mantle boundary, it can remain stable and coexist with the mantle silicates, while MgCO₃ can only be stable at depth above ~1850 km. The observations indicate CaCO₃ the dominant host of oxidized carbon at the coremantle boundary.

The presence of light elements in the core are inferred by seismic and cosmochemical observations, and possible light elements are narrowed to Si, O, S, C, H. Recently, nitrogen has been added to the candidates' list, and thus iron nitrides are possible constituents in the Earth's and other terrestrial planet cores. However, the physical properties, especially pressure-induced magnetic changes and effects on compressibility of iron nitrides remain poorly understood. In chapter 4, I constrained the magnetic transition pressure and the equation of state of ε -Fe₇N₃ and γ '-Fe₄N up to 60 GPa at 300 K, indicating the completion of magnetic transition induces elastic stiffening in ε -Fe₇N₃ by 22% at ~40 GPa, but has no resolvable effect on the compression behavior of γ '-Fe₄N. I re-examined evidence for magnetic transition and effects on compressibility of other candidate components of terrestrial planet cores, Fe₃S, Fe₃P, Fe₇C₃, and Fe₃C, showing the completion of magnetic transition of Fe₃S, Fe₃P and Fe₃C induces elastic stiffening, whereas that of Fe₇C₃ induces elastic softening.

To sum up, this dissertation expands our understanding on the role of carbon and nitrogen in the properties of Earth and planetary interiors, by revealing the stability and fate of carbonate subducted to the lower mantle and the physical properties iron nitrides.

Copyright by MINGDA LYU 2021



ACKNOWLEDGEMENTS

First and foremost, I am tremendously grateful to my advisor, Prof. Susannah Dorfman, who introduced me to interdisciplinary research on Earth's lower mantle from the perspectives of geophysics, geochemistry, and geodynamics. Prof. Dorfman trained me on how to conduct high-quality experiments, helped me to improve my writing and presentation skills, and provided a lot of advice on my career development. None of the work described in this dissertation could have been accomplished without the guidance and support of my advisor. I am deeply appreciative to my advisory committee, Profs. Allen McNamara, Tyrone Rooney, Matthew Schrenk, who pointed out my knowledge gap and weakness, and gave me conscientious suggestions from various perspectives throughout my journey. I am sincerely thankful for the inspiring and fruitful discussions in journal clubs, particularly with Profs. Min Chen, Jeffrey Freymueller, Dalton Hardisty, Seth Jacobson, Kevin Mackey, Michael Velbel, Songqiao Wei, and Warren Wood. I feel fortunate to work under the supervision of these brilliant mentors in our department.

I extremely appreciate my collaborators, in particular Drs. James Badro, Jie Li, Jiachao Liu, and Feng Zhu, who have been played an essential role in my research, gave me advice on my career development, and provided constructive comments to manuscripts. I greatly thank all the talented scientists who provided technical supports and training for my experiments, in particular Drs. Stephan Borensztajn, Eran Greenberg, Vitali Prakapenka, Yuming Xiao, Dongzhou Zhang, and Drs. Allen Hunter, Xudong Fan, Owen Neill. I want to thank my labmates and all the other colleagues, too many to be listed, who gave me endless help and support during the past five years.

This dissertation was supported by new faculty startup funding from Michigan State University, the Sloan Foundation's Deep Carbon Observatory Grant G-2017-9954, and National

Science Foundation (NSF) grants EAR-1664332 and 1751664 to Prof. Dorfman. Parts of this dissertation were supported by IPGP multidisciplinary program PARI, and by Region Île-de-France SESAME Grant no. 12015908 to Dr. James Badro. Parts of this dissertation were supported by NSF grants EAR-1763189 and AST-1344133 to Prof. Jie Li. Parts of the beamtime for this dissertation were provided through the Chicago-DOE Alliance Center. Parts of the work were performed at GeoSoilEnviroCARS (The University of Chicago, Sector 13), Advanced Photon Source (APS), Argonne National Laboratory. GeoSoilEnviroCARS is supported by the National Science Foundation-Earth Sciences (EAR-1634415) and Department of Energy-GeoSciences (DE-FG02-94ER14466). Use of the COMPRES-GSECARS gas loading system and the PX2 program was supported by COMPRES under NSF Cooperative Agreement EAR-1661511 and by GSECARS through NSF grant EAR-1634415 and DOE grant DEFG02-94ER14466. Parts of this dissertation were performed at HPCAT (Sector 16), Advanced Photon Source (APS), Argonne National Laboratory. HPCAT operations are supported by DOE-NNSA's Office of Experimental Sciences. This work used resources of the Advanced Photon Source, a U.S. Department of Energy (DOE) Office of Science User Facility operated for the DOE Office of Science by Argonne National Laboratory under Contract No. DE-AC02-06CH11357.

Finally and most importantly, I would like to express sincere gratitude to my parents, my parents-in-law, and my wife for their love, support, and encouragement throughout my life.

TABLE OF CONTENTS

| LIST OF TABLES | x |
|--|----------|
| LIST OF FIGURES | xi |
| Chapter 1 Introduction | 1 |
| Chapter 2 Thermal equation of state of post-aragonite CaCO ₃ -Pmmn | 11 |
| 2.1 Abstract | |
| 2.2 Introduction | 12 |
| 2.3 Experimental methods | 15 |
| 2.4 Results and discussion | |
| 2.4.1 Synthesis and stability of CaCO ₃ -Pmmn | 16 |
| 2.4.2 Compressibility of CaCO ₃ -Pmmn at 300 K | |
| 2.4.3 Thermal equation of state of CaCO ₃ -Pmmn | 20 |
| 2.5 Implications | 23 |
| Chapter 3 Reversal of carbonate-silicate cation exchange in cold slabs in Earth's lower mantle 3.1 Abstract | 43 |
| 3.2 Introduction | |
| 3.3 Results | |
| 3.3.1 Calcium carbonate reaction to form magnesium carbonate | |
| 3.3.2 Magnesium carbonate reaction to form calcium carbonate | |
| 3.4 Discussion | |
| 3.5 Methods | |
| 3.5.1 Starting materials | |
| 3.5.2 LHDAC experiments | |
| 3.5.3 In-situ XRD | |
| 3.5.4 Ex-situ EDX | |
| 3.6 Supporting Information | 56 |
| Chapter 4 Spin transitions and compressibility of ϵ -Fe ₇ N ₃ and γ '-Fe ₄ N: implications for iron | |
| alloys in terrestrial planet cores | |
| 4.1 Abstract | |
| 4.2 Introduction | |
| 4.3 Experimental methods | |
| 4.4 Results | |
| 4.4.1 No structural transition of Fe ₇ N ₃ or Fe ₄ N | |
| 4.4.2 Spin states of ε -Fe ₇ N ₃ and γ '-Fe ₄ N | 89 ሰሰ |
| 4.4.3 Compression behavior of ε-Fe ₇ N ₃ and γ'-Fe ₄ N | |
| | |
| 4.5.1 Magnetic transitions of ε -Fe ₇ N ₃ and γ '-Fe ₄ N | УЭ |

| 4.5.2 Magneto-elastic coupling in Fe-light element alloys/compounds | 98 |
|---|-----|
| 4.5.3 Implications for iron alloys in Earth's and planetary cores | 101 |
| 4.6 Conclusions | 102 |
| | |
| | |
| BIBLIOGRAPHY | 122 |

LIST OF TABLES

| Table 2-1: Comparison of parameters of BM3 EoS of CaCO ₃ -Pmmn at 300 K |
|--|
| Table 2-2: Thermoelastic parameters of CaCO ₃ , MgCO ₃ , and major components in eclogite 38 |
| Table 2-3: Unit cell parameters of CaCO ₃ -Pmmn at different P-T conditions |
| Table 3-1: Starting materials, experimental conditions, and run products for all experiments. Starting materials for experiments were loaded in sandwich configuration, with laser absorber layer between two thermal insulation layers. Pressures determined from Raman shift of the singlet peak of the diamond anvil at the culet surface (Akahama & Kawamura, 2006) with 2σ uncertainties. The temperature reported is the temporal average of recorded temperatures over the heating duration rounded to the nearest 50 K. Temperature fluctuations over this time scale were less than the specified uncertainty, which is derived from a standard deviation of temperature measurements from both sides of the laser-heated sample (typically ± 100 K below 2000 K and ± 150 K above 2000 K) |
| Table 3-2: Parameters for isotopic mass balance calculations (see Supplementary Note 1 for details) |
| Table 4-1: Equation of state parameters of ϵ -Fe ₇ N ₃ and γ '-Fe ₄ N |
| Table 4-2: Volume and unit-cell parameters of ϵ -Fe ₇ N ₃ at 300 K. The uncertainties of pressures were propagated from uncertainties of unit cell volumes of Au and Ne, and uncertainties of their equation of state parameters (Fei et al., 2007), respectively. 117 |
| Table 4-3: Volume and unit-cell parameters of γ '-Fe ₄ N at 300 K. The uncertainties of pressures were propagated from uncertainties of unit cell volumes of Au and Ne, and uncertainties of their equation of state parameters (Fei et al., 2007), respectively. 118 |
| Table 4-4: Volume and unit-cell parameters of Fe at 300 K. The uncertainties of pressures were propagated from uncertainties of unit cell volumes of Au and Ne, and uncertainties of their equation of state parameters (Fei et al., 2007), respectively |
| Table 4-5: Mie-Grüneisen-Debye equation of state parameters of nonmagnetic iron alloys and pure iron |

LIST OF FIGURES

| Figure 1-1: 0 | Origins and behavior of volatile elements in Earth's interior |
|------------------|--|
| Figure 1-2: l | Plate tectonics and volatile elements cycling between Earth's surface and interior 10 |
| | Full-profile Le Bail refinement confirms the synthesis of CaCO ₃ -Pmmn. Measured XRD data for the quenched sample after heating at 49 GPa and 300 K (black dots) are consistent with orthorhombic post-aragonite structure (space group Pmmn with Z = 2) (black ticks below). Le Bail fit (red curve) also includes expected peak positions for Au calibrant (yellow sticks) and Ne medium (blue ticks). One unknown peak at 2θ around ~7° (marked by an asterisk) may be from the metastable CaCO ₃ -P2 ₁ /c-l due to kinetics. The wavelength of the monochromatic X-ray beam is 0.3344 Å |
| i 1 () | Representative in-situ X-ray diffraction patterns of CaCO ₃ -Pmmn. (a) Representative in-situ X-ray diffraction patterns of CaCO ₃ -Pmmn measured at high pressures and room temperature (black marker). (b) Representative high-temperature X-ray diffraction patterns of CaCO ₃ -Pmmn at ~60 GPa (black marker) measured in-situ in a laser-heated diamond anvil cell. In all XRD patterns, Au was used as the internal pressure calibrant (Fei et al., 2007) and laser-absorber (orange marker), while Ne was used as the thermal insulator and pressure medium (blue marker). The wavelength of the monochromatic X-ray beam is 0.3344 Å |
| | Equation of state of CaCO ₃ -pmmn. (a) Pressure-volume data for CaCO ₃ -Pmmn at room temperature from this study (black circle) and previous studies. Data from Ono et al. (2005) (red square) and Lobanov et al. (2017) (blue square) were recalculated using Pt pressure scale (Fei et al., 2007). Black solid curve (this study) is modeled by BM3 EoS using $K_{T0} = 162(\pm 62)$ GPa, $K0' = 3.1$ (± 1.1), and $V_0 = 96.6(\pm 4.8)$ Å ³ . A brown dashed curve (Oganov et al., 2006) and a purple dashed curve (Marcondes et al., 2016) modeled by BM3 EoS constrained via DFT-GGA and LDA, respectively. (b) Isothermal bulk modulus (K_T) at 300 K calculated by BM3 EoS. The black solid line, dashed line and short-dashed line represent the BM3 EoS fittings without constraint, with a fixed $V_0 = 97.76$ Å ³ and with reference pressure set at 50 GPa |
| | Volume Eulerian strain (f) - normalized pressure (F) plot of CaCO ₃ - $Pmmn$. The dashed line represents the linear fit through the data, and a red envelope indicates 95% confidence interval. The V_0 was set as 96.6 Å ³ obtained by BM3 EoS fitting of experimental data at 300 K. |
| j] | Measured pressure-volume-temperature data for CaCO ₃ - <i>Pmmn</i> . Colorful curves are isotherms at 1300, 1600, 1900, 2200 K modeled by (a) HT-BM3 EoS and (b) MGD EoS, respectively, with parameters listed in Table 2-2. Black points and curve are at 300 K same as Figure 2-3. The lower panel of each figure shows fitting residuals33 |

- Figure 2-7: Modeled (a) bulk sound velocity and (b) density profiles of eclogite and carbonated-eclogite with the presence of CaCO₃-MgCO₃ mixture as 2, 5 and 10 mol.%, respectively. The eclogite is assumed to be composed by 27 mol.% bridgmanite [(Mg_{0.9},Fe_{0.1})SiO₃], 24 mol.% Ca-perovskite (CaSiO₃), 20 mol.% stishovite (SiO₂), 29 mol.% Al-bearing calcium-ferrite-type silicate [(Mg_{0.9},Fe_{0.1})Al₂O₄], and the thermoelastic parameters of these phases are listed in Table 2-2. The pressure is ranging from 30 to 80 GPa along cold geotherm (Syracuse et al., 2010). The CaCO₃-Pnma to CaCO₃-Pmmn transition is assumed to occur at 45 GPa. The PREM model (Dziewonski & Anderson, 1981) is plotted as a comparison of the averaged mantle.
- Figure 3-1: Electron microscopic characterizations of recovered samples. Images of selected recovered sample cross-sections obtained using backscattered scanning electron microscopy (a, d, g), scanning transmitted electron microscopy (b, e, h) and energydispersive X-ray mapping (c, f, i) of the cross-section show the silicate layer sandwiched by two carbonate layers, with the reaction region along the contacting interface. (a-c) Ex-situ analysis of sample quenched from 33 GPa and 1650 K heated for 15 min (run #1) demonstrates reaction CaC-to-MgC: CaSiO₃ is not present in starting materials but is indicated in EDX map by colocation of Ca and Si, shown in magenta; (d-f) Ex-situ analysis of sample quenched from 88 GPa and 1800 K heated for 150 min (run #9) demonstrates reaction MgC-to-CaC: MgSiO₃ is not present in starting materials but is indicated in EDX map by colocation of Mg and Si, shown in blue-green. CaCO₃ also appears as red (Ca, but no Si) ribbon within CaSiO₃ starting material. (g-i) Ex-situ analysis of sample quenched from 133 GPa and 2000 K heated for 400 min (run #10) demonstrates reaction MgC-to-CaC: MgSiO₃ appears as Cadepleted, Si-rich region (blue or blue-green) adjacent to CaSiO₃ starting material
- Figure 3-2: Phase diagram for relative stability of the MgCO₃ + CaSiO₃ assemblage versus CaCO₃ + MgSiO₃. The boundary sketched as a black dashed line with gray shadow as uncertainty inferred is based on experimental observations of carbonate-silicate exchange reactions CaC-to-MgC and MgC-to-CaC. Squares represent observations from this work starting with (Ca,Mg)CO₃ and (Mg,Fe)SiO₃, looking for newly-synthesized CaSiO₃ to indicate the CaC-to-MgC reaction takes place. Circle symbols

- Figure 3-3: Pressure-temperature diagram of reactions between carbonate, silicates, and silica in the subducted oceanic crust to the lower mantle. The grey dotted line indicates the reversal boundary of the carbonate-silicate exchange reaction proposed by this study, whereas previous theoretical predictions are illustrated by yellow shaded region (Santos et al., 2019; Yao et al., 2018b; Zhang et al., 2018). The cyan and orange lines indicate the decarbonation reactions of CaCO₃ + SiO₂ (Li et al., 2018) and MgCO₃ + SiO₂ (Drewitt et al., 2019), respectively. The black dashed line shows the melting curve of MgCO₃-CaCO₃ system constrained by Thomson et al. (Thomson et al., 2014). Four typical mantle geotherms are modified from Maeda et al. (Maeda et al., 2017). The red shaded region indicates the transition boundary of CaCO₃ from *sp*²- to *sp*³ structure predicted by density functional theory computations (Santos et al., 2020; Zhang et al., 2018).

- Figure 3-6: Microscope images of loaded sample for run #9. We loaded the Fe-bearing sample on top of the thermal insulation layer on the piston side of DAC (75/300 beveled anvil), then we loaded another insulation layer on the cylinder side of DAC together with Re gasket before we close and compress the DAC to the target pressure. (a) Samples are loaded at ambient conditions on the piston side before closing the cell. (b) Samples are compressed to target pressure before heating, and the dashed circle indicates the dark Fe-bearing sample. (c) The heating spot on the loaded sample during laser heating.67

| Figure 3-7: | X-ray diffraction patterns obtained from the starting material of CaC-to-MgC before heating (a) and products quenched from various <i>P-T</i> conditions: (b) run #1, (c) run #4, (d) run #5, and (e) run #7, and phase identifications are indicated by small ticks at the bottom. The wavelength of the incident X-ray beam was 0.3344 Å |
|-------------|---|
| Figure 3-8: | Representative unrolled X-ray diffraction images (lower panel) corresponding to X-ray diffraction patterns (upper panel) obtained from the starting materials of CaC-to-MgC before heating and the products quenched from various <i>P-T</i> conditions: (a-b) run #4, (c-d) run #5. Large spots in 2D diffraction patterns in (a) and (b) are from untransformed dolomite starting material. The wavelength of the incident X-ray beam was 0.3344 Å. |
| Figure 3-9: | Representative full-profile fitting for XRD of (a) run #1 and (b) run #5. Le Bail refinements (red curves) of observed XRD data (black dots) were carried out after background subtraction, demonstrating all the identified phases (vertical ticks below patterns) can account for the peaks and intensities of XRD patterns. Black curves are fitting residues. The wavelength of the incident X-ray beam was 0.3344 Å |
| Figure 3-10 | Ex-situ analysis of sample quenched from 33 GPa and 1650 K heated for 15 min (run #1) demonstrates CaC-to-MgC. (a) SEM-BSE image obtained during FIB milling. Sample was prepared as a (Mg,Fe)SiO ₃ layer sandwiched by two (Ca,Mg)CO ₃ layers; (b) dark-field STEM image reveals CaSiO ₃ and MgCO ₃ , as well as SiO ₂ and FeO, formed by reaction between (Mg,Fe)SiO ₃ and (Ca,Mg)CO ₃ layers; (c) EDX spectrum and corresponding (d) chemical maps for calcium, silicon, magnesium, carbon, and iron. |
| Figure 3-11 | : Ex-situ analysis of sample quenched from 88 GPa and 1800 K heated for 150 min (run #9) demonstrates MgC-to-CaC. (a) SEM-BSE image obtained during FIB milling. Sample was prepared as an (Mg,Fe)CO ₃ layer sandwiched by two CaSiO ₃ layers; (b) dark-field STEM image reveals (Mg,Fe)SiO ₃ and CaCO ₃ formed by reaction of (Mg,Fe)CO ₃ and CaSiO ₃ layers; (c) STEM-EDX spectrum and corresponding (d) chemical maps for magnesium, silicon, calcium, and carbon |
| Figure 3-12 | 2: Ex-situ analysis of sample quenched from 133 GPa and 2000 K heated for 400 min (run #10) demonstrates MgC-to-CaC. (a) SEM-BSE image obtained during FIB milling. Sample was prepared as a (Mg,Fe)CO ₃ layer sandwiched by two CaSiO ₃ layers; (b) dark-field STEM image reveals (Mg,Fe)SiO ₃ and CaCO ₃ formed by reaction of (Mg,Fe)CO ₃ and CaSiO ₃ layers; (c) EDX spectrum and corresponding (d) chemical maps for magnesium, silicon, calcium, and carbon |
| Figure 3-13 | Ex-situ analysis of sample quenched from 35 GPa and 1900 K heated for 20 min (run #8) demonstrates MgC-to-CaC. (a) SEM-BSE image obtained during FIB milling. Sample was prepared as a (Mg,Fe)CO ₃ layer sandwiched by two CaSiO ₃ layers; (b) STEM-EDX chemical maps for calcium, silicon, magnesium, carbon, iron and oxygen |
| | |

| | : Typical temperature measurements of downstream (red squares) and upstream (blue circles) over heating duration of (a) run #5 for CaC-to-MgC and (b) run #9 for MgC-to-CaC, respectively |
|---|---|
| | 5: Representative temperature measurements and fitting profiles of upstream and downstream for run #9. Temperatures of the heated samples were determined by fitting the measured thermal radiation spectra using the Planck radiation function under the graybody approximation |
| - | Calculated isotopic composition versus reaction rate after the reaction (a) CaC-to-MgC and (b) MgC-to-CaC. n represents the mole fraction of Mg in $(Mg_nCa_{n-1})CO_3$. Black dashed line represents the average $\delta^{44/40}Ca$ and $\delta^{26}Mg$ values in carbonates, respectively. |
| - | Calculated isotopic composition of carbonated pyrolite after isotopic fractionation between carbonates and silicates for the reaction (a) CaC-to-MgC and (b) MgC-to-CaC. The horizontal axis represents the mole ratio of Mg/Ca in the carbonated pyrolite. <i>k</i> represents reaction rate. |
| C | (a) and (b) are representative X-ray diffraction patterns of ε -Fe ₇ N ₃ at 1 and 60 GPa at 300 K, respectively; (c) and (d) are representative X-ray diffraction patterns of γ '-Fe ₄ N at 1 and 60 GPa at 300 K, respectively. Le Bail refinements (red solid curves) of observed XRD data (black dots) were carried out after background subtraction, demonstrating all sample peaks match hexagonal ε -Fe ₇ N ₃ and cubic γ '-Fe ₄ N, respectively, within the investigated pressure range. The vertical ticks are ε -Fe ₇ N ₃ (blue), γ '-Fe ₄ N (dark green), and the pressure calibrant, Au (orange). The wavelength of the incident X-ray beam was 0.434 Å. |
| | (a-b) Fe- K_{β} fluorescence spectra of ε-Fe ₇ N ₃ and γ'-Fe ₄ N up to 60.5 GPa at 300 K. The XES spectra were normalized to unity in integrated intensity. The top-left inset shows intensity difference of observed satellite emission peak (K_{β} ') between 7030 and 7053 eV relative to the low-spin reference FeS ₂ at 0 GPa (black dashed line). (c-d) Highspin fraction of Fe in ε-Fe ₇ N ₃ and γ'-Fe ₄ N as a function of pressure derived from the XES measurements following integrated relative difference method (Mao et al., 2014). Completion of the spin transition of ε-Fe ₇ N ₃ is at ~40 GPa, and for γ'-Fe ₄ N at ~30 GPa. The dashed line is fitted by Boltzmann function, and error bars determined by comparing results using FeS ₂ vs. sample at 60 GPa as low-spin references. Pressures were determined by ruby fluorescence (Mao et al., 1986) before and after each XES collection, which differed by up to 10% due to relaxation of the sample or cell assembly. |
| | Compression behavior of ε-Fe ₇ N ₃ at 300 K. (a) Unit-cell volume of ε-Fe ₇ N ₃ up to 60 GPa at 300 K determined from X-ray diffraction measurements in this work (solid circles), together with previous experimental results. The black and red curves |

represent the 3rd-order Birch-Murnaghan equation of state (BM3-EoS) fits for the data for high spin (HS) and mixed spin (MS) / magnetic state (1 bar-40 GPa), low spin (LS) / nonmagnetic state (40-60 GPa), respectively. (b) Normalized stress *G* as a function

| | of effective strain g . Solid black, gray, and red circles represent the results of high spin, mixed spin, and low spin state, respectively, as determined by XES. Black and red lines indicate fits of the high spin and low spin state $G(g)$ data, respectively. The V_0 for the nonmagnetic state is obtained by extrapolating g to g_0 |
|-------------|---|
| Figure 4-4: | Compression behavior of γ '-Fe ₄ N at 300 K. (a) Unit-cell volume of γ '-Fe ₄ N up to 60 GPa at 300 K determined from X-ray diffraction measurements in this work (dark green circles), together with previous experimental results. The black curve represents the 3rd-order Birch-Murnaghan equation of state (BM-EoS) fit of all pressure-volume data from this study. (b) Normalized stress G as a function of effective strain g . Solid black, gray, and red circles represent the results of high spin, mixed spin, and low spin state, respectively, as determined by XES. The black solid line indicates a linear fit for all data. The pressure of onset and completion of spin transition is indicated by XES, but no change in compressibility can be observed in either plot |
| Figure 4-5: | Isothermal bulk modulus (K) of high spin and mixed spin (magnetic) state $\epsilon\text{-Fe}_7N_3$ (black curve), low spin (nonmagnetic) state $\epsilon\text{-Fe}_7N_3$ (red curve), and γ '-Fe ₄ N (dark green curve) at 300 K as a function of pressure, calculated from the fitted BM-EOS parameters (Table 4-1). The magnetic to nonmagnetic transition of $\epsilon\text{-Fe}_7N_3$ induces +22% increase in incompressibility at 40 GPa |
| Figure 4-6: | Normalized stress G as a function of effective strain g for (a) Fe ₃ S (Chen et al., 2007; Kamada et al., 2014; Seagle et al., 2006), (b) Fe ₃ P (Lai et al., 2020), (c) Fe ₇ C ₃ (Chen et al., 2012; Liu et al., 2016), and (d) Fe ₃ C (Li et al., 2002; Litasov et al., 2013; Ono & Mibe, 2010; Sata et al., 2010). Dashed lines are linear fits to g - G , and the discontinuity in compression behavior corresponds to the change of slope of the linearized g - G plot. 110 |
| Figure 4-7: | Compression behavior of pure Fe at 300 K. (a) Unit-cell volume of α -Fe (black circles) and ϵ -Fe (red circles) up to 60 GPa at 300 K determined from X-ray diffraction measurements. The solid black curves and solid red curves represent the 3rd-order Birch-Murnaghan equation of state (BM-EoS) fits for the data for α -Fe (1-15 GPa) and ϵ -Fe (15-60 GPa), respectively. (b) Normalized stress G as a function of effective strain g . Solid black and red circles represent the results of α -Fe and ϵ -Fe, respectively. The black and red lines indicate linear fits for α -Fe and ϵ -Fe, respectively. The V_0 for the ϵ -Fe is obtained by extrapolating g to g_0 |
| Figure 4-8: | Full width at half maximum (FWHM) for Au (111) normalized to 2θ . Orange circles are data obtained from Au at position of γ '-Fe ₄ N sample in the diamond anvil cell. The peak broadening induced by the onset of nonhydrostaticity of Ne medium (Klotz et al., 2009) in this study starts at ~17 GPa. The magnitude of peak broadening remains small above this pressure, consistent with quasi-hydrostatic conditions in the sample chamber |
| Figure 4-9: | Crystal structure of ϵ -Fe ₇ N ₃ (left) and γ '-Fe ₄ N (right) at ambient conditions. Gray spheres in polyhedra represent the N atoms and brown spheres represent Fe atoms. |
| | |

| Figure 4-11: (a) Molar volumes of nonmagnetic ε-Fe ₇ N ₃ (light blue), β-Fe ₇ N ₃ (purple), 3γ'-Fe ₄ N |
|--|
| (green) and its isochemical assemblage of β -Fe ₇ N ₃ + 5 ϵ -Fe (light red) as a function of |
| pressure at 300 K. The calculation is based on BM3 EoS with parameters of relevant |
| phases summarized in Table 1 and 2. (b) Isothermal density profiles of nonmagnetic |
| β-Fe ₇ N ₃ (purple), Fe ₇ C ₃ (orange), Fe ₃ C (brown), Fe ₃ S (gray), Fe ₃ P (pink) along a 5500 |
| K isotherm. For comparison, a density profile of pure ε-Fe and seismologically |
| constrained density profile (Preliminary Reference Earth Model, Dziewonski & |
| Anderson, 1981) are also plotted. The calculation is based on Mie-Grüneisen-Debye |
| equation of state with parameters of relevant phases listed in Table 4-5 |
| |

Chapter 1 Introduction

Earth is unique among the planets in our solar system in that it has a habitable climate fostering life on the surface, not only owing to the stabilization of hydrosphere and atmosphere, but also the presence of life-essential volatile elements on Earth's surface, such as carbon, nitrogen, hydrogen, oxygen, and sulfur (Bergin et al., 2015; Hirschmann, 2016; Marty, 2012). Over Earth's history, the surface inventory of life-essential volatile elements has been maintained by cycling of materials between the surface and interior via outgassing and ingassing mechanisms induced by plate tectonics, which helps to stabilize the long-term moderation of the climate (Dasgupta, 2013; Shahar et al., 2019). The storage and fluxes of life-essential volatile elements in and between Earth's surface and interior constitute deep Earth volatile cycles, which are of importance in several fields of Earth sciences, such as mantle and core dynamics, chemical differentiation and thermal evolution history, subduction and volcanism, weathering and sedimentation, climate change, and origin and evolution of life (Hazen & Schiffries, 2013).

In addition, it has been one of the most exciting puzzles in planetary science to search for a habitable exoplanet. A habitable planet must have the ingredients necessary for the development of life, including the life-essential volatile elements on the surface. Assuming Earth-like concentration and distribution of volatile elements can sustain the habitability on an exoplanet, many efforts have been dedicated to constraining the origins, concentrations, and transportation of volatile elements in relevant reservoirs on Earth and planetary building blocks (Bergin et al., 2015; Hirschmann, 2016; Marty, 2012). The abundance of volatile elements of cosmochemical reservoirs can be directly constrained from chemical analysis of meteorites and samples returned by dedicated space missions. In contrast, it is difficult to estimate the Earth's bulk content of volatile

elements from accessible rocks on Earth's surface, such as basalts, because of the unknown amounts of elements buried in inaccessible deep mantle and core reservoirs. Mantle-derived basalts along mid-ocean ridge and oceanic intraplate volcanoes contain volatile elements from the interior, but a considerable amount of volatile elements have been lost during magma degassing due to their low solubility in silicate melts. Moreover, basalt generation only directly samples typically the top 100-200 km of the mantle, which results in large uncertainties when extrapolating the estimation to the bulk silicate Earth (Dasgupta & Hirschmann, 2010; Kelemen & Manning, 2015; Plank & Manning, 2019). Therefore, indirect geochemical and geophysical observations, theoretical prediction, and dynamic modeling are necessary for understanding the storage of volatiles in the current and primitive Earth's reservoirs, as well as their delivery, retention, and loss during primary planetary differentiation.

Earth formation and origins of volatile elements. Earth is believed to be the product of a number of collisions between the proto-Earth and other planetary bodies (Carlson et al., 2014; Wood et al., 2006). One of the final events during the accretion of Earth is believed to have been a large-scale collision with a Mars-sized impactor, which also resulted in the formation of Earth's moon around 4.5 billion years ago. This giant impact is thought to have generated enough energy to melt part or even all of the early Earth, creating planetary-scale volumes of molten rock that may form a magma ocean hundreds of kilometers in depth. The subsequent cooling of the planet from this molten state would have resulted in the segregation of iron-rich alloy from the magma ocean, and crystallization of the magma ocean into the solid mantle, which was a defining stage in the assembly of Earth's interior structure, the chemistry of its surface, and the formation of its early atmosphere (Carlson et al., 2014; Wood et al., 2006).

The present-day inventory of volatile elements in Earth's mantle and surface reservoirs are in part a product of the early events in Earth's history, such as accretion of volatile-rich materials, loss of volatile to space during accretion, and segregation of the metallic core and the silicate mantle (Bergin et al., 2015; Hirschmann, 2016; Liu et al., 2019; Marty, 2012). However, the processes of volatile acquisition into the early Earth remain poorly understood. One widely accepted model suggests that the Earth formed from chondritic material, but most of the volatiles were lost to space due to the high energy and temperature of accretion, and the Earth's volatiles were delivered by volatile-rich chondritic material in the form of late veneer after complete coremantle segregation (e.g., Albarede, 2009; Wang & Becker, 2013). Nevertheless, this model has been challenged by recent studies on partitioning behavior of carbon and sulfur, inferring their abundances do not formally require an accretion in a late veneer, and can be explained by a coremantle equilibration alone (e.g., Boujibar et al., 2014; Fischer et al., 2020).

The distribution of volatile elements between the core-forming metallic melt, silicate melt, and atmosphere is controlled by partitioning between metal and silicate, and solubility in silicate melt in equilibrium with the overlying atmosphere (Hirschmann, 2016). During core formation, some of the volatile elements entered the core, and some of them were trapped in the silicate mantle (Figure 1-1). Some major uncertainties in how much, for example, carbon is in the mantle or nitrogen is in the core, relate to limited information on phase equilibria and physical properties of the minerals that host these volatiles at depth (see Chapter 2 and Chapter 4).

Plate tectonics and volatile element cycling. The volatile elements in the mantle can be sampled by mantle-derived basalts, volcanic gases, and deep diamonds. Chemical analysis of species, concentration, and isotopic signatures of H, C, N, and S indicates they have been exchanged between the mantle and the Earth's surface. The volatiles can be trapped as solids in

minerals and conveyed into the mantle at subduction zones, where the hydrated and carbonated oceanic plates are plunging into the mantle. Some of the volatile elements are expelled during dehydration of plates and released back to the surface through arc magmatism, but a significant fraction of volatile elements survive dehydration and possibly continue all the way down to the core-mantle boundary (Dasgupta & Hirschmann, 2010; Kelemen & Manning, 2015; Plank & Manning, 2019) (Figure 1-2). The volatiles can return to the surface through volcanism and degassing at mid-ocean ridges and arcs, where volatile elements originally trapped in mantle minerals enter preferentially the magmas and degas to the atmosphere and hydrosphere during volcanic eruptions (Dasgupta & Hirschmann, 2010; Kelemen & Manning, 2015; Plank & Manning, 2019) (Figure 1-2).

In addition, diamonds provide unique information of Earth's interior since they can access Earth's deepest intact material through the minerals contained within their volumes. Although most diamonds are thought to crystalize in the mantle roots of the continental lithosphere, the so-called superdeep diamonds and their inclusions are believed to crystalize in the convecting upper mantle, transition zone, and even lower mantle (Stachel & Luth, 2015). The formation of superdeep diamonds itself is a key part of carbon cycling, since the redox reactions between carbonates in subducting slabs and metallic iron in the ambient mantle have been proposed as an important mechanism to produce superdeep diamonds (e.g., Dorfman et al., 2018; Rohrbach & Schmidt, 2011; Thomson et al., 2016b) (Figure 1-2). These diamonds may then carry to the surface traces of carbonates from great depth and reveal reactions that have taken place (see Chapters 2 and 3).

Carbon in the mantle. Carbon is the fourth most abundant element in the universe, which is the backbone for the chemistry of life and, in the form of CO₂, combines with water to provide

the greenhouse needed for a habitable Earth. Although the surface carbon inventory has a key influence in building and sustaining a habitable planet, the specific physical, chemical and dynamic processes in the Earth's interior that maintain the surface carbon inventory remain largely uncertain. One of the most debatable issues related to the carbon cycle is whether the global carbon flux into the Earth's interior through subduction is identical to the output through volcanism (Dasgupta & Hirschmann, 2010; Kelemen & Manning, 2015; Plank & Manning, 2019). Global carbon flux is difficult to constrain, since the mechanics of subduction (input) and carbonated melt production or CO₂ degassing (output) are dependent on multiple parameters. The fate and flux of carbon vary from trench to trench, as different subducting slab has a different mixture of carbon source (e.g., carbonate, organic carbon, sediment, serpentinite), temperature field, and geometry. The estimated carbon flux into the convecting mantle shows discrepancies and uncertainties in the order of magnitudes by various studies (Dasgupta & Hirschmann, 2010; Kelemen & Manning, 2015; Plank & Manning, 2019). Nonetheless, carbonates are the major source that conveys carbon into the deep Earth by subduction, and deep subduction of oceanic crust introduces a considerable amount of carbon into the mantle. Therefore, several important questions have arisen in order to better constrain the carbon flux: what is the fate of carbonate when subducted to Earth's deep interior? (Chapters 2 and 3) What are the physical and chemical properties of carbonates subducting to the lower mantle? (Chapter 2) Can carbonate remain stable until to the core-mantle boundary? (Chapter 3)

Nitrogen in the core. The abundance of volatile elements in Earth's core is impossible to measure directly. Seismic observations reveal the Earth's outer and inner core are ~10% and 6%, respectively, less dense than pure, solid iron under the same pressure and temperature conditions. This density deficit is primarily due to the presence of one or more light elements in the core, such

as Si, O, S, C, and H, although the identity of the light element(s) and abundance in the core is highly controversial (Hirose et al., 2013; Li & Fei, 2014). In addition, nitrogen has been proposed as one of the light element candidates in the core. Nitrogen is the seventh most abundant element in the solar system, and is a key component of DNA, RNA, and proteins, while also present as the dominant constituent of our atmosphere, but its evolution and abundance in the Earth's interior remain enigmatic. The abundance of nitrogen in the core can be constrained from geochemical and geophysical observations. The distribution of nitrogen in Earth's silicate mantle or metallic core depends on whether it is siderophile (iron-loving) or lithophile (rock-loving) during the coremantle segregation process, so the partitioning coefficient of nitrogen between metal and silicate at relevant core formation conditions can be a key parameter to constrain the nitrogen in the core. On the other hand, constraining the core's composition is by measuring physical properties of Ferich alloys at the pressure-temperature conditions of the Earth's core (densities, sound velocities, phase relations, etc.) and comparing them to seismological measurements of core properties (Hirose et al., 2013; Li & Fei, 2014). Therefore, several important questions have arisen to better constrain the nitrogen in the core: what are the physical and chemical properties of iron-nitrogen alloys (iron nitride) at core conditions? How does nitrogen affect the physical properties of iron in the core? (Chapter 4).

Dissertation outline. In this dissertation, I have investigated the physical and chemical behavior of carbonates and iron nitrides to decipher the role of carbon and nitrogen within the Earth and planetary deep interior.

In chapter two, I report the results of in-situ high pressure and temperature X-ray diffraction measurements to study the stability and physical properties of CaCO₃ at lower mantle conditions. It has been shown that CaCO₃ crystallizes in the form of calcite at the Earth's surface. As

subducting to the mantle, CaCO₃ undergoes a series of phase transitions at high pressures, and six high-pressure polymorphs of CaCO₃ corresponding to the mantle conditions have been reported, i.e., same composition with different crystal structures (e.g., Lobanov et al., 2017; Oganov et al., 2013; Pickard & Needs, 2015). I focused on studying one of the CaCO₃ polymorphs, post-aragonite, which is believed to be the dominant stable phase along mantle geotherm from 25 to 135 GPa and 2000 to 2500 K.

In chapter three, I examine the stability of carbonates, MgCO₃ and CaCO₃, coexisting with the lower mantle minerals. Previous studies show carbon has limited solubility in mantle silicates, and therefore resides chiefly in carbon-rich accessory phases in the deep mantle, such as carbonates, carbonate melts, carbon-bearing fluids, graphite, diamond, and/or iron carbides (Oganov et al., 2013). One question that scientists have dedicated efforts to answer is what are forms of carbon in Earth's deep interior, which is important to constrain carbon storage in the mantle reservoir. In addition to constraining the stability of the single carbonate phase as chapter two did, I designed a series of high pressure and temperature experiments to investigate the stability and phase equilibrium between carbonate and silicates.

In chapter four, I focus on the spin/magnetic transition and its effect on the incompressibility of iron nitrides, which provide new constraints on the role of nitrogen and other volatile elements in the core. Iron is the most abundant transition metal within the Earth and the major component of the core. Iron has its 3d electronic shells partially filled, leading to a series of possible energy configurations that depend on its atomic environment: iron adopts different valences, namely metallic (Fe⁰), ferrous (Fe²⁺), and ferric (Fe³⁺) iron, and different electronic configurations, such as high-spin and low-spin states. The spin transitions of iron in silicates, oxides, and alloys have been reported, which revealed the role of spin transitions on physical,

chemical, and transport properties of the deep Earth (Badro, 2014; Lin et al., 2013). Here I study the pressure-driven spin transition of iron nitrides, and compared the effects of nitrogen with other volatile elements.

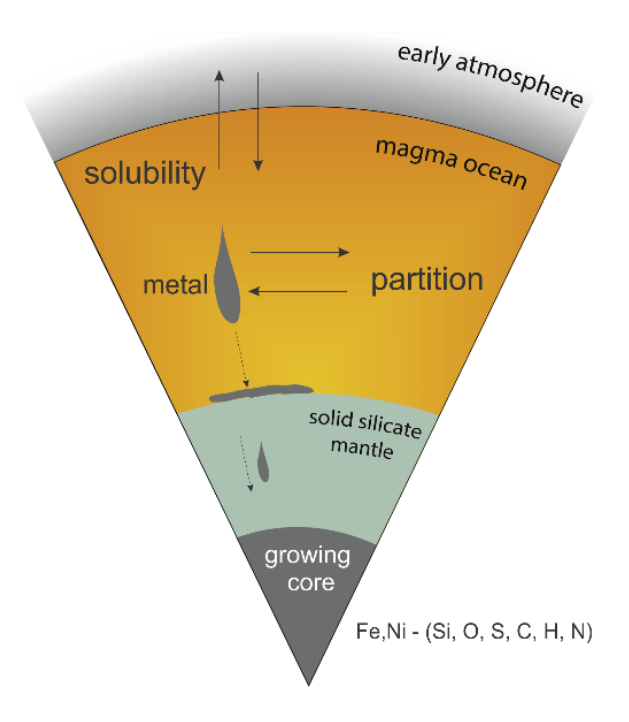


Figure 1-1: Origins and behavior of volatile elements in Earth's interior.

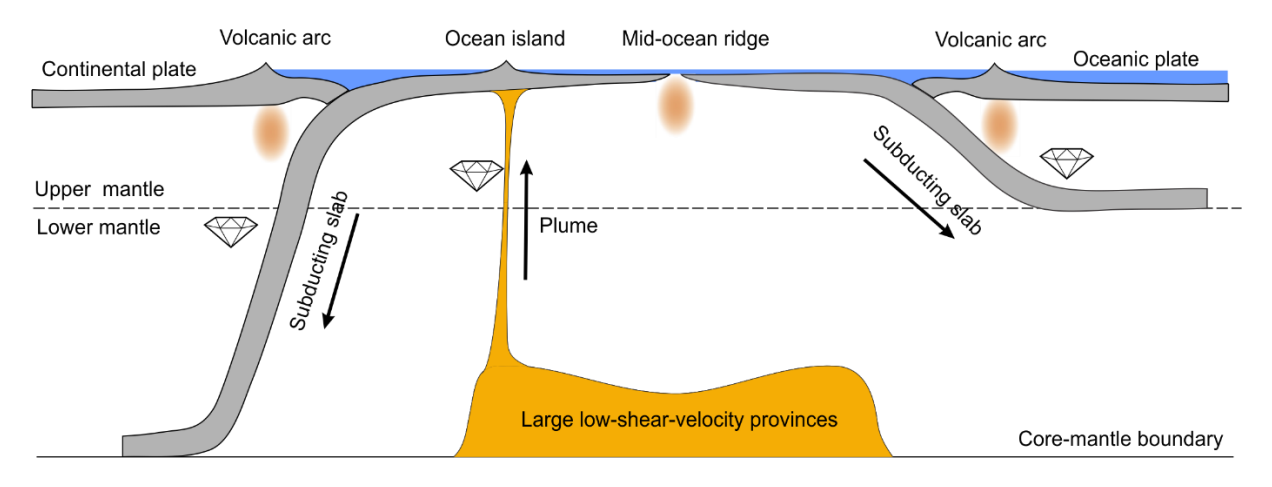


Figure 1-2: Plate tectonics and volatile elements cycling between Earth's surface and interior.

Chapter 2 Thermal equation of state of post-aragonite CaCO₃-Pmmn

This chapter has been published as Lv et al. (2020a).

2.1 Abstract

Calcium carbonate (CaCO₃) is one of the most abundant carbonates on Earth's surface and transports carbon to Earth's interior via subduction. Although some petrological observations support preservation of CaCO₃ in cold slabs to lower mantle depths, the geophysical properties and stability of CaCO₃ at these depths are not known, due in part to complicated polymorphic phase transitions and lack of constraints on thermodynamic properties. Here we measured thermal equation of state of CaCO₃-Pmmn, the stable polymorph of CaCO₃ through much of the lower mantle, using synchrotron X-ray diffraction in a laser-heated diamond-anvil cell up to 75 GPa and 2200 K. The room temperature compression data for CaCO₃-Pmmn are fit with third-order Birch-Murnaghan equation of state, yielding $K_{T0} = 146.7~(\pm 1.9)$ GPa and $K_0' = 3.4(\pm 0.1)$ with V_0 fixed to the value determined by ab initio calculation, 97.76 Å³. High-temperature compression data are consistent with zero-pressure thermal expansion $\alpha_T = a_0 + a_1 T$ with $a_0 = 4.3(\pm 0.3) \times 10^{-5}$ K⁻¹, $a_1 =$ $0.8(\pm0.2)\times10^{-8}$ K⁻², temperature derivative of the bulk modulus $(\partial K_T/\partial T)_P = -0.021(\pm0.001)$ GPa/K; the Grüneisen parameter $y_0 = 1.94(\pm 0.02)$, and the volume independent constant $q = 1.9(\pm 0.3)$ at a fixed Debye temperature $\theta_0 = 631$ K predicted via ab initio calculation. Using these newly determined thermodynamic parameters, the density and bulk sound velocity of CaCO₃-Pmmn and (Ca,Mg)-carbonate bearing eclogite are quantitatively modeled from 30 to 80 GPa along a cold slab geotherm. With the assumption that carbonates are homogeneously mixed into the slab, the results indicate the presence of carbonates in subducted slab is unlikely to be detected by seismic

observations, and the source of buoyancy provided by carbonates is negligible to affect slab dynamics.

2.2 Introduction

Calcium carbonate (CaCO₃) in the form of calcite is one of the most abundant carbonates on Earth's surface (reviewed by Luth, 1999), and an important vector of carbon to Earth's interior. Calcite can be sequestered in the oceanic crust by hydrothermal alteration and biological activity, and transferred to the mantle in subducting slabs (Dasgupta & Hirschmann, 2010; Kelemen & Manning, 2015; Staudigel, 2014). However, four major chemical processes have been argued to block transport of CaCO₃ transport to the lower mantle: 1) melting of carbonate and carbonated peridotite or eclogite (e.g., Dasgupta & Hirschmann, 2006; Ghosh et al., 2014; Kiseeva et al., 2013; Thomson et al., 2016b), 2) reduction of carbonate solid or melt through reaction with iron or other reduced phases, generating diamond (e.g., Dorfman et al., 2018; Palyanov et al., 2013; Rohrbach & Schmidt, 2011), 3) carbonate-silicate exchange consuming CaCO₃ to form Ca-perovskite and MgCO₃ (e.g., Biellmann et al., 1993; Seto et al., 2008), 4) decarbonation of CaCO₃ with free silica phase to form Ca-perovskite, CO₂ or C (e.g., Drewitt et al., 2019; Li et al., 2018). Whether the energetics and kinetics of these reactions lead to complete loss of CaCO3 from very cold and/or fast subducting slabs has been controversial (e.g., Martirosyan et al., 2016; Zhu et al., 2019), though superdeep diamonds with CaCO₃ inclusions coexisting with lower mantle phases such as CaSiO₃ perovskite (Brenker et al., 2007; Bulanova et al., 2010; Tschauner et al., 2018) prove the existence of CaCO₃ in at least some regions of the transition zone and lower mantle. To determine the conditions needed to preserve CaCO₃ in these regions and its fate during subduction to the

mantle, experimental constraints on thermodynamic behavior of CaCO₃ are needed at lower-mantle conditions.

At mantle pressure and temperature (P-T) conditions, multiple polymorphic phase transitions of CaCO₃ have recently been discovered and debated, with potentially important effects on melting and other chemical reactions in the mantle. Calcite is stable up to ~3 GPa and then transforms to aragonite with space group Pnma (CaCO₃-Pnma), which remains stable through the transition zone and shallow lower mantle (e.g., Litasov et al., 2017a). The reported melting curve of CaCO₃-Pnma and a mixture of CaCO₃-MgCO₃ are higher than a hot slab geotherm (Li et al., 2017; Thomson et al., 2014), suggesting that subducted CaCO₃ may survive melting in the transition zone and travel to the lower mantle. At lower mantle pressures, the post-aragonite structures have been a subject of active recent research, and experimental studies from ~40 to 50 GPa have identified 1 transition to an orthorhombic structure, or transitions to an intermediate monoclinic structure then an orthorhombic structure. The orthorhombic structure is most commonly termed "post-aragonite" (CaCO₃-Pmmn), which was first identified by (Ono et al., 2005) at ~40 GPa and confirmed by computational structure simulations (Oganov et al., 2006). More recently, a monoclinic $P2_1/c$ structure (CaCO₃- $P2_1/c$ -1, "-1" = low-pressure) was predicted to be an intermediate stable phase from ~40 to 50 GPa between CaCO₃-Pnma and CaCO₃-Pmmn (Gavryushkin et al., 2017; Pickard & Needs, 2015; Smith et al., 2018). CaCO₃-P2₁/c-1 was observed experimentally by (Gavryushkin et al., 2017; Li et al., 2018; Smith et al., 2018), but the transition from monoclinic to CaCO₃-Pmmn was found to be kinetically challenging (Smith et al., 2018). Near the base of Earth's mantle, $CaCO_3$ is expected to transform from one of these sp^2 hybridized post-aragonite structures to one of multiple proposed sp³-hybridized post-postaragonite structures. The first sp^3 -hybridized post-post-aragonite to be identified was a pyroxenestructured $C222_1$ phase (CaCO₃- $C222_1$) observed at pressures higher than 130 GPa, corresponding to conditions near the core-mantle boundary (Oganov et al., 2006; Oganov et al., 2008; Ono et al., 2007). A second monoclinic $P2_1$ /c structure with sp^3 -hybridization, termed CaCO₃- $P2_1$ /c-h ("-h" = high-pressure, to distinguish it from the lower-pressure "-1" polymorph), was predicted to be more favorable than CaCO₃- $C222_1$ (Pickard & Needs, 2015) and observed at pressures as low as ~105 GPa (Lobanov et al., 2017). Although the stable forms of CaCO₃ at the top and bottom of the lower mantle and conditions of the sp^2 - to sp^3 -hybridization transition in CaCO₃ remain controversial, CaCO₃-Pmmn is thought to be the stable phase of CaCO₃ throughout most of the lower mantle (see phase diagram of CaCO₃ proposed by Gavryushkin et al., 2017; Smith et al., 2018; Zhang et al., 2018).

The stability and abundance of CaCO₃-*Pmmn* can be modeled in the Earth using constraints on thermoelastic behavior, including accurate thermal equation of state (TEoS) measurements and corresponding thermoelastic parameters bulk modulus, its pressure and temperature derivatives, and thermal expansion coefficient. However, in contrast to the relatively well-known thermoelastic behavior of CaCO₃-*Pnma* (Li et al., 2015; Litasov et al., 2017a; Palaich et al., 2016; Ye et al., 2012), experimental and computational constraints on the equation of state (EoS) of CaCO₃-*Pmmn* have been limited to 300 K (Lobanov et al., 2017; Ono et al., 2005) and 0 K (Oganov et al., 2006), respectively, without addressing high-temperature expansion behavior. In order to accurately model the phase equilibrium and physical properties of CaCO₃ at lower mantle conditions, the TEoS study on CaCO₃-*Pmmn* is required.

In this study, we investigate the structural stability of CaCO₃-*Pmmn*, and establish its TEoS up to 75 GPa and 2200 K using synchrotron X-ray diffraction in a laser-heated diamond anvil cell (LHDAC). The physical properties of CaCO₃ along cold subducting slab geotherm are calculated

using the TEoS parameters, which are compared with the other major endmember carbonate, MgCO₃. By combining the newly obtained parameters with literature thermodynamic parameters of mineral phases in the subducted slab, we model the effect of the presence of CaCO₃-MgCO₃ mixture on the density and bulk sound velocity of the carbonate-rich subducting slab at lower mantle conditions.

2.3 Experimental methods

CaCO₃-Pmmn was synthesized from calcite under high pressure and temperature conditions using a LHDAC. Sample material was prepared by mixing calcite powder (99.95%, Alfa Aesar) with 5 wt% micron-scale Au powder (99.95%, Goodfellow), which serves as a laser absorber and pressure calibrant. The mixture was mechanically ground under ethanol for 1 hour, then dried in an oven at 120 °C overnight to remove moisture contamination. The powder was slightly compressed to form a ~10-μm-thick disc for loading into the DAC. We use a symmetric DAC equipped with a pair of 150-μm culet beveled anvils to generate high pressures. A rhenium gasket of 250 μm thick was pre-indented to ~25-μm, and a hole with 75-μm diameter was drilled in the center of the indentation, serving as the sample chamber. To separate the sample disc from the diamond anvils, we loaded a sample disc into the sample chamber supported by three small ~5 μm-thick calcite spacers. To achieve quasi-hydrostatic conditions in the sample chamber, Ne was loaded as pressure transmitting medium and thermal insulator using the COMPRES/GSECARS gas-loading system (Rivers et al., 2008).

The TEoS of CaCO₃-Pmmn was determined using synchrotron X-ray diffraction with insitu laser heating carried out at beamline 13-ID-D of the GeoSoilEnviroCARS sector of the Advanced Photon Source (APS), Argonne National Laboratory (ANL). The monochromatic X-

ray beam with a wavelength of 0.3344 Å was focused on an area of $\sim 2.5 \times 3 \, \mu \text{m}^2$ on the sample. Each two-dimensional X-ray diffraction image was recorded on a CdTe 1M Pilatus detector for 30 s, and subsequently integrated using Dioptas software (Prescher & Prakapenka, 2015). The sample-to-detector distance, tilt, and rotation of the detector relative to the incident X-ray beam were calibrated using the diffraction pattern of LaB₆ powder at ambient conditions. The sample was heated using a double-sided Nd:YLF laser heating system (Prakapenka et al., 2008). Two 1.064 µm laser beams were focused to 20-µm diameter on both sides of the sample, and co-axially aligned with the incoming X-ray beam by using the X-ray-induced luminescence on the sample. Temperatures during heating were determined by fitting the measured thermal radiation spectra using the Planck radiation function under the graybody approximation (Prakapenka et al., 2008). The uncertainty of temperatures is ± 100 K up to 2000 K and ± 150 K higher than 2000 K based on multiple temperature measurements from both sides of the laser-heated sample. Pressures were calculated using the TEoS of the Au standard (Fei et al., 2007), with uncertainties propagating from that of temperatures, unit-cell volumes of Au, and TEoS parameters of Au, and the unit-cell volumes of Au were derived from diffraction lines (1 1 1), (2 0 0), (2 2 0) and (3 1 1) (Figure 2-1 and Figure 2-2).

2.4 Results and discussion

2.4.1 Synthesis and stability of CaCO₃-Pmmn

The starting material calcite was directly compressed in a DAC to the target pressure of 49 GPa before laser heating to synthesize the stable lower-mantle form of CaCO₃. During heating at 1800 K and after quench to 300 K, CaCO₃-*Pmmn* was confirmed by full-profile refinement XRD using the Le Bail method (Le Bail et al., 1988) as implemented in the GSAS/EXPGUI program

(Toby, 2001) (Figure 2-1). In contrast, some previous studies which attempted synthesis from CaCO₃-Pnma or CaCO₃-P2₁/c-1 (Gavryushkin et al., 2017; Smith et al., 2018) failed to obtain complete transformation to CaCO₃-Pmmn, perhaps due to thermal gradients during laser heating and/or high kinetic barriers to transitions between these structures. Sharp diffraction peaks of Au after annealing and intense diffraction from Ne pressure medium support quasi-hydrostatic stress conditions in the sample chamber (Figure 2-1 and Figure 2-2). An additional diffraction peak is observed at d-spacing of 2.6 Å, which broadens with increasing pressure and disappears above 60 GPa, probably representing metastable CaCO₃-P2₁/c-l retained due to phase transition kinetics (Bayarjargal et al., 2018; Gavryushkin et al., 2017; Li et al., 2018; Smith et al., 2018). The unitcell parameters of CaCO₃-Pmmn at 300 K and 49 GPa are consistent with previous observations (Gavryushkin et al., 2017; Ono et al., 2005) within the uncertainty of pressure calibration (Figure 2-1). As pressure and temperature increased, in-situ XRD exhibits no splitting or broadening of CaCO₃-Pmmn peaks, indicating no melting, dissociation or phase transition occurred (Figure 2-1 and Figure 2-2). This study concurs with other previous studies (e.g., Gavryushkin et al., 2017; Oganov et al., 2006; Ono et al., 2005) that CaCO₃-Pmmn is the stable form of CaCO₃ up to 75 GPa and 2200 K.

After synthesis of CaCO₃-*Pmmn*, we further compressed the sample at ~2-3 GPa intervals from 50 to 75 GPa, the minimum range of stability of this phase (Gavryushkin et al., 2017; Smith et al., 2018; Zhang et al., 2018). At each target pressure, we collected XRD patterns of the sample at 300 K before and after heating, and collected high-temperature patterns while the temperature was increasing at ~50-100 K intervals from ~1000 to 2200 K (Figure 2-2). The lattice parameters of CaCO₃-*Pmmn* were obtained by least-squares fitting of diffraction lines (1 1 1), (0 2 0), (2 0 0) and (0 2 1) by using PDIndexer software (Seto et al., 2010), and are provided in the Table 2-3.

To directly compare volumes observed at 300 K for CaCO₃-*Pmmn* to previous studies (Lobanov et al., 2017; Ono et al., 2005), we recalculated previously-reported pressures using the Pt scale of Fei et al. (2007) for consistency with Au scale applied in this study (Figure 2-3a). With this correction, all *P-V* data are consistent within uncertainty over the pressure range examined in this work.

2.4.2 Compressibility of CaCO₃-Pmmn at 300 K

Because all previous compression data for CaCO₃-*Pmmn* were obtained at room temperature only, and the room temperature isotherm provides a useful constraint on the *P-V-T* EoS, we first address the 300 K *P-V* EoS of CaCO₃-*Pmmn*. *P-V* data of CaCO₃-*Pmmn* obtained at 300 K were fit to a third-order Birch-Murnaghan equation of state (BM3 EoS) (Birch, 1952) using the error-weighted least squares method to constrain zero-pressure parameters unit-cell volume (V_0), bulk modulus (K_{T0}) and its pressure derivative (K'_0) (Figure 2-3a and Table 2-1). We first fit the data using BM3 EoS without constraints on parameters, yielding $V_0 = 96.6(\pm 4.8)$ Å³, $K_{T0} = 162(\pm 62)$ GPa, $K'_0 = 3.1(\pm 1.1)$. The large uncertainties in fitted parameters reflect the long extrapolation from high-pressure data to 1 bar for this unquenchable phase, but compressibility at mantle-relevant pressures is well-constrained.

Previous experimental studies (<u>Ono et al., 2005, Lobanov et al., 2017</u>) reported EoS parameters that may differ due to different scales used to determine pressure, extrapolation to 1 bar, and the choice to fix $K'_0 = 4$, as well as differences in hydrostatic conditions due to choice of pressure media. Experimental volumes obtained by Lobanov et al. (2017) without a pressure medium above ~90 GPa are high relative to our extrapolated EoS even with pressures corrected to match the pressure scale in this study (Figure 2-3a), corresponding to a relatively high

incompressibility at mantle pressures. However, the incompressibility K_{70} reported by both previous studies is relatively low compared to our unconstrained fit. This parameter trades off with relatively high V_0 and K'_0 in these studies. Since CaCO₃-Pmmn is an unquenchable phase and reverts to calcite upon decompression (Ono et al., 2005), the unit-cell volume at ambient pressure cannot be measured directly, which leads to large uncertainties on the 1 bar parameters. We therefore also fit our 300 K data setting 50 GPa as the reference pressure and obtain $K_{50} = 302(\pm 15)$ GPa, $K'_{50} = 2.1(\pm 1.7)$ and $V_{50} = 77.526(\pm 0.046)$ Å³. A fit to the 300 K data from Ono et al. (2005) and Lobanov et al. (2017) setting 50 GPa as the reference pressure yields larger K_{50} (Figure 2-3b). This difference is consistent with less hydrostatic conditions in the sample chamber provided by NaCl medium in Ono et al. (2005) and no pressure medium in Lobanov et al. (2017) relative to the quasi-hydrostatic conditions provided by Ne medium and frequent annealing in this study.

Analysis of the finite Eulerian strain corresponding to compression behavior of CaCO₃-Pmmn supports the low K'_0 from the BM3 EoS. P-V data can be described by the normalized stress $(f_E = [(V_0/V)^{2/3}-1]/2)$ versus the finite Eulerian strain $(F_E = P/[3f_E(1+2f_E)^{5/2}])$ plot (Figure 2-4), where $F_E = K_{T0} + 1.5 K_{T0} f_E (K'_0 - 4)$. The intercept value, $F_E(0) = 162(\pm 2)$ GPa, agrees with K_{T0} obtained from the fit to the BM3 EoS, and the negative slope indicates K'_0 is smaller than 4 (Angel, 2000), which is consistent with our fitting results.

The EoS obtained by DFT-GGA (Oganov et al., 2006) and DFT-LDA (Marcondes et al., 2016) serve as upper and lower bounds of experimental measurements, respectively (Figure 2-3a). (Marcondes et al., 2016) provide the only previous predictions of the elastic shear properties of CaCO₃-*Pmmn*, which are necessary to directly compare our results for thermoelastic parameters derived by MGD EoS (discussed in the following section). We thus provide an additional fit to our 300 K P-V data with V0 fixed to 97.76 Å³ as predicted by DFT-LDA, yielding K70 = 146.7 (\pm 1.9)

GPa and $K'_0 = 3.4(\pm 0.1)$. Smaller K_{T0} and larger K'_0 relative to the unconstrained BM3 EoS are mainly due to the tradeoffs between V_0 , K_{T0} , and K'_0 (Figure 2-8). The modeled K_T at pressures from 50-80 GPa (black dashed line in Figure 2-3b) are consistent with the fits without a fixed V_0 .

2.4.3 Thermal equation of state of CaCO₃-Pmmn

To constrain the TEoS, unit-cell volumes for CaCO₃-Pmmn are collected up to 75 GPa and 2200 K (Table 2-3), with temperature determined by spectroradiometry and pressure measured using the TEoS of Au (Fei et al., 2007). We use two approaches to constrain high-temperature behavior: 1) obtaining thermal expansion coefficient (α_T) from fitting P-V-T data to a hightemperature BM3 EoS (HT-BM3 EoS) (Birch, 1952; Fei, 1995) (Figure 2-5a), and 2) obtaining Grüneisen parameter (y₀) from a Mie-Grüneisen-Debye equation of state (MGD EoS) (Jackson, 1998; Jackson & Rigden, 1996) (Figure 2-5b). Both the MGD EoS and HT-BM3 EoS models can mathematically describe our experimental measurements well (Figure 2-5), but have complementary strengths and weaknesses in terms of fitting tradeoffs, assumptions, and sensitivity to physically meaningful quantities. To be more specific, the MGD EoS formulation is based on statistical mechanics, i.e., Debye's approximation, but is not directly comparable to experiments; whereas the HT-BM3 EoS formulation is based on finite strain theory to empirically express experimental measurements, but can lead to poor extrapolation beyond experimental conditions (Poirier, 2000). Both models have been widely applied to materials in Earth sciences with thermodynamic databases used in geophysical studies, such as (Fabrichnaya et al., 2004) based on HT-BM3 EoS, and (Stixrude & Lithgow-Bertelloni, 2011) based on MGD EoS. We present both models to allow the reader to assess the effects of tradeoffs, and to directly use and compare our results to the previous results in these thermodynamic databases.

The HT-BM3 EoS is given by the following expression for P(V, T):

$$P(V,T) = \left(\frac{3}{2}\right) K_T \left[\left(\frac{V_{T,0}}{V}\right)^{\frac{7}{3}} - \left(\frac{V_{T,0}}{V}\right)^{\frac{5}{3}} \right] \left\{ 1 + \frac{3}{4} \left(K_T' - 4\right) \left[\left(\frac{V_{T,0}}{V}\right)^{\frac{2}{3}} - 1 \right] \right\},$$

where K_T denotes isothermal bulk modulus at ambient pressure and a given high temperature, $V_{T,0}$ is the ambient pressure volume, V is the high-pressure and temperature volume, and K_T' is the pressure derivative of K_{T0} at ambient pressure, neglecting higher-order pressure derivatives of the bulk modulus and assuming that K_T' is a constant in the temperature range of our study, i.e., K_0' . The temperature effect on K_T can be expressed as a linear function of temperature, with the temperature derivative at ambient pressure $(\partial K_T/\partial T)_P$ and K_{T0} as follow:

$$K_T = K_{T0} + (\partial K_T / \partial T)_P (T - T_0),$$

where T_0 is the reference temperature, 300 K. $(\partial K_T/\partial T)_P$ is assumed to be a constant within the temperature range of our study. The temperature dependence of the volume at ambient pressure, $V_{T,0}$, can be expressed as a function of the thermal expansion at zero pressure:

$$V_{T,0} = V_0 \exp\left(\int_{T_0}^T \alpha_T dT\right).$$

The thermal expansion coefficient α_T is expressed as $\alpha_T = (1/V)(\partial V/\partial T)_P$. At atmospheric pressure, α_T can be approximated to a linear function of temperature:

$$\alpha_T = a_0 + a_1 T,$$

where a_0 and a_1 are constants. By least-squares fitting with the parameters V_0 , K_{T0} and K'_0 fixed from the 300 K BM3 EoS, we obtained a_0 , a_1 , and $(\partial K_T/\partial T)_P$. We further fit the P-V-T data with a fixed V_0 to 97.76 Å³ alone, yielding K_{T0} , K'_0 , a_0 , a_1 , and $(\partial K_T/\partial T)_P$, which are consistent with the first fitting within uncertainties (Table 2-2). The isothermal compression curves for temperatures from 1300 to 2200 K at 300 K intervals were calculated from these thermoelastic parameters (Figure 2-5a). The fitting residuals indicate the discrepancies between measured and calculated

pressure are ranging from -1.7 to 1.4 GPa within the investigated pressure and temperature range (Figure 2-5a), indicating the fitted HT-BM3 EoS can describe our experimental measurements well.

In the MGD EoS, the total pressure P(V,T) is expressed as the sum of the static pressure at room temperature, $P(V,T_0)$, and the thermal pressure, $P_{th}(V,T)$:

$$P(V,T) = P(V,T_0) + P_{th}(V,T),$$

where $P(V,T_0)$ is fixed by BM3 EoS at 300 K, and the thermal pressure $P_{th}(V,T)$ is a function of the Grüneisen parameter γ and the thermal energy $E_{th}(V,T)$, that can be estimated using a Debye model:

$$P_{th}(V,T) = \frac{\gamma(V,T)}{V} [E_{th}(V,T) - E_{th}(V,T_0)],$$

$$E_{th}(V,T) = \frac{9nRT}{(\theta/T)^3} \int_0^{\theta/T} \frac{x^3}{e^{x-1}} dx,$$

where θ is the Debye temperature, n = 5 is the number of atoms in the formula unit, and R is the gas constant (8.314 J·mol⁻¹·K⁻¹). The volume dependence of the θ and γ are described by:

$$\theta = \theta_0 \exp\left(\frac{\gamma_0 - \gamma}{q}\right),$$

$$\gamma = \gamma_0 \left(\frac{V}{V_0}\right)^q,$$

where q is the dimensionless power mode parameter, γ_0 and θ_0 are Grüneisen parameter and Debye temperature at 300 K, respectively. As above, V_0 , K_{T0} , K'_0 are fixed from the 300 K EoS. The θ_0 can be evaluated more precisely from sound velocities using equations based on Debye's lattice vibration model (Poirier, 2000). With self-consistent elastic parameters at zero pressure $K_{S0} = 122$ GPa, $G_0 = 56$ GPa and $\rho_0 = 3.4$ g/cm³ reported by (Marcondes et al., 2016), the θ_0 for CaCO₃-Pmmn was estimated to be 631 K. Due to strong correlations between the three high-temperature parameters θ_0 , γ_0 and q, we fixed θ_0 and obtained the fitted $\gamma_0 = 1.94(\pm 0.02)$ and $q = 1.9(\pm 0.3)$. To

investigate the tradeoff between γ_0 and q, we further fix q=1 as a common assumption, yielding $\gamma_0=1.53(\pm 0.01)$. We also fit the P-V-T data with a fixed V_0 to 97.76 Å 3 and θ_0 to 631 K alone, yielding $K_{T0}=151(\pm 4)$ GPa, $K_0'=3.2(\pm 0.2)$, $\gamma_0=1.6(\pm 0.5)$ and $q=1.3(\pm 0.9)$, which are in agreement with the first fitting within uncertainties (Table 2-2). These thermoelastic parameters produce isothermal compression curves (Figure 2-5b) consistent with those obtained from HT-BM3 EoS (Figure 2-5a). The fitting residuals indicate the discrepancies between measured and calculated pressure are ranging from -1.7 to 1.7 GPa within the investigated pressure and temperature range (Figure 2-5b). In summary, both HT-BM3 EoS and MGD EoS results here comprise the first characterization of high-temperature properties of CaCO₃-Pmmn and can be used to model the chemical and physical properties of CaCO₃ in the lower mantle.

Neither of EoS yields a superior or significantly different fit to the experimental data (Figure 2-5) and the results for density and bulk sound velocity of CaCO₃-Pmmn are not significantly affected by the choice of EoS. Calculated densities and velocities follow geotherms from 45 to 80 GPa (Figure 2-6 and Figure 2-7), which does not extrapolate our experimental *P-T* conditions significantly and minimizes the potential errors produced by extrapolation of the thermal equation of state.

2.5 Implications

Due to the substantially lower density of carbonates than the principal constituents of the lower mantle (Figure 2-6), sufficient amounts of carbonates may be expected to affect the buoyancy of the subducting slab and its seismic signature, which would be the main manifestations that could be used to constrain the survival and behavior of carbonates subducted into Earth's lower mantle. Calcite/aragonite is one of the most abundant carbonates at shallow depths, along

with dolomite (CaMg(CO₃)₂) and magnesite (MgCO₃) (Luth, 1999). During subduction, CaMg(CO₃)₂ breaks down to MgCO₃ and CaCO₃ above 5 GPa (Luth, 2004). The two end-member carbonates, CaCO₃ and MgCO₃, have melting points above typical slab geotherms and thus have been suggested to remain stable in the lower mantle (Li et al., 2017; Solopova et al., 2014; Thomson et al., 2014), where they may be trapped in super-deep diamonds (Brenker et al., 2007; Bulanova et al., 2010; Tschauner et al., 2018). However, as these diamonds provide only samples of local composition that may not be typical of the mantle, geophysical methods may provide useful bounds on the abundance of these carbonates in the deep Earth. Key questions include what maximum amounts of each carbonate or mixture are consistent with observed behaviors and properties of subducting carbonate-bearing slabs in the transition zone and lower mantle.

To understand the dynamics and seismic signatures of subducting carbonate-bearing slabs, density (ρ) and bulk sound velocity (V_{Φ}) of CaCO₃ and MgCO₃ at relevant P-T conditions are firstly modeled based on the thermal equations of state. The bulk sound velocity is calculated by $V_{\Phi} = (K_S/\rho)^{1/2}$, where $K_S = K_{T0} (1+\alpha\gamma T)$, which are determined by HT-BM3 EoS and MGD EoS. Because the thermoelastic parameters of CaCO₃-P2 $_1$ /c-1 have not been constrained experimentally or theoretically, we cannot address the physical properties change due to phase transition from CaCO₃-P2 $_1$ /c-1 to CaCO₃-P2 $_1$ 0. The thermoelastic parameters used in the modeling of CaCO₃-P2 $_1$ 0 (Litasov et al., 2017a), CaCO₃-P2 $_1$ 1 (this study) and magnesite (MgCO₃-P3 $_1$ 2 (Litasov et al., 2008) are summarized in Table 2-2. A cold slab temperature profile [600 K cooler than normal mantle geotherm (Syracuse et al., 2010)] is considered in the model as a typical scenario most likely to retain carbonate minerals during subduction. The calculated ρ and V_{Φ} of CaCO₃ and MgCO₃ from 30 to 80 GPa are plotted in Figure 2-6, and both HT-BM3 EoS and MGD EoS of

CaCO₃ and MgCO₃ provide similar results. The phase transition of CaCO₃-*Pnma* to CaCO₃-*Pmmn* in our model leads to an increase in ρ by ~4.5% but a decrease in V_{Φ} by ~0.8%, consistent with previous modeled results (Bayarjargal et al., 2018; Litasov et al., 2017a). At mid-lower mantle conditions, the density of CaCO₃-*Pmmn* is higher than MgCO₃- $R\bar{3}$ c by ~10-12%, whereas the V_{Φ} is lower by ~9-11%. In comparison to surrounding "average" mantle represented by the Preliminary Reference Earth Model (Dziewonski & Anderson, 1981), pure CaCO₃ in the lower mantle exhibits V_{Φ} ~15% lower, while MgCO₃ has V_{Φ} closer to PREM (Figure 2-6b). As a result, slow seismic anomalies in the mid-lower mantle may be more likely to be associated with local enrichment in CaCO₃ than MgCO₃.

More realistically, CaCO₃ and MgCO₃ are components of carbonated mantle lithologies (Poli & Schmidt, 2002), and the role of these carbonates in changing properties of the subducting slabs may provide a way to estimate bounds on amounts of these carbonates. To determine the physical properties of carbon-bearing rocks in the lower mantle, we must account for geologically relevant mixtures of carbonates with the major mantle silicate and oxide phases (Poli & Schmidt, 2002). It is likely that the carbonate content of subducted rocks varies substantially, from a typical value of ~0.5 mol% for altered oceanic basalts, ranging up to ~10 mol.% due to local enrichment of carbonates (e.g., Alt & Teagle, 1999; Shilobreeva et al., 2011). The basalt part of the subducting slab transforms at lower mantle conditions to a mixture of bridgmanite, Ca-perovskite, stishovite and Al-bearing calcium-ferrite-type (cf-) silicate (Dorfman, 2016). Mixing this assemblage with carbonates will affect not only the chemical behavior of the rock but also its geophysical behavior. We thus model ρ and V_{Φ} profile of carbonated basalt in the lower mantle from 30 to 80 GPa along a cold slab geotherm (Syracuse et al., 2010) as a typical scenario. Thermoelastic parameters of relevant phases, including constituents of subducted slab (Stixrude & Lithgow-Bertelloni, 2011)

and a mixture CaCO₃-MgCO₃ used in the model are summarized in Table 2. CaCO₃ and MgCO₃ are added into the metamorphosed basalt assemblages as a 1:1 molar ratio in proportions of 0 (i.e., eclogite), 2, 5 and 10 mol.%, respectively. The bulk properties of carbonated basalt are calculated based on MGD EoS by using a Hashin-Shtrikman averaging scheme (Cottaar et al., 2014).

The comparison of the bulk sound velocity profile between eclogite and carbonatedeclogite illustrates the effects of carbonate on seismic signatures of the subducting slab. The modeled results show V_{Φ} of eclogite can be decreased by at most ~2.0 % with the presence of 10 mol.% carbonates in the case of maximum carbonate enrichment and zero loss of carbonate during subduction. Even for this extreme upper bound, the effect of CaCO₃ phase transition on the seismic velocity of the slab, increased by ~0.1%, is invisible (Figure 2-7a). In the case of typical 0.5 mol.% carbonates presence in the subducting slab, the V_{Φ} of eclogite would decrease by less than 0.1 %. Comparing to the ambient mantle profile (PREM), the subducting slabs exhibit high V_{Φ} zones, which cannot be changed by adding carbonates. Therefore, the presence of carbonates in the lower mantle is unlikely to be detected by seismic observation. Previous studies proposed that the presence of sufficient amounts (i.e., 10 mol.%) of carbonates would cause shear velocity discontinuities (decreased by 7%) due to CaCO₃-P2₁/c-l to CaCO₃-Pmmn phase transition (Bayarjargal et al., 2018), and largely localized anisotropy due to small shear modulus of MgCO₃ (Yao et al., 2018a). Although the region with >1% seismic velocity anomaly is detectable by seismic tomography (e.g., French & Romanowicz, 2015), considering the typical concentration and thickness of carbonate depositions on the oceanic crust, even the localized shear velocity anomaly or anisotropy caused by the presence of carbonates is unlikely detectable due to the limit of spatial resolution of seismic tomography.

The ρ contrast between carbonates and surrounding phases at lower mantle conditions is a source of buoyancy that impedes the downward motion of the slab. In comparison to the average mantle density profile (PREM), eclogite is denser than the ambient lower mantle by ~0.8 %, indicating the higher density of eclogite helps drive subduction in the lower mantle. However, the model results indicate the density of highly carbonated eclogite with maximum carbonate enrichment 10 mol.% carbonates are lower than the ambient lower mantle by ~0.6 % (Figure 2-7b), and thus will not sink. The maximum amount of carbonate stored in eclogite that will not contribute to slab stagnation is 5 mol.%. This is also much greater than the typical 0.5% carbonate content in altered oceanic crust. The temperature effects on the density of subducting slab are negligible, i.e., the calculated density of eclogite decreases by ~1% when changing the reference geotherm from cold slab to hot slab [300 K cooler than normal mantle geotherm (Syracuse et al., 2010)]. In addition, the buoyancy of carbonates is not expected to significantly affect the dynamics of subducting slabs relative to other metastable components of cold slabs potentially present in far greater abundance, particularly metastable olivine (Rubie & Ross, 1994) and pyroxene (van Mierlo et al., 2013).

Thermoelastic properties of CaCO₃-Pmmn provide useful geochemical constraints necessary for modeling the phase equilibria of carbonates with mantle phases at lower mantle conditions. Reactions that control the presence of CaCO₃ in the slab include melting, decarbonation and redox interactions with ambient mantle phases. For example, recent experimental studies suggest the CaCO₃ decarbonation occurs in the presence of silica at lower mantle conditions forming Ca-perovskite and CO₂ (Drewitt et al., 2019; Li et al., 2018), and the redox reaction between CaCO₃ and metallic iron in the ambient mantle is proposed to be a mechanism of deep diamond formation (Martirosyan et al., 2016; Palyanov et al., 2013). The P-T

boundaries of both reactions are essential to understanding the fate of subducted CaCO₃ and equilibrium between CaCO₃ and mantle phases. However, both boundaries are not well constrained by experiments, mainly due to the kinetic barriers in reactions and uncertainties in pressure and temperature measurements. For other lower mantle phases, thermodynamic modeling has begun to be used to construct physically-consistent phase diagrams (e.g., Stixrude & Lithgow-Bertelloni, 2011). The newly determined thermoelastic parameters of CaCO₃-Pmmn combined with those of other mantle phases will contribute to more quantitative constraints on phase equilibria in the carbonate-silicate system at lower mantle conditions.

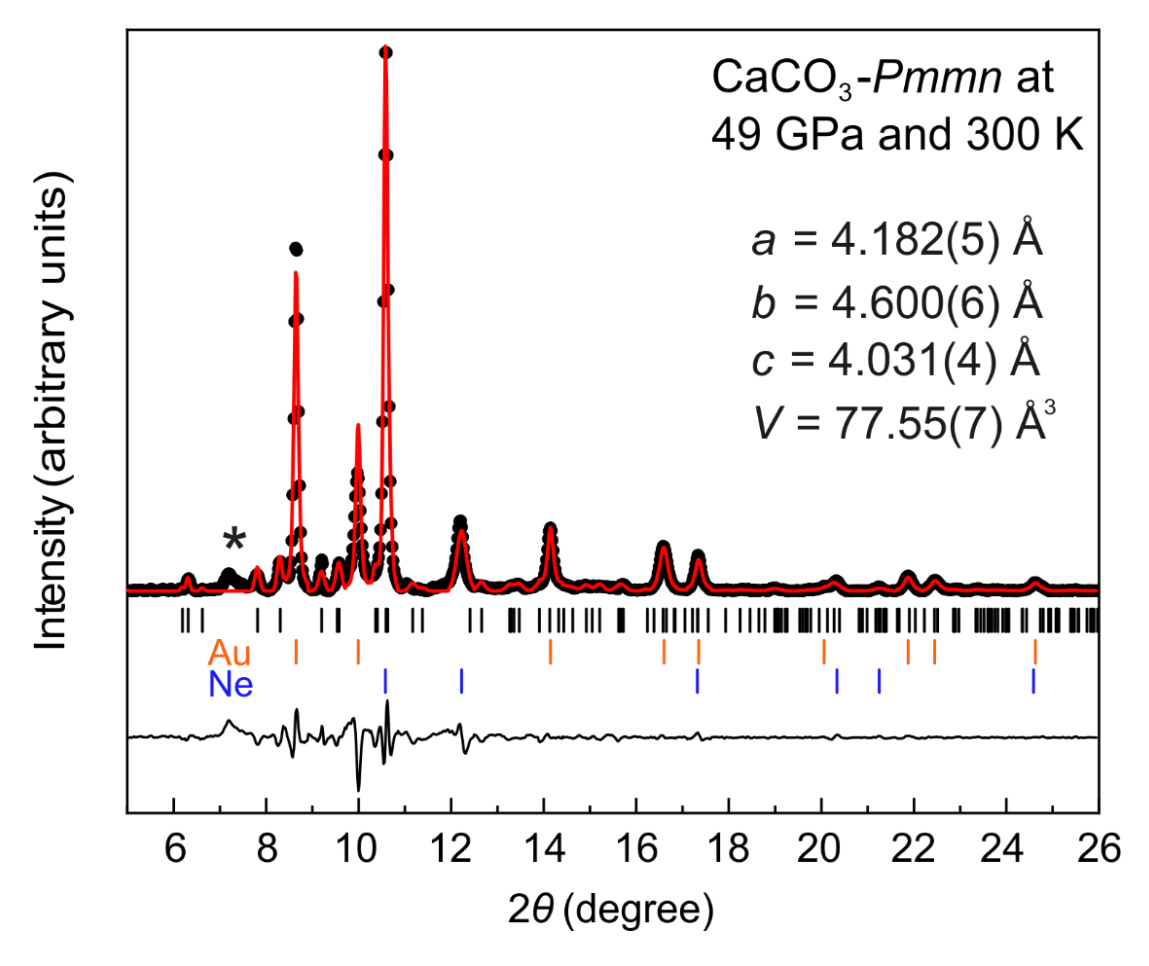


Figure 2-1: Full-profile Le Bail refinement confirms the synthesis of $CaCO_3$ -Pmmn. Measured XRD data for the quenched sample after heating at 49 GPa and 300 K (black dots) are consistent with orthorhombic post-aragonite structure (space group Pmmn with Z=2) (black ticks below). Le Bail fit (red curve) also includes expected peak positions for Au calibrant (yellow sticks) and Ne medium (blue ticks). One unknown peak at 2θ around ~7° (marked by an asterisk) may be from the metastable $CaCO_3$ - $P2_1/c$ -1 due to kinetics. The wavelength of the monochromatic X-ray beam is 0.3344 Å.

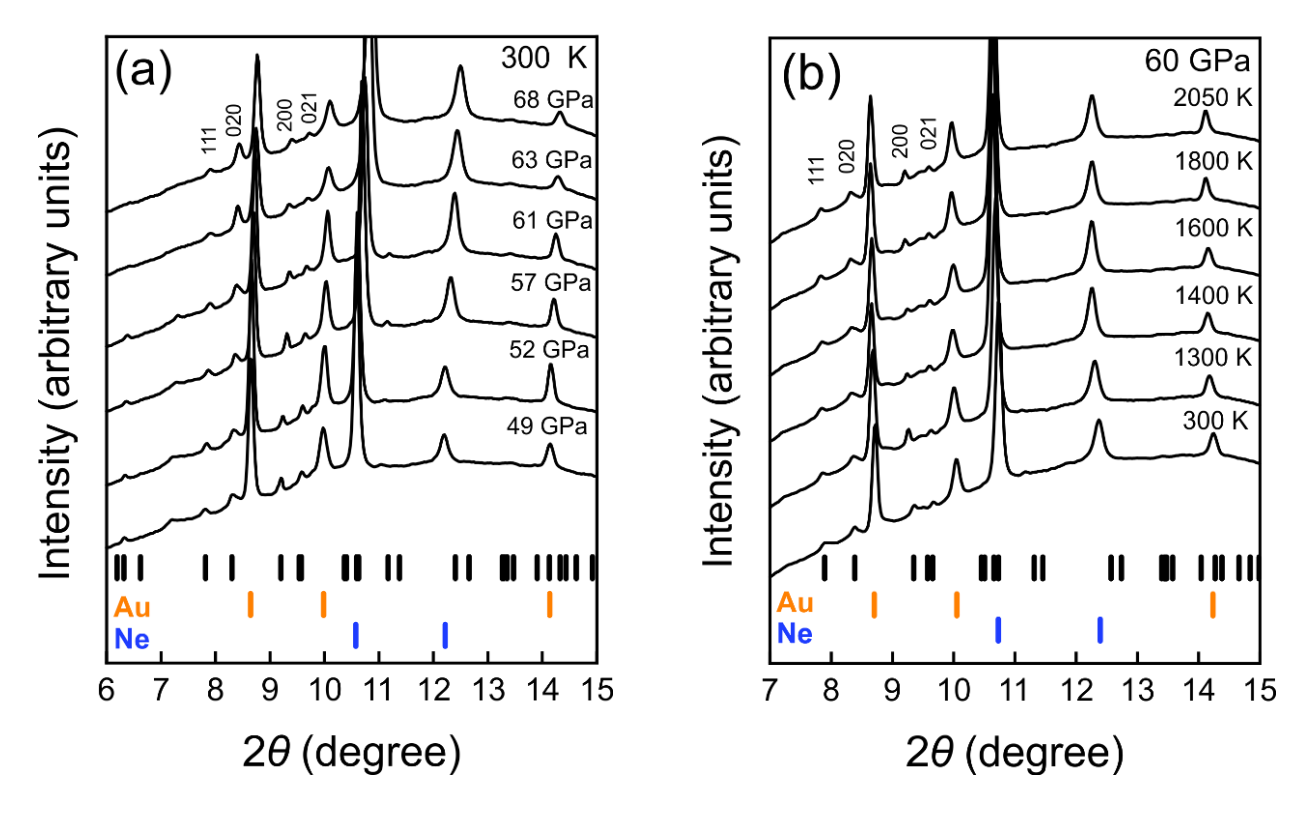


Figure 2-2: Representative in-situ X-ray diffraction patterns of CaCO₃-*Pmmn*. (a) Representative in-situ X-ray diffraction patterns of CaCO₃-*Pmmn* measured at high pressures and room temperature (black marker). (b) Representative high-temperature X-ray diffraction patterns of CaCO₃-*Pmmn* at ~60 GPa (black marker) measured in-situ in a laser-heated diamond anvil cell. In all XRD patterns, Au was used as the internal pressure calibrant (Fei et al., 2007) and laser-absorber (orange marker), while Ne was used as the thermal insulator and pressure medium (blue marker). The wavelength of the monochromatic X-ray beam is 0.3344 Å.

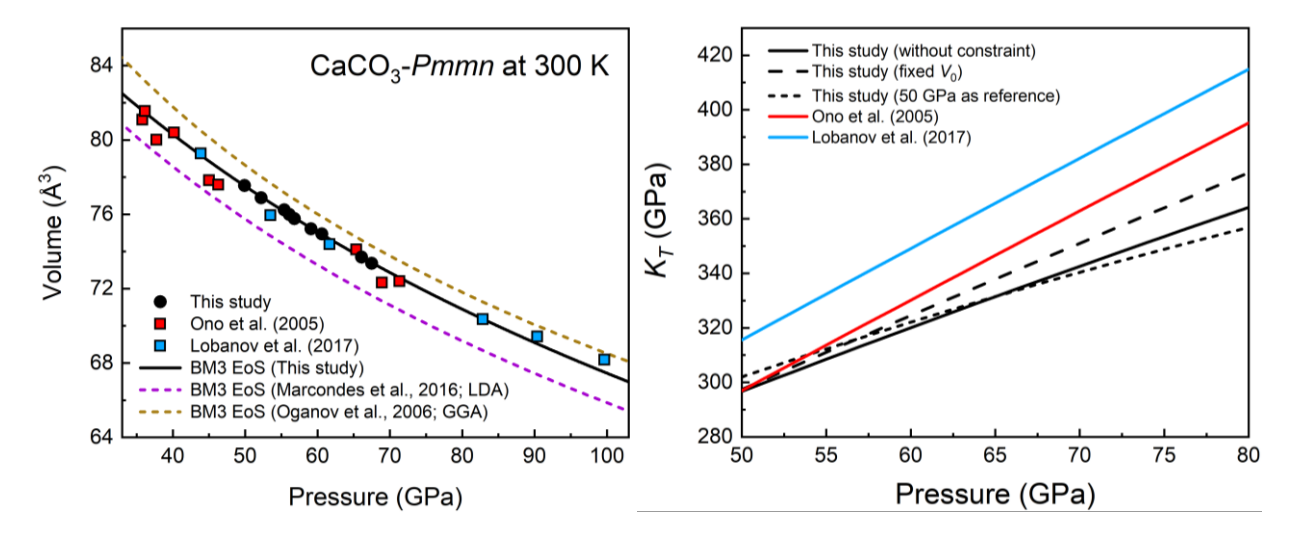


Figure 2-3: Equation of state of CaCO₃-pmmn. (a) Pressure-volume data for CaCO₃-Pmmn at room temperature from this study (black circle) and previous studies. Data from Ono et al. (2005) (red square) and Lobanov et al. (2017) (blue square) were recalculated using Pt pressure scale (Fei et al., 2007). Black solid curve (this study) is modeled by BM3 EoS using $K_{T0} = 162(\pm 62)$ GPa, $K'_0 = 3.1$ (± 1.1), and $V_0 = 96.6(\pm 4.8)$ Å³. A brown dashed curve (Oganov et al., 2006) and a purple dashed curve (Marcondes et al., 2016) modeled by BM3 EoS constrained via DFT-GGA and LDA, respectively. (b) Isothermal bulk modulus (K_T) at 300 K calculated by BM3 EoS. The black solid line, dashed line and short-dashed line represent the BM3 EoS fittings without constraint, with a fixed $V_0 = 97.76$ Å³ and with reference pressure set at 50 GPa.

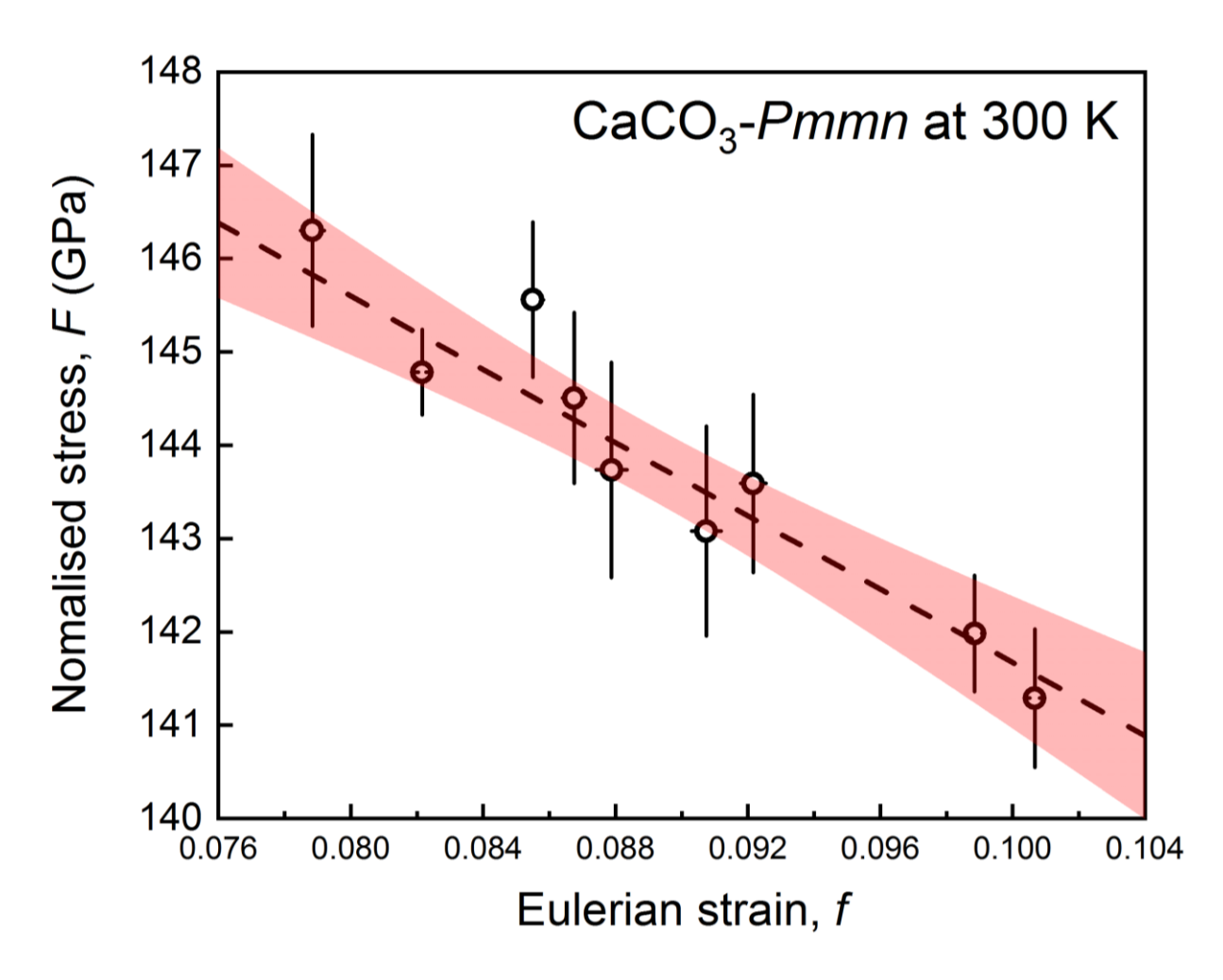


Figure 2-4: Volume Eulerian strain (f) - normalized pressure (F) plot of CaCO₃-Pmmn. The dashed line represents the linear fit through the data, and a red envelope indicates 95% confidence interval. The V_0 was set as 96.6 Å³ obtained by BM3 EoS fitting of experimental data at 300 K.

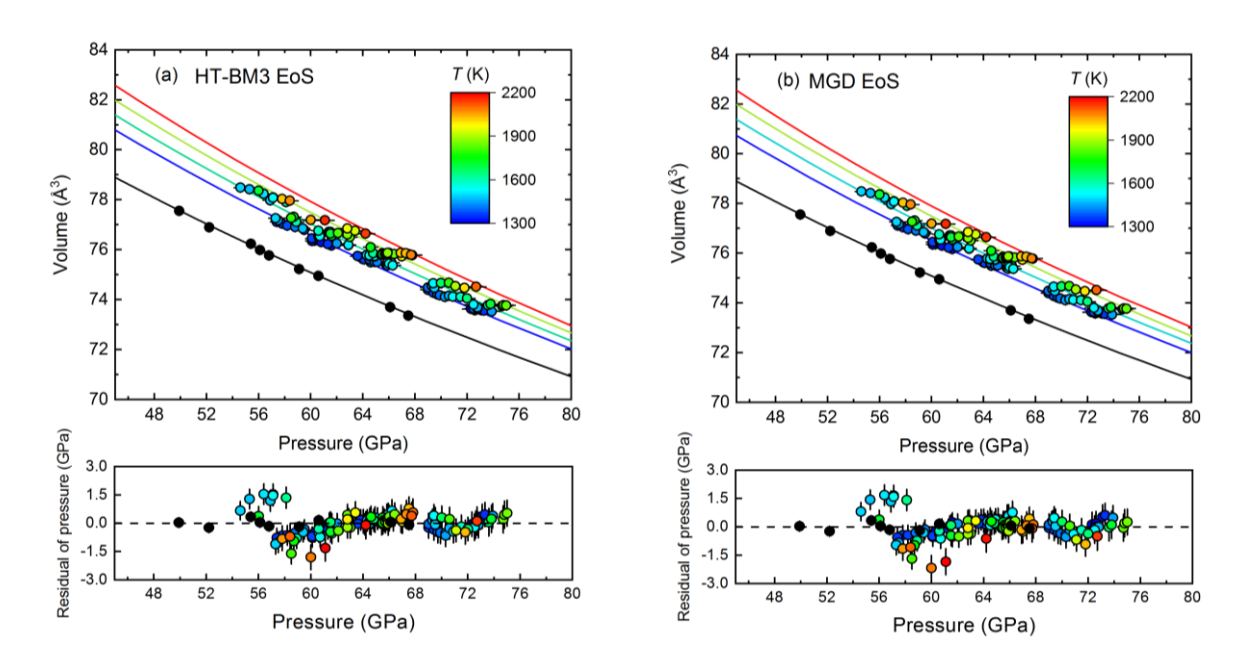


Figure 2-5: Measured pressure-volume-temperature data for CaCO₃-*Pmmn*. Colorful curves are isotherms at 1300, 1600, 1900, 2200 K modeled by (a) HT-BM3 EoS and (b) MGD EoS, respectively, with parameters listed in Table 2-2. Black points and curve are at 300 K same as Figure 2-3. The lower panel of each figure shows fitting residuals.

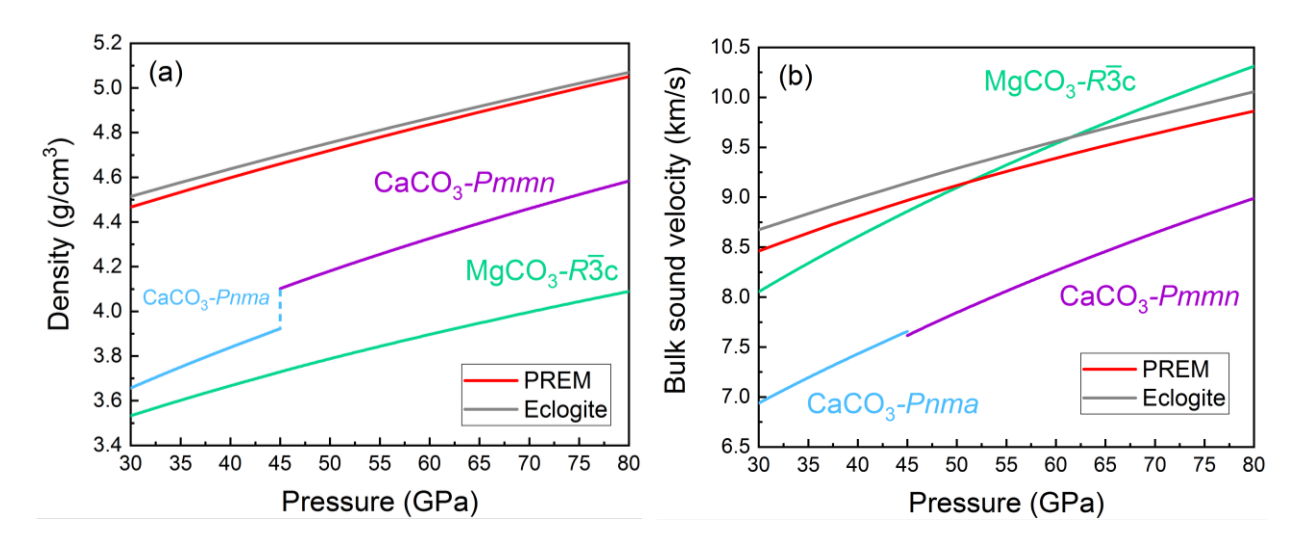


Figure 2-6: Modeled (a) density and (b) bulk sound velocity profiles of CaCO₃ and MgCO₃ from 30 to 80 GPa along mantle geotherm (Brown & Shankland, 1981) compared to PREM model (Dziewonski & Anderson, 1981) and eclogite (assumed to be composed by 27 mol.% bridgmanite [(Mg_{0.9},Fe_{0.1})SiO₃], 24 mol.% Ca-perovskite (CaSiO₃), 20 mol.% stishovite (SiO₂), 29 mol.% Albearing calcium-ferrite-type silicate [(Mg_{0.9},Fe_{0.1})Al₂O₄]), using the thermoelastic parameters listed in Table 2-2. In order to clearly illustrate the density contrast of different carbonates, the phase transition of CaCO₃-*Pnma* to CaCO₃-*Pmmn* is assumed to occur at 45 GPa.

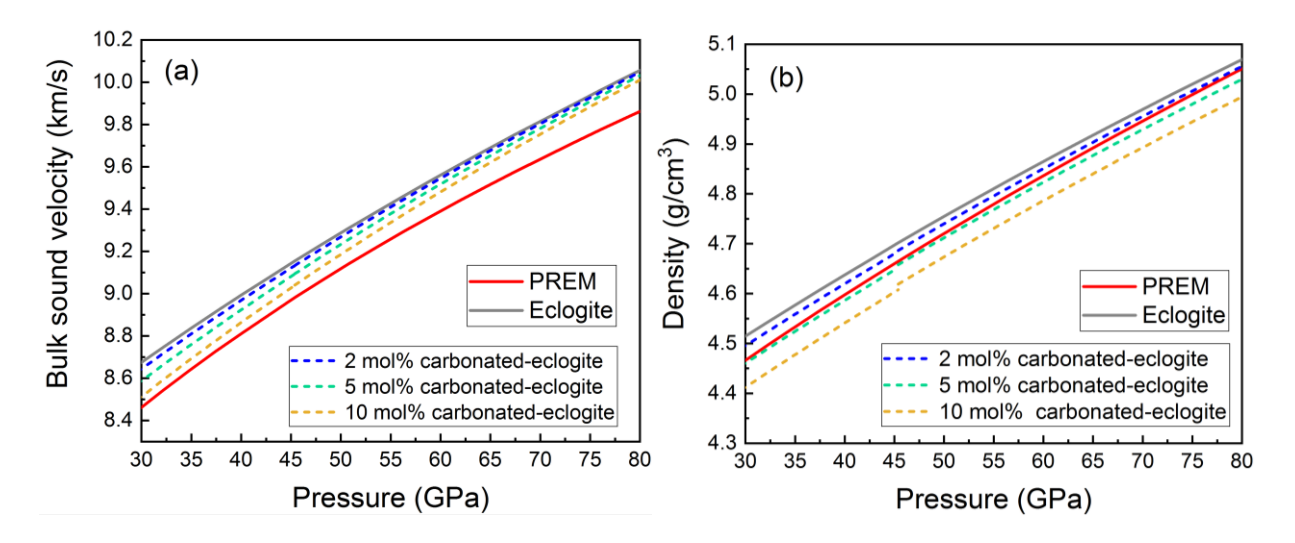


Figure 2-7: Modeled (a) bulk sound velocity and (b) density profiles of eclogite and carbonated-eclogite with the presence of CaCO₃-MgCO₃ mixture as 2, 5 and 10 mol.%, respectively. The eclogite is assumed to be composed by 27 mol.% bridgmanite [(Mg_{0.9},Fe_{0.1})SiO₃], 24 mol.% Caperovskite (CaSiO₃), 20 mol.% stishovite (SiO₂), 29 mol.% Al-bearing calcium-ferrite-type silicate [(Mg_{0.9},Fe_{0.1})Al₂O₄], and the thermoelastic parameters of these phases are listed in Table 2-2. The pressure is ranging from 30 to 80 GPa along cold geotherm (Syracuse et al., 2010). The CaCO₃-Pnma to CaCO₃-Pmmn transition is assumed to occur at 45 GPa. The PREM model (Dziewonski & Anderson, 1981) is plotted as a comparison of the averaged mantle.

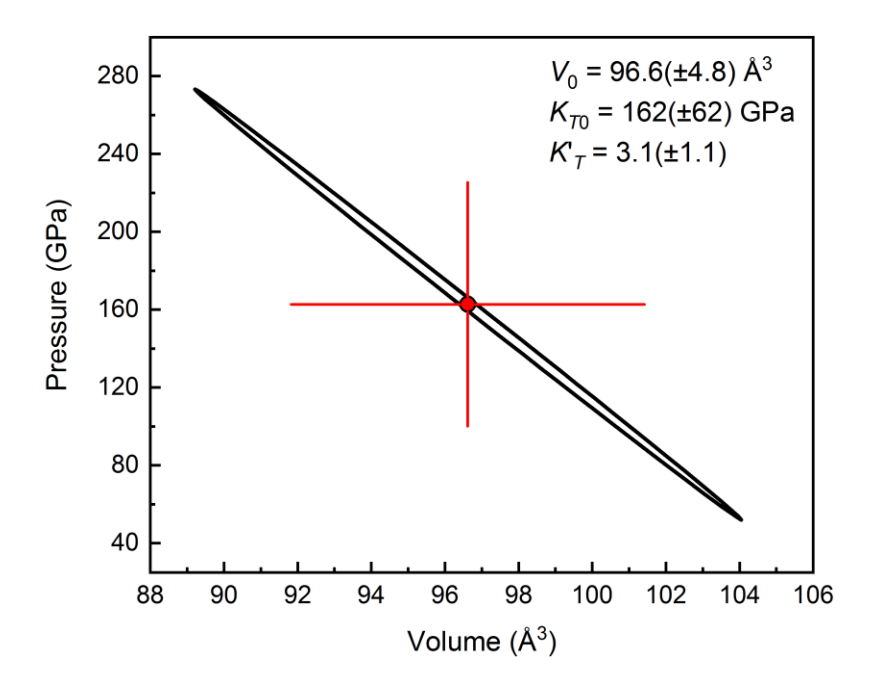


Figure 2-8: The correlation between the fitted V_0 and K_{T0} of CaCO₃-*Pmmn* at 300 K using BM3 EoS. The red circle indicates the fitting result and black ellipsoid represents 95% confidence interval.

Table 2-1: Comparison of parameters of BM3 EoS of CaCO₃-Pmmn at 300 K.

| V_0 (Å ³) | K _{T0} (GPa) | K_0' | Method | References |
|-------------------------|-----------------------|-----------|------------------------------|--------------------------------|
| 99.4(20) | 118(14) | 4 (fixed) | XRD (PM ² : NaCl) | Ono et al. (2005) ³ |
| 97.3(16) | 135(12) | 4 (fixed) | XRD (No PM) | Lobanov et al. $(2017)^3$ |
| 109.74 | 65.4 | 4.94 | DFT-GGA ⁴ | Oganov et al. (2006) |
| 97.76 | 122 | 3.732 | DFT-LDA ⁴ | Marcondes et al. (2016) |
| 96.6(48) | 162(62) | 3.1(11) | XRD (PM: Ne) ⁵ | This study |
| 97.76 (fixed) | 146.7(19) | 3.4(1) | XRD (PM: Ne) ⁵ | This study |

Numbers in parentheses are uncertainties on the last digits.

PM: pressure medium

Refitted by the pressure scale of Pt (Fei et al., 2007).

Results are from 0 K.

⁵ Using the pressure scale of Au (Fei et al., 2007).

Table 2-2: Thermoelastic parameters of CaCO₃, MgCO₃, and major components in eclogite.

| Sample | V_0 | K_{T0} | K_0' | $\partial K_T/\partial T$ | a_0 | a_1 | θ_0 | γο | q |
|--|--------------------|---------------|------------|---------------------------|---------------------------|---------------------------|------------------|----------|----------------|
| | (\mathring{A}^3) | (GPa) | _ | $(GPa\cdot K^{-1})$ | (10^{-5}K^{-1}) | (10^{-8}K^{-2}) | (K) | | |
| CaCO ₃ -Pmmn ¹ | 97.76 ⁵ | $146.7(19)^5$ | $3.4(1)^5$ | -0.021(1) | 4.3(3) | 0.8(2) | 631 ⁵ | 1.94(2) | 1.9(3) |
| CaCO ₃ -Pmmn ¹ | 97.76 ⁵ | 146(5) | 3.4(2) | -0.022(8) | 4.4(5) | 0.9(8) | - | - | - |
| CaCO ₃ -Pmmn ¹ | 97.76^{5} | 151(4) | 3.2(2) | - | - | - | 631 ⁵ | 1.6(5) | 1.3(9) |
| CaCO ₃ -Pmmn ¹ | 97.76^{5} | $146.7(19)^5$ | $3.4(1)^5$ | - | - | - | 631 ⁵ | 1.53(1) | 1 ⁵ |
| CaCO ₃ -Pnma ² | $227.11(3)^6$ | 67.0(8) | 4.74(12) | -0.016(1) | 4.95(22) | 2.77(40) | 516 ⁵ | 1.39(1) | 1 ⁵ |
| $MgCO_3-R\bar{3}c^3$ | 279.55(2) | 97.1(5) | 5.44(7) | -0.013(1) | 4.03(7) | 0.49(10) | 747^{5} | 1.38(1) | 1 ⁵ |
| MgSiO ₃ | 162.40 | 251(3) | 4.1(1) | | | | 905(5) | 1.57(5) | 1.1(3) |
| (perovskite) ⁴ | | | | | | | | | |
| FeSiO ₃ (perovskite) ⁴ | 169.31 | 272(40) | 4.1(10) | | | | 871(26) | 1.57(30) | 1.1(10) |
| $MgAl_2O_4$ (cf) ⁴ | 480.63 | 211(1) | 4.1(1) | | | | 838(16) | 1.31(30) | 1.0(10) |
| $FeAl_2O_4$ (cf) ⁴ | 494.97 | 211 (10) | 4.1(10) | | | | 804(69) | 1.31(30) | 1.0(10) |
| CaSiO ₃ (perovskite) ⁴ | 45.58 | 236 (4) | 3.9 (2) | | | | 796 (44) | 1.89 (7) | 0.9 (16) |
| SiO ₂ (stishovite) ⁴ | 46.56 | 314(8) | 3.8(1) | | | | 1108(13) | 1.37(17) | 2.8(22) |

¹ This study. ² Litasov et al. (2017). ³ Litasov et al. (2008).

⁴ Stixrude and Lithgow-Bertelloni (2011).
⁵ Fixed during fitting.
⁶ Numbers in parentheses are uncertainties on the last digits

Table 2-3: Unit cell parameters of CaCO₃-*Pmmn* at different *P-T* conditions.

| T (K) | P (GPa) | $\frac{\text{rs of CaCO}_3\text{-}Pmmn}{V(\text{Å}^3)}$ | $\frac{\text{at different } P-I}{a(\text{Å})}$ | b (Å) | c (Å) |
|------------|----------------------|---|--|----------|----------|
| 298 | 49.9(1) ^a | 77.55(7) | 4.182(5) | 4.600(6) | 4.031(4) |
| 298 298 | 52.2(1) | 76.89(2) | 4.162(3) 4.155(2) | 4.600(6) | 4.031(4) |
| 298 | 55.4(1) | 76.23(6) | 4.132(4) | 4.594(5) | 4.014(9) |
| 298 | 56.1(2) | 75.99(7) | 4.132(4) | 4.589(5) | 4.013(9) |
| 298 | 56.8(2) | 75.77(9) | 4.127(3) | 4.589(3) | 4.008(9) |
| 298 | 59.1(2) | 75.22(9) | 4.121(7) | 4.574(7) | 4.007(9) |
| 298 | 60.6(2) | 74.95(7) | 4.104(0) | 4.576(6) | 3.994(9) |
| 298 | 66.1(2) | 73.70(4) | 4.102(3) | 4.558(3) | 3.967(9) |
| 298 | 67.5(3) | 73.36(3) | 4.075(3) | 4.548(2) | 3.968(6) |
| 1308(100) | 60.3(5) | 76.36(6) | 4.144(4) | 4.595(5) | 4.010(9) |
| 1317(100) | 60.1(5) | 76.35(4) | 4.145(3) | 4.597(3) | 4.007(9) |
| 1317(100) | 72.3(7) | 73.63(4) | 4.076(2) | 4.554(3) | 3.967(9) |
| 1320(100) | 61.6(5) | 76.17(5) | 4.135(4) | 4.592(4) | 4.012(9) |
| 1322(100) | 72.6(6) | 73.58(3) | 4.073(2) | 4.553(3) | 3.967(9) |
| 1326(100) | 60.8(5) | 76.30(7) | 4.143(5) | 4.597(6) | 4.007(9) |
| 1340(100) | 73.1(6) | 73.57(3) | 4.073(2) | 4.552(2) | 3.968(9) |
| 1348(100) | 64.0(6) | 75.62(8) | 4.117(5) | 4.578(6) | 4.013(9) |
| 1353(100) | 64.0(5) | 75.67(8) | 4.118(5) | 4.578(6) | 4.015(9) |
| 1354(100) | 63.8(5) | 75.72(9) | 4.119(6) | 4.578(7) | 4.015(9) |
| 1358(100) | 73.3(6) | 73.57(5) | 4.072(4) | 4.552(4) | 3.970(9) |
| 1360(100) | 57.8(5) | 77.04(5) | 4.155(3) | 4.606(4) | 4.025(9) |
| 1360(100) | 57.4(5) | 77.11(4) | 4.158(3) | 4.607(3) | 4.026(9) |
| 1360(100) | 61.3(5) | 76.22(4) | 4.140(3) | 4.594(3) | 4.007(9) |
| 1362(100) | 69.2(6) | 74.41(1) | 4.103(1) | 4.564(1) | 3.974(3) |
| 1366(100) | 69.4(6) | 74.28(2) | 4.102(1) | 4.565(2) | 3.967(4) |
| 1366(100) | 69.0(6) | 74.40(6) | 4.103(1) | 4.565(1) | 3.972(5) |
| 1368(100) | 72.6(7) | 73.60(2) | 4.075(2) | 4.554(2) | 3.966(9) |
| 1369(100) | 60.1(5) | 76.45(6) | 4.147(4) | 4.597(4) | 4.010(9) |
| 1369(100) | 64.1(6) | 75.61(8) | 4.117(5) | 4.577(6) | 4.013(9) |
| 1372(100) | 63.6(5) | 75.74(7) | 4.119(5) | 4.578(6) | 4.016(9) |
| 1374(100) | 58.2(5) | 76.96(5) | 4.155(3) | 4.605(4) | 4.022(9) |
| 1378(100) | 64.6(6) | 75.50(8) | 4.115(6) | 4.577(6) | 4.009(9) |
| 1381(100) | 64.5(6) | 75.60(8) | 4.115(5) | 4.576(6) | 4.015(9) |
| 1392(100) | 64.5(6) | 75.61(8) | 4.116(6) | 4.577(6) | 4.013(9) |
| 1393(100) | 69.7(6) | 74.22(4) | 4.100(3) | 4.565(3) | 3.965(8) |
| 1396(100) | 72.5(7) | 73.65(2) | 4.076(2) | 4.554(2) | 3.968(9) |
| 1402(100) | 69.0(6) | 74.49(3) | 4.104(1) | 4.565(2) | 3.976(6) |
| 1405(100) | 69.9(6) | 74.18(3) | 4.100(2) | 4.565(3) | 3.963(7) |
| 1414(100) | 64.9(6) | 75.51(8) | 4.113(6) | 4.576(6) | 4.012(9) |
| 1415(100) | 58.8(5) | 76.90(4) | 4.154(3) | 4.605(3) | 4.021(9) |
| 1422(100) | 65.1(6) | 75.51(9) | 4.113(6) | 4.575(7) | 4.013(9) |
| 1429(100) | 59.5(5) | 76.79(4) | 4.151(3) | 4.603(3) | 4.019(8) |
| | | | | | |

| Table 2-3 (co | ont'd) | | | | |
|---------------|---------|----------|----------|----------|----------|
| 1430(100) | 65.8(6) | 75.40(9) | 4.109(7) | 4.574(7) | 4.011(9) |
| 1431(100) | 72.8(7) | 73.64(2) | 4.077(1) | 4.554(1) | 3.967(3) |
| 1438(100) | 62.0(5) | 76.24(5) | 4.139(4) | 4.593(4) | 4.011(9) |
| 1440(100) | 70.3(6) | 74.13(3) | 4.100(2) | 4.565(2) | 3.961(6) |
| 1445(100) | 70.3(6) | 74.10(2) | 4.098(1) | 4.564(2) | 3.962(4) |
| 1448(100) | 73.9(6) | 73.53(5) | 4.071(3) | 4.552(4) | 3.968(9) |
| 1456(100) | 57.5(5) | 77.17(4) | 4.163(3) | 4.609(3) | 4.022(8) |
| 1463(100) | 72.8(7) | 73.69(2) | 4.079(1) | 4.554(1) | 3.967(4) |
| 1467(100) | 70.6(6) | 74.15(2) | 4.098(1) | 4.564(1) | 3.965(3) |
| 1467(100) | 69.3(6) | 74.55(1) | 4.105(1) | 4.565(1) | 3.979(3) |
| 1471(100) | 55.3(5) | 78.42(4) | 4.199(3) | 4.619(3) | 4.044(9) |
| 1472(100) | 60.6(5) | 76.53(5) | 4.147(3) | 4.596(4) | 4.015(9) |
| 1479(100) | 59.4(5) | 76.85(4) | 4.152(3) | 4.604(3) | 4.020(7) |
| 1485(100) | 56.9(6) | 77.98(6) | 4.185(4) | 4.616(4) | 4.036(9) |
| 1485(100) | 69.5(6) | 74.55(4) | 4.105(1) | 4.565(3) | 3.979(7) |
| 1489(100) | 69.5(6) | 74.48(3) | 4.104(1) | 4.565(3) | 3.975(3) |
| 1490(100) | 65.9(6) | 75.37(7) | 4.111(5) | 4.576(6) | 4.007(9) |
| 1492(100) | 57.3(5) | 77.26(5) | 4.164(3) | 4.609(3) | 4.025(9) |
| 1492(100) | 64.3(6) | 75.79(7) | 4.122(5) | 4.579(5) | 4.016(9) |
| 1495(100) | 54.6(5) | 78.49(3) | 4.200(2) | 4.619(2) | 4.046(6) |
| 1500(100) | 56.4(5) | 78.24(3) | 4.193(2) | 4.616(3) | 4.042(7) |
| 1506(100) | 64.5(6) | 75.75(7) | 4.121(5) | 4.579(5) | 4.014(9) |
| 1507(100) | 62.9(5) | 76.18(6) | 4.134(4) | 4.591(5) | 4.014(9) |
| 1509(100) | 65.9(6) | 75.49(9) | 4.112(7) | 4.575(7) | 4.013(9) |
| 1511(100) | 64.6(6) | 75.74(7) | 4.121(4) | 4.579(5) | 4.013(9) |
| 1516(100) | 66.2(6) | 75.48(9) | 4.111(7) | 4.575(8) | 4.014(9) |
| 1521(100) | 69.4(6) | 74.65(4) | 4.105(1) | 4.566(3) | 3.984(8) |
| 1522(100) | 62.9(5) | 76.20(7) | 4.136(5) | 4.593(5) | 4.011(9) |
| 1523(100) | 72.5(7) | 73.80(4) | 4.082(3) | 4.555(3) | 3.970(9) |
| 1526(100) | 70.9(6) | 74.12(3) | 4.098(2) | 4.564(3) | 3.963(7) |
| 1529(100) | 57.1(6) | 78.09(6) | 4.187(4) | 4.615(4) | 4.041(9) |
| 1532(100) | 64.9(6) | 75.73(6) | 4.121(4) | 4.580(5) | 4.013(9) |
| 1533(100) | 57.1(6) | 78.08(5) | 4.187(4) | 4.615(4) | 4.041(9) |
| 1538(100) | 66.0(6) | 75.44(8) | 4.112(5) | 4.576(6) | 4.010(9) |
| 1542(100) | 60.7(5) | 76.54(6) | 4.149(4) | 4.597(4) | 4.013(9) |
| 1542(100) | 66.3(6) | 75.37(8) | 4.110(6) | 4.575(6) | 4.008(9) |
| 1543(100) | 64.9(6) | 75.74(8) | 4.120(5) | 4.578(6) | 4.015(9) |
| 1544(100) | 64.5(6) | 75.77(7) | 4.122(5) | 4.580(5) | 4.013(9) |
| 1582(100) | 71.5(6) | 74.11(2) | 4.097(1) | 4.564(1) | 3.963(4) |
| 1594(100) | 60.6(5) | 76.76(2) | 4.151(2) | 4.604(2) | 4.016(5) |
| 1615(100) | 58.9(5) | 77.11(4) | 4.159(3) | 4.609(3) | 4.022(9) |
| 1620(100) | 58.1(6) | 77.91(7) | 4.184(5) | 4.616(5) | 4.035(9) |
| 1629(100) | 64.8(6) | 75.86(6) | 4.127(4) | 4.581(5) | 4.013(9) |

| Table 2-3 (co | ont'd) | | | | |
|---------------|---------|----------|----------|----------|----------|
| 1648(100) | 61.4(6) | 76.72(2) | 4.149(2) | 4.601(2) | 4.019(5) |
| 1648(100) | 72.0(5) | 74.05(4) | 4.096(3) | 4.564(3) | 3.961(9) |
| 1655(100) | 61.5(6) | 76.71(3) | 4.147(2) | 4.600(2) | 4.021(6) |
| 1656(100) | 73.6(7) | 73.77(3) | 4.082(1) | 4.555(2) | 3.968(4) |
| 1661(100) | 70.0(6) | 74.67(2) | 4.105(1) | 4.565(1) | 3.985(3) |
| 1673(100) | 61.6(5) | 76.56(4) | 4.149(3) | 4.597(3) | 4.014(9) |
| 1701(100) | 61.5(5) | 76.65(4) | 4.151(3) | 4.598(3) | 4.016(8) |
| 1704(100) | 73.8(7) | 73.82(2) | 4.082(2) | 4.555(2) | 3.970(5) |
| 1705(100) | 56.0(5) | 78.36(3) | 4.201(2) | 4.622(3) | 4.036(7) |
| 1728(100) | 65.4(6) | 75.80(6) | 4.126(4) | 4.581(5) | 4.010(9) |
| 1731(100) | 65.5(6) | 75.86(7) | 4.126(5) | 4.581(6) | 4.014(9) |
| 1734(100) | 64.6(6) | 76.10(5) | 4.133(4) | 4.591(4) | 4.011(9) |
| 1736(100) | 65.6(6) | 75.81(7) | 4.125(5) | 4.581(6) | 4.011(9) |
| 1740(100) | 58.7(6) | 77.31(4) | 4.165(3) | 4.609(3) | 4.027(9) |
| 1748(100) | 65.5(6) | 75.81(7) | 4.127(5) | 4.582(5) | 4.009(9) |
| 1785(100) | 65.7(6) | 75.83(6) | 4.127(4) | 4.581(5) | 4.010(9) |
| 1790(100) | 65.8(6) | 75.85(6) | 4.127(4) | 4.582(5) | 4.011(9) |
| 1792(100) | 58.5(6) | 77.27(5) | 4.168(3) | 4.612(4) | 4.020(9) |
| 1798(100) | 70.6(6) | 74.68(4) | 4.105(1) | 4.566(4) | 3.985(4) |
| 1813(100) | 74.7(7) | 73.74(2) | 4.080(1) | 4.555(1) | 3.968(3) |
| 1814(100) | 62.1(6) | 76.67(2) | 4.153(1) | 4.595(1) | 4.017(4) |
| 1816(100) | 65.9(6) | 75.85(6) | 4.127(4) | 4.581(5) | 4.012(9) |
| 1819(100) | 66.0(6) | 75.87(7) | 4.127(5) | 4.581(5) | 4.013(9) |
| 1820(100) | 74.8(7) | 73.78(1) | 4.082(1) | 4.554(1) | 3.969(3) |
| 1824(100) | 62.8(6) | 76.72(3) | 4.147(2) | 4.601(2) | 4.021(6) |
| 1832(100) | 75.0(7) | 73.77(3) | 4.083(3) | 4.554(3) | 3.967(8) |
| 1835(100) | 63.0(6) | 76.51(5) | 4.147(4) | 4.597(4) | 4.013(9) |
| 1840(100) | 66.4(6) | 75.82(7) | 4.126(5) | 4.581(5) | 4.012(9) |
| 1866(100) | 62.8(6) | 76.61(4) | 4.150(3) | 4.598(3) | 4.015(8) |
| 1873(100) | 65.9(6) | 75.87(7) | 4.128(5) | 4.583(6) | 4.011(9) |
| 1897(100) | 71.1(6) | 74.54(4) | 4.105(1) | 4.567(1) | 3.976(2) |
| 1937(100) | 63.4(6) | 76.75(3) | 4.147(2) | 4.601(3) | 4.023(7) |
| 1956(100) | 62.8(6) | 76.84(4) | 4.152(3) | 4.605(3) | 4.019(8) |
| 1962(100) | 67.0(6) | 75.74(6) | 4.128(4) | 4.582(4) | 4.004(9) |
| 1992(100) | 67.5(6) | 75.83(6) | 4.126(4) | 4.582(5) | 4.011(9) |
| 1999(100) | 71.8(6) | 74.47(2) | 4.105(2) | 4.567(2) | 3.972(5) |
| 2015(150) | 66.9(7) | 75.87(6) | 4.128(4) | 4.583(5) | 4.010(9) |
| 2029(150) | 57.8(6) | 78.03(2) | 4.192(1) | 4.623(1) | 4.026(1) |
| 2037(150) | 67.3(7) | 75.86(6) | 4.128(4) | 4.582(5) | 4.010(9) |
| 2054(150) | 60.0(7) | 77.20(2) | 4.170(1) | 4.611(2) | 4.015(4) |
| 2061(150) | 67.8(7) | 75.78(5) | 4.128(4) | 4.583(4) | 4.006(9) |
| 2069(150) | 58.4(6) | 77.96(2) | 4.190(2) | 4.624(2) | 4.024(5) |
| 2080(150) | 67.7(7) | 75.79(5) | 4.127(4) | 4.582(4) | 4.008(9) |

Table 2-3 (cont'd)

| 2103(150) | 72.7(8) | 74.52(4) | 4.106(1) | 4.567(1) | 3.974(2) | |
|-----------|---------|----------|----------|----------|----------|--|
| 2139(150) | 64.2(7) | 76.64(3) | 4.151(2) | 4.598(2) | 4.015(5) | |
| 2160(150) | 61.1(7) | 77.18(1) | 4.166(1) | 4.609(1) | 4.019(2) | |

^a Numbers in parentheses are uncertainties on the last digits.

Chapter 3 Reversal of carbonate-silicate cation exchange in cold slabs in Earth's lower mantle

This chapter has been published as Lv et al. (2021).

3.1 Abstract

The stable forms of carbon in Earth's deep interior control storage and fluxes of carbon through the planet over geologic time, impacting the surface climate as well as carrying records of geologic processes in the form of diamond inclusions. However, current estimates of the distribution of carbon in Earth's mantle are uncertain, due in part to limited understanding of the fate of carbonates through subduction, the main mechanism that transports carbon from Earth's surface to its interior. Oxidized carbon carried by subduction has been found to reside in MgCO₃ throughout much of the mantle. Experiments in this study demonstrate that at deep mantle conditions MgCO₃ reacts with silicates to form CaCO₃. In combination with previous work indicating that CaCO₃ is more stable than MgCO₃ under reducing conditions of Earth's lowermost mantle, these observations allow us to predict that the signature of surface carbon reaching Earth's lowermost mantle may include CaCO₃.

3.2 Introduction

Carbon is not only key to life and Earth's habitability, but also traces and modifies geological processes of subduction, partial melting, degassing, and metasomatism, providing valuable insights into Earth's evolution (Hazen & Schiffries, 2013). Over the history of the planet, carbon transport between surface and deep reservoirs has impacted the atmospheric, oceanic and

crustal CO₂ budgets in tandem with the composition and redox state of the Earth's mantle (Kelemen & Manning, 2015; Plank & Manning, 2019). Carbon is transported from Earth's surface to its interior mainly as carbonate minerals in subduction zones, and is returned in carbon-bearing gas/fluid through volcanic degassing (Kelemen & Manning, 2015; Plank & Manning, 2019). These processes leave signatures in the mantle including depletion of incompatible elements (Stachel et al., 2004; Thomson et al., 2016a), diamond formation (and inclusions) (Palyanov et al., 2013; Rohrbach & Schmidt, 2011), and isotopic abundances(Cartigny et al., 2014; Teng, 2017). Carbon flux via subduction to the deep mantle remains uncertain, with estimated magnitudes ranging from 0.0001 to 52 megatons/year (Dasgupta & Hirschmann, 2010; Kelemen & Manning, 2015). The wide range of these estimates is due in part to limited understanding of the physical and chemical responses of carbonates to mantle pressures, temperatures, and compositional environments.

The dominant carbonates carried into the mantle by subducting slabs, dolomite CaMg(CO₃)₂, magnesite MgCO₃, and calcite CaCO₃ (Poli & Schmidt, 2002), undergo changes in crystal structure or state and chemical reactions at depth. Carbonates are likely to be retained as solid minerals in subducting ocean crust until/unless the solidus of carbonated peridotite (Dasgupta & Hirschmann, 2006; Ghosh et al., 2014) or eclogite (Kiseeva et al., 2012; Thomson et al., 2016b) intersects with mantle geotherms, initiating melting. These slab-derived carbonatite melts will segregate to the overlying mantle due to low viscosity and density (Sun & Dasgupta, 2019), or be reduced to diamonds at depths greater than ~250 km via redox freezing (Rohrbach & Schmidt, 2011; Stagno et al., 2013; Thomson et al., 2016b). However, carbonates are present in the mantle transition zone and possibly lower mantle depths in some regions, based on direct evidence provided by carbonate minerals found in deep-sourced diamond inclusions (Brenker et al., 2007; Wirth et al., 2009). Additional evidence from thermodynamic modeling of devolatilization of

carbonate-bearing subducting slab (Kerrick & Connolly, 2001; Poli et al., 2009), and melting experiments on carbonates in the MgCO₃-CaCO₃ system up to 80 GPa (Thomson et al., 2014) supports preservation of solid carbonates along low-temperature geotherms in subducting slabs in the lower mantle. However, temperature is not the only control on the fate of subducted carbonates: carbonates may also interact chemically with the major phases of the ambient mantle or basalt-rich subducted crust. In these compositions in the lower mantle, the silicates potentially reacting with carbonates are bridgmanite (bdg), post-perovskite (pPv), and Ca-perovskite (Ca-Pv).

The presence of the end-member carbonates, MgCO₃ and CaCO₃ (note that (Mg,Ca)(CO₃)₂ dolomite breaks down to these end-members above 5 GPa and 1200 K (Luth, 2004), together with lower mantle silicates depends on the thermodynamics and kinetics of the carbonate-silicate exchange reaction:

$$CaCO_3 + MgSiO_3 \rightarrow MgCO_3 + CaSiO_3$$
 (1)

Previous experiments (Biellmann et al., 1993; Seto et al., 2008) indicate CaCO₃ reacts with silicates to form MgCO₃ via the forward reaction up to 80 GPa and 2300 K, i.e. at least to the midlower mantle. Theoretical studies further predict that MgCO₃ + CaSiO₃ are enthalpically favored over CaCO₃ + MgSiO₃ throughout the lower mantle pressure and temperature regime (Oganov et al., 2008; Pickard & Needs, 2015; Santos et al., 2019; Yao et al., 2018b; Zhang et al., 2018). However, although many studies have addressed the stability of individual carbonates up to higher pressures (Binck et al., 2020; Boulard et al., 2011; Isshiki et al., 2004), no experiments examined the carbonate-silicate cation exchange reaction up to core-mantle boundary conditions.

In this work, to assess the stability of MgCO₃ and CaCO₃ coexisting with lower mantle silicates, we conduct a series of experiments on the carbonate-silicate reaction along the lower mantle geotherm. Thin disks of carbonates and silicates were loaded together in laser-heated

diamond-anvil cells (LHDAC, Table 3-1, see Methods for details). Laser heating at 1600-2800 K and 33-137 GPa was applied for 10-400 mins. Run products were examined by in-situ synchrotron X-ray diffraction (XRD) and ex-situ energy-dispersive X-ray spectroscopy (EDX) analysis with a scanning transmission electron microscope (STEM, see Methods for details).

3.3 Results

3.3.1 Calcium carbonate reaction to form magnesium carbonate

Experiments assessed thermodynamic stability by using as reactants either (Mg,Ca)CO₃ + (Mg,Fe)SiO₃ (reactants for the forward reaction, hereafter referred to CaC-to-MgC) and (Mg,Fe)CO₃ + CaSiO₃ (reactants for the reverse reaction, hereafter referred to MgC-to-CaC). For reaction CaC-to-MgC, the criterion for determining whether the reaction takes place is the presence of newly-synthesized CaSiO₃-perovskite in the run product. For reaction MgC-to-CaC, newly-synthesized MgSiO₃ and CaCO₃ indicate the reaction is favorable. The silicate reaction products are easier to observe through diffraction than carbonates due to higher diffraction intensity.

Experiments with CaC-to-MgC reactants indicate the forward reaction takes place in runs conducted below 83 GPa (runs #1-4), as determined via both EDX and XRD. For example, ex-situ electron microscopic analysis of the sample recovered from 33 GPa and 1650 K (run #1) (Figure 3-1a-c) reveals a ~1-μm-thick layer of CaSiO₃ between the silicate layer and the carbonate layer, coexisting with SiO₂, FeO, MgSiO₃, and MgCO₃. These observations are consistent with in-situ XRD patterns of run products after heating (Figure 3-7, Figure 3-9), which exhibit several new sharp peaks compared to the pattern before heating (Figure 3-7a). The diffraction pattern of run products is consistent with the presence of Ca-Pv, magnesite, bdg, wüstite, stishovite, and

monoclinic dolomite III (previously observed at presure above 36 GPa (Mao et al., 2011a)). Ca-Pv can be observed in the run products of CaC-to-MgC up to 83 GPa (Figure 3-7c, Figure 3-8a-b), in agreement with previous experimental observations (Biellmann et al., 1993; Seto et al., 2008).

At higher pressures from 91 to 137 GPa, however, we observe no evidence of carbonate-silicate exchange reaction in experiments with CaC-to-MgC reactants. Ca-Pv is not identified in the run products (runs #5-7) through either in-situ (Figure 3-7d-e, Figure 3-8c-d, Figure 3-9b) or ex-situ analysis. New, sharp peaks from bdg and pPv can be observed in-situ in XRD patterns (Figure 3-7d-e), indicating the sample was sufficiently heated to transform starting materials to high-pressure silicate structures, but no carbonate-silicate exchange reaction occurs. Two hypotheses can explain these observations: (1) in contrast to theoretical predictions that the reversal of the carbonate-exchange reaction takes place at higher pressures and lower temperatures (Oganov et al., 2008; Pickard & Needs, 2015; Santos et al., 2019; Yao et al., 2018b; Zhang et al., 2018), CaCO₃ + MgSiO₃ become more favorable than MgCO₃ + CaSiO₃ from 91-137 GPa and 2100-2800 K; (2) the reaction CaC-to-MgC is hindered by reaction kinetics, and metastable starting materials are observed.

3.3.2 Magnesium carbonate reaction to form calcium carbonate.

In order to resolve the thermodynamically stable phase assemblage, three separate sets of experiments on the backward reaction (MgC-to-CaC, runs #8-11) were conducted at 35-133 GPa and 1800-2000 K. Elemental mapping of the run products of experiments at 88 GPa (run #10, Figure 3-1d-f) and 133 GPa (run #11, Figure 3-1g-i) indicates that MgSiO₃ layers formed along the carbonate-silicate interface, and newly-formed CaCO₃ can be observed as well. At 35 GPa, neither EDX nor XRD shows MgSiO₃ formed from MgC-to-CaC reactants (run #8, Figure 3-13).

Observations of the reversal of the reaction confirm that MgCO₃ is unstable and reacts with CaSiO₃ producing CaCO₃ and MgSiO₃ at pressures higher than 88 GPa along a lower mantle geotherm.

Our results agree with previous experimental constraints (Figure 3-2) below 80 GPa showing: dolomite is unstable relative to CaCO₃ and MgCO₃ at lower mantle conditions (Biellmann et al., 1993; Dorfman et al., 2018; Luth, 2004; Seto et al., 2008); neither CaO nor MgO are observed in run products, indicating no decomposition of CaCO3 and MgCO3 into oxides plus CO₂ (Oganov et al., 2008; Pickard & Needs, 2015; Santos et al., 2019); MgCO₃ is more favorable in the lower mantle than CaCO₃ up to ~80 GPa due to the CaC-to-MgC reaction (Biellmann et al., 1993; Seto et al., 2008). Since similar previous studies were limited to pressures below 80 GPa, they did not observe the reversal reaction (MgC-to-CaC). Combining our new results with previous results (Biellmann et al., 1993; Seto et al., 2008) and theoretical predictions indicating a positive Clapeyron slope for this reaction (Santos et al., 2019; Yao et al., 2018b; Zhang et al., 2018), we suggest a reaction boundary above 80 GPa with a positive slope (black dashed line in Figure 3-2). We note that the experimental data allow for significant uncertainty in this boundary, but are inconsistent with theoretical predictions (Santos et al., 2019; Yao et al., 2018b; Zhang et al., 2018) (yellow region, Figure 3-2). This discrepancy may have been produced by theoretical approximations at higher temperatures. If density functional perturbation theory and quasi-harmonic approximation have misestimated the volumes of the carbonate phases expected to be stable at ~80 GPa and higher pressures, this could lead to the systematic overestimation of Gibbs free energy of CaCO₃ + MgSiO₃ relative to MgCO₃ + CaSiO₃ at higher temperatures.

3.4 Discussion

The pressure/temperature conditions of the reversal reaction as constrained by these experiments are similar to those of polymorphic phase transitions associated with sp^2 - sp^3 bonding changes in both MgCO₃ and CaCO₃, which suggests these transitions are related to the stabilization of a $CaCO_3 + MgSiO_3$ assemblage. The transition from sp^2 - to sp^3 -bonds in MgCO₃ has been identified at ~ 80 GPa with the stabilization of the C2/m structure (Binck et al., 2020; Boulard et al., 2011; Maeda et al., 2017), and the resulting densification of MgCO₃ supports the forward reaction to MgCO₃ + CaSiO₃. The transition in CaCO₃ from sp^2 - to sp^3 -bonds in the $P2_1/c$ -h structure was experimentally observed at ~105 GPa and 2000 K (Lobanov et al., 2017). Computational studies predicted this boundary at ~70 (Zhang et al., 2018) and ~100 GPa (Santos et al., 2020) at mantle-relevant temperatures (red shaded region in Figure 3-3). While an earlier study that did not include the sp³ CaCO₃-P2₁/c-h structure predicted a crossover in silicatecarbonate exchange reaction at 135 GPa and 0 K (Oganov et al., 2008), a later study that predicted the sp³ CaCO₃-P2₁/c-h structure found a silicate-carbonate reaction reversal at 84 GPa and 0 K (Santos et al., 2019). This would correspond to sp^2 - sp^3 crossover and stabilization of CaCO₃ + MgSiO₃ in the mid-lower mantle.

Whether a crossover in the carbonate-silicate exchange reaction takes place in the deep Earth depends on whether carbonates are preserved in Earth's lower mantle to at least 1800 km depth. Previous studies have identified barriers to carbon subduction and stability in the lower mantle, particularly melting (Kiseeva et al., 2013; Thomson et al., 2016b) and reduction (Drewitt et al., 2019; Kakizawa et al., 2015; Li et al., 2018). If carried in cold subducting slabs, MgCO₃ and CaCO₃ may avoid melting as their melting temperatures (Thomson et al., 2014) are higher than some predicted cold slab geotherms (Maeda et al., 2017). Any solid carbonate in the mantle will

be in contact and may equilibrate with silicates in all mantle environments and with free silica in basalt-rich compositions. MgCO₃ and CaCO₃ have been observed in experiments (Drewitt et al., 2019; Kakizawa et al., 2015; Li et al., 2018) to undergo decarbonation reactions with free silica over a pressure range of ~40 to 60 GPa. However, the Clapeyron slope of $CaCO_3 + SiO_2 \rightarrow CaSiO_3$ + CO₂ is positive and takes place at pressure/temperature conditions warmer than the coolest slab geotherms (Li et al., 2018). Observations that MgCO₃ is less thermally stable than CaCO₃ support the survival of CaCO₃ rather than MgCO₃ along a cold subducted slab geotherm to the lowermost mantle (Drewitt et al., 2019; Maeda et al., 2017) (Figure 3-3). In this study, we report a reversal in the Mg-Ca silicate-carbonate cation exchange reaction at ~90 GPa, making MgCO₃ + CaSiO₃ favorable in the upper part of the lower mantle, while CaCO₃ + MgSiO₃ is preferred in the lower part of the lower mantle (Figure 3-3). However, the question of whether any carbonate persists to these depths in the coldest subducting slabs remains unresolved. If MgCO₃ remains present in cold slabs, and the reaction CaC-to-MgC proceeds throughout most of the mantle eliminating CaCO₃, the reversal MgC-to-CaC reaction may transform MgCO₃ back to CaCO₃ in the lowermost mantle (Figure 3-4). CaCO₃ could thus be found in the lowermost mantle coexisting with silicates and reduced iron.

The reduced nature of the Earth's mantle, with oxygen fugacity inferred to be near the iron-wüstite buffer in the transition zone and greater depths (Frost & McCammon, 2008), stabilizes diamond or Fe-carbide as long-term hosts of carbon, owing to their chemical refractoriness and dynamic immobility (Shirey et al., 2013). Similarly, our experimental observations support CaCO₃ as a refractory, stable host for oxidized carbon in the middle to lowermost mantle, in particular, the high-pressure polymorph of CaCO₃ (CaCO₃-P2₁/c-h) with tetrahedral bonds (Lobanov et al., 2017). Experimental observations also suggest CaCO₃ is more resistant to redox breakdown

reaction with iron under reduced conditions than MgCO₃ (Dorfman et al., 2018). In addition, due to the cation exchange between carbonate and silicate, the relative stability of MgCO₃ or CaCO₃ will change in the lowermost mantle, and depending on conditions one of these phases may buffer the redox state of the mantle through an influx of oxidized carbon in the form of solid carbonate (Stagno et al., 2019).

The Mg-Ca silicate-carbonate exchange reactions along subduction pressure-temperature (P-T) conditions may impact observable signatures of Mg and Ca isotopes in mantle silicates under certain special conditions, or in carbonate inclusions in diamonds. Subducting carbonates carry low- $\delta^{44/40}$ Ca and low- δ^{26} Mg signatures relative to the heavier mantle ratios, but although previous studies have observed heterogeneity in the Ca and Mg isotope signatures in basalts and mantle peridotites, these studies determined that lighter ratios cannot be simply interpreted as evidence of recycled marine carbonates (Ionov et al., 2019; Wang et al., 2014). The Mg-Ca silicate-carbonate exchange reactions along subduction P-T conditions may contribute to these variable Mg and Ca isotopic compositions. The reaction CaC-to-MgC in the transition zone and upper part of the lower mantle would transfer light Ca isotopes from subducted CaCO₃ to CaSiO₃ (Ca-Pv) (Figure 3-16). Isotopically light Ca-Pv can then be trapped in diamond inclusions and return to the surface (Nestola et al., 2018), while the Ca isotopic signature of upwelling rocks would remain variable, as it undergoes continuous fractionation within peridotitic mantle lithologies (Amsellem et al., 2020; Chen et al., 2018b; Ionov et al., 2019; Kang et al., 2017). The modification of carbonatesilicate phase equilibria observed in this study provides a new process that could alter Mg and Ca isotopic composition in such lithologies (Figure 3-16). While the isotope signature of MgSiO₃ produced by reaction MgC-to-CaC would not be observable due to the small masses involved relative to the vast lower mantle reservoir of MgSiO₃, any CaCO₃ produced in the deep lower

mantle by this reaction would carry a heavier deep mantle $\delta^{44/40}$ Ca signature that would distinguish it from surface-derived carbonate. If preserved in diamond inclusions and returned to the surface, heavy CaCO₃ could be used to trace the presence of oxidized carbon in the lowermost mantle. The potential of CaCO₃ to be a signature of an ultradeep carbon cycle reaching the core-mantle-boundary region may help to reveal other mysteries of the deep mantle, such as heat budget related to radioactive elements stored in Ca-bearing silicates (Corgne et al., 2005), and compositions of heterogeneities that may record Earth's early history (Howell et al., 2020; Nestola et al., 2018).

3.5 Methods

3.5.1 Starting materials

To investigate phase equilibria in the carbonate-silicate system in Earth's lower mantle and control for effects of reaction kinetics, both CaC-to-MgC and MgC-to-CaC experiments were carried out in symmetric diamond anvil cells (DAC) with flat-top double-sided laser heating (Prakapenka et al., 2008). For CaC-to-MgC, natural dolomite with homogeneous composition of (Mg_{0.38}Ca_{0.59}Fe_{0.03})CO₃ was used as a carbonate reactant, the composition and structure of which has been characterized by X-ray fluorescence spectroscopy and X-ray diffraction, respectively (Dorfman et al., 2018). Fe-bearing enstatite synthesized at École Polytechnique Fédérale de Lausanne with a composition of (Mg_{0.5}Fe_{0.5})SiO₃ was used as a silicate reactant (Dorfman et al., 2020). For MgC-to-CaC, natural ferromagnesite (sample from Princeton University) was used as a carbonate reactant, with composition determined to be (Mg_{0.87}Fe_{0.13})CO₃ by wavelength dispersive X-ray spectroscopy in a Cameca SX100 Electron Probe Microanalyzer at University of Michigan. Pure calcium silicate (CaSiO₃, Alfa Aesar) was used as a silicate reactant. The chief advantages to the abovementioned starting compositions are that recognition of a carbonate-silicate exchange

reaction only requires identification of the presence of newly synthesized silicates in quenched run products, i.e., Ca-perovskite (Ca-Pv) in CaC-to-MgC and bridgmanite (bdg) in MgC-to-CaC; and Fe-bearing enstatite and ferromagnesite can serve as laser absorber during the forward CaC-to-MgC and reversal MgC-to-CaC experiments, respectively.

3.5.2 LHDAC experiments

The dolomite, enstatite, and calcium silicate samples were separately ground under acetone in an agate mortar for ~2 hours each to achieve homogenous, finely powdered samples with grain size typically less than ~2 μm. A single ferromagnesite crystal was double-side polished to ~10micron thickness. All starting materials were dried in an oven at 120 °C overnight before loading, and the powder samples were subsequently pressed in a DAC to form thin foils approximately ~8-10 µm thick. The enstatite foils and ferromagnesite crystals were sandwiched between iron-free dolomite and calcium silicate, respectively, serving as thermal insulators in symmetric DACs for CaC-to-MgC and MgC-to-CaC (Figure 3-5 and Figure 3-6). No other pressure standard or medium was loaded to prevent reactions with other components and contamination of the chemical system. The sample sandwiches were loaded in sample chambers with diameters approximately halves of the anvil culet sizes drilled into Re gaskets pre-indented to a thickness of ~30μm, by using the laser drilling system at HPCAT (Sector 16) of the Advanced Photon Source (APS), Argonne National Laboratory (ANL) (Hrubiak et al., 2015). Diamond anvils with flat culets of 300 µm were used for experiments under 60 GPa, beveled culets of 150/300 µm for experiments under 100 GPa, and beveled culets of 75/300 µm for experiments up to 140 GPa.

Before laser heating, each sample was compressed to the target pressure at 300 K, and after heating each sample was quenched to ambient pressure at 300 K to limit and preserve reactions at

target conditions. Pressures were determined from the Raman shift of the singlet peak of the diamond anvil at the culet surface (Akahama & Kawamura, 2006), and post-heating pressures were typically within 3% of the pre-heating pressure. Thermal pressure during heating may be estimated to be ~10% GPa higher than the pre-heating pressure at the modest temperatures (Figuet et al., 2010; Nomura et al., 2014). High-temperature conditions were achieved by using a double-sided ytterbium fiber laser heating system at beamline 13-ID-D (GeoSoilEnviroCars) of APS, ANL (Prakapenka et al., 2008), with two 1.064 µm laser beams focused down to a flat-top spot with a diameter of 10-12 µm on both sides of the sample. Temperatures of the heated samples were determined by fitting the measured thermal radiation spectra using the Planck radiation function under the graybody approximation (Prakapenka et al., 2008). The temperature reported in Table 3-1 is the temporal average of multiple temperature measurements over the heating duration. Temperature fluctuations over this time scale were less than the specified uncertainty, which is derived from a standard deviation of temperature measurements from both sides of the laser-heated sample (typically ± 100 K below 2000 K and ± 150 K above 2000 K) (Figure 3-14 and Figure 3-15). Experiments were held at temperatures between 1600 and 2800 K for ~30 min in CaC-to-MgC experiments and up to 400 min in MgC-to-CaC experiments.

3.5.3 In-situ XRD

Phases synthesized at high P/T and achievement of chemical steady-state were determined by in-situ angle-dispersive X-ray diffraction (XRD) measurements performed before, during and after heating at beamline 13-ID-D (GeoSoilEnviroCars) of APS, ANL. The incident X-ray beam was focused down to less than $3\times4~\mu\text{m}^2$ with a monochromatic wavelength λ =0.3344 Å. Diffracted X-rays were recorded using a MAR 165 detector or Pilatus 1M CdTe pixel array detector. NIST

standard LaB₆ was used to calibrate the detector distance, tilt angle, and rotation angle of the image plane relative to the incident X-ray beam. Exposure times were typically 30 s. The XRD patterns were integrated to produce 2θ plots using the software DIOPTAS (Prescher & Prakapenka, 2015).

3.5.4 Ex-situ EDX

After complete pressure release, each sample was recovered from the LHDAC, and then sectioned along the compression axis through the laser-heated spot and over the entire thickness of the DAC sample (~5-20 μm), using a focused ion beam (FIB) coupled with a field emission scanning electron microscope (FE-SEM) at IPGP (Paris, France) or the Michigan Center for Materials Characterization at the University of Michigan (Ann Arbor, USA). A ~30-nm-thick Au layer was coated on each sample to reduce charging in the scanning electron microscope, and a 2-μm-thick Pt layer was deposited across the center of each heated spot to protect the sample from damage by the Ga⁺ ion beam. Thin sections of each heated spot were extracted and polished to electron transparency (~100 nm thickness).

Textural and chemical characterization of recovered samples was performed with scanning transmission electron microscopy (STEM) and energy-dispersive X-ray spectroscopy (EDX) in a JEOL 2200FS field emission TEM (Center for Advanced Microscopy, MSU), operated at 200 kV to image the sample in Bright-Field. EDX maps were scanned over 512 ×384 pixel areas with a pixel dwell time of 50 microseconds. Typical count rates were ~2,000 counts per second. Chemical mapping rather than point measurement approach prevents migration of elements due to damage by the electron beam. Uncertainties in compositions were determined from standard deviations of EDX measurements obtained from selected regions within multiple grains.

3.6 Supporting Information

To assess whether observations of Ca and Mg isotopes in mantle silicates or diamond inclusions can be used to detect the presence of carbonates in the deep mantle, we estimate the potential effects of carbonate-silicate cation exchange on isotope signatures based on available constraints and mass balance.

Subducting carbonates carry low- $\delta^{44/40}$ Ca (reported relative to NIST SRM 915a standard, $\delta^{44/40}$ Ca = [(\frac{44}{Ca}/\frac{40}{Ca})_{sample}/(\frac{44}{Ca}/\frac{40}{Ca})_{standard} - 1] \times 1,000) and low-\delta^{26}Mg (relative to the Dead Sea metal Mg standard (DSM-3, Galy et al., 2003), δ^{26} Mg = $[(^{26}\text{Mg}/^{24}\text{Mg})_{\text{sample}}/(^{26}\text{Mg}/^{24}\text{Mg})_{\text{standard}}]$ 1]×1,000) signatures, while reported mantle ratios are heavier (Fantle & Tipper, 2014; Kang et al., 2017; Teng et al., 2010; Wombacher et al., 2011)(Table 3-2). Based on both our observations and previous experimental studies (Biellmann et al., 1993; Seto et al., 2008), CaCO₃ is unstable relative to MgCO₃ in the shallow lower mantle due to the reaction CaC-to-MgC, so the light Ca isotopes brought by CaCO₃ may be transferred to CaSiO₃ in the slab and surrounding ambient shallow lower mantle. Conversely, our experiments obtain the new result that in the deep lower mantle, MgCO₃ is unstable relative to CaCO₃ due to the reaction MgC-to-CaC, so the light Mg isotopes brought by MgCO₃ may be transferred to the surrounding ambient deep lower mantle in MgSiO₃, and deep mantle CaCO₃ would form with the Ca isotope signature of the mantle silicate. These reactions, their stable isotope equilibrium fractionation factors, and the masses of carbonate and silicate that reach equilibrium may moderate isotope ratios in cold carbonated subducting slabs and their surroundings.

The reaction CaC-to-MgC affects $\delta^{44/40}$ Ca of mantle and δ^{26} Mg of carbonate:

$$(f_{\text{Ca_pyro}} + k \cdot f_{\text{Ca_carb}}) \cdot \delta^{44/40} \text{Ca}_{\text{pyro}} = f_{\text{Ca_pyro}} \cdot \delta^{44/40} \text{Ca}_{\text{pyro}}^{i} + k \cdot f_{\text{Ca_carb}} \cdot \delta^{44/40} \text{Ca}_{\text{carb}}^{i}$$
(1)

$$(f_{\text{Mg_carb}} + k \cdot f_{\text{Ca_carb}}) \cdot \delta^{26} \text{Mg}_{\text{carb}} = f_{\text{Mg_carb}} \cdot \delta^{26} \text{Mg}_{\text{carb}}^{i} + k \cdot f_{\text{Ca_carb}} \cdot \delta^{26} \text{Mg}_{\text{pyro}}^{i}$$
(2)

and the reaction MgC-to-CaC affects δ^{26} Mg of mantle and $\delta^{44/40}$ Ca of carbonate:

$$(f_{\text{Mg_pyro}} + k \cdot f_{\text{Mg_carb}}) \cdot \delta^{26} \text{Mg}_{\text{pyro}} = f_{\text{Mg_pyro}} \cdot \delta^{26} \text{Mg}_{\text{pyro}}^{i} + k \cdot f_{\text{Mg_carb}} \cdot \delta^{26} \text{Mg}_{\text{carb}}^{i}$$
(3)

$$(f_{\text{Ca_carb}} + k \cdot f_{\text{Mg_carb}}) \cdot \delta^{44/40} \text{Ca}_{\text{carb}} = f_{\text{Ca_carb}} \cdot \delta^{44/40} \text{Ca}_{\text{carb}}^{i} + k \cdot f_{\text{Mg_carb}} \cdot \delta^{44/40} \text{Ca}_{\text{pyro}}^{i}$$
(4)

where $f_{\text{Ca_pyro}}$, $f_{\text{Ca_carb}}$, $f_{\text{Mg_pyro}}$, $f_{\text{Mg_carb}}$ represent the mole fraction of Ca and Mg contributed by pyrolitic mantle and carbonate, respectively. i represents the initial status before the reaction. k is reaction rate ranging from 0 to 1, representing the mole fraction of carbonate that undergoes cation exchange reaction with silicate in pyrolitic mantle. In this model, we fixed the weight ratio of carbonate and surrounding pyrolitic mantle to 1/10 based on previous work applied to upper mantle conditions (Wang et al., 2014). For a subducting slab in the lower mantle, this ratio represents a generous upper bound on the amount of carbonate available to react with silicates. We varied the composition of subducted carbonate by changing the n in (Mg_nCa_{n-1})CO₃ from 0 to 1. Parameters used in the calculation are listed in Table 1, and the calculated results are plotted in Figure 3-16.

We assume equilibrium isotope fractionation between carbonates and mantle silicates, occurring after the cation exchange reaction, i.e., carbonates are well mixed and equilibrium with surrounding mantle. In this case, $\delta^{44/40}$ Ca and δ^{26} Mg of this carbonated pyrolite are governed by the following equations according to Wang et al. (2014), respectively:

$$(f_{\text{Ca_pyro}} + k \cdot f_{\text{Ca_carb}}) \, \delta^{44/40} \text{Ca}_{\text{pyro}}^{\text{f}} = (f_{\text{Ca_pyro}} + k \cdot f_{\text{Ca_carb}}) \cdot \delta^{44/40} \text{Ca}_{\text{pyro}} +$$

$$(\delta^{44/40} \text{Ca}_{\text{carb}}^{\text{i}} + \Delta^{44/40} \text{Ca}_{\text{pyro-carb}}) \cdot (f_{\text{Ca_carb}} - k \cdot f_{\text{Ca_carb}})$$

$$(5)$$

$$(f_{\text{Mg_pyro}} + k \cdot f_{\text{Mg_carb}}) \cdot \delta^{26} \text{Mg}_{\text{pyro}}^{\text{f}} = (f_{\text{Mg_pyro}} - k \cdot f_{\text{Ca_carb}}) \cdot \delta^{26} \text{Mg}_{\text{pyro}}^{\text{i}} + (\delta^{26} \text{Mg}_{\text{carb}} + \Delta^{26} \text{Mg}_{\text{pyro-carb}}) \cdot (f_{\text{Mg_carb}} + k \cdot f_{\text{Ca_carb}})$$

$$(6)$$

similarly, after the reaction MgC-to-CaC, $\delta^{44/40}$ Ca and δ^{26} Mg of mantle are governed by the following equations, respectively:

$$(f_{\text{Mg_pyro}} + k \cdot f_{\text{Mg_carb}}) \cdot \delta^{26} \text{Mg}_{\text{pyro}}^{\text{ f}} = (f_{\text{Mg_pyro}} + k \cdot f_{\text{Mg_carb}}) \cdot \delta^{26} \text{Mg}_{\text{pyro}} + k \cdot f_{\text{Mg_carb}}$$

$$(\delta^{26} Mg_{carb}^{i} + \Delta^{26} Mg_{pyro-carb}) \cdot (f_{Mg_carb} - k \cdot f_{Mg_carb})$$

$$(f_{Ca_pyro} + k \cdot f_{Ca_carb}) \cdot \delta^{44/40} Ca_{pyro}^{f} = (f_{Ca_pyro} - k \cdot f_{Mg_carb}) \cdot \delta^{44/40} Ca_{pyro}^{i} +$$

$$(\delta^{44/40} Ca_{carb} + \Delta^{44/40} Ca_{pyro-carb}) \cdot (f_{Ca_carb} + k \cdot f_{Mg_carb})$$

$$(8)$$

where f represents the final status after the isotope fractionation. $\Delta^{44/40}$ Ca_{pyro-carb} and Δ^{26} Mg _{pyro-carb} represent equilibrium isotope fractionation between silicate and carbonate. Values for $\Delta^{44/40}$ Ca_{pyro-} $_{carb}$ and $\Delta^{26}Mg$ $_{pyro-carb}$ listed in Table 3-2 represent constraints measured at ~Earth surface conditions. Fractionation may be expected to depend on pressure and temperature as well as the high-pressure polymorphism in the carbonate and silicate systems. However, due to the lack of available measurements at deep mantle conditions, we assume fractionation values remain constant throughout the mantle. The calculated results are plotted in Figure 3-17.

(8)

To use isotope fractionation to identify carbonates at depth, isotope ratios in subducted carbonate cation exchange scenarios must be significantly different from the scenario where no subducted carbonate reaches the deep mantle. If no carbonate reaches the lower mantle in subducted slabs, lower-mantle-derived silicates will have heavy $\delta^{44/40}$ Ca and δ^{26} Mg, and there would be no lower-mantle-derived carbonate. If some carbonate reaches the shallow lower mantle in subducted slabs, lower-mantle-derived silicates from this region may have light $\delta^{44/40}$ Ca due to reaction of persistent metastable CaCO₃ with MgSiO₃ to produce CaSiO₃ (reaction CaC-MgC). The mass balance calculation indicates that a generous upper bound on the masses involved could locally enrich mantle CaSiO₃ in light $\delta^{44/40}$ Ca (Figure 3-16). There would be no effect on δ^{26} Mg of the silicates in the mantle, the CaC-MgC reaction would make δ^{26} Mg in the carbonate relatively heavy (Figure 3-16a) and would no longer appear to have a subduction source. If some carbonate continues to the deeper lower mantle where the reaction MgC-CaC becomes favorable, the much greater abundance of Mg in mantle silicates means that δ^{26} Mg of silicates would not be significantly impacted by the breakdown of MgCO₃ (Figure 3-16b). However, the $\delta^{44/40}$ Ca in CaCO₃ produced by this reaction would reflect the heavy mantle source (Figure 3-16b) and could be distinguished by CaCO₃ with a surface origin. The exchange reactions potentially overwrite the isotope signals in subducted carbonates with heavy isotopes, and could not significantly affect mantle silicate isotope ratios in the deep lower mantle. Mg and Ca isotope composition of carbonated pyrolite after the equilibrium isotopic fractionation between carbonate and surrounding pyrolitic mantle depends on the mole ratio of Mg and Ca of the subducted carbonates, but less strongly depends relies on the reaction completion (Figure 3-17). In summary, carbonate-silicate cation exchange reactions only produce potentially observable heterogeneity in silicate cation isotopes relative to the null case in the CaC-MgC regime, and only in $\delta^{44/40}$ Ca.

CaCO₃ formed by a cation exchange reaction between MgCO₃ and CaSiO₃ in the lower mantle can be expected to have a different isotope signature relative to subducted CaCO₃ formed at Earth's surface. CaCO₃ formed in the deep lower mantle would contain Ca isotopes that sample the "ambient mantle" source rather than a subducted carbonate source. This could provide a test for shallow vs. ultradeep origin of carbonate inclusions. This is the motivation for future systematic study of the isotope signatures of diamond inclusions.

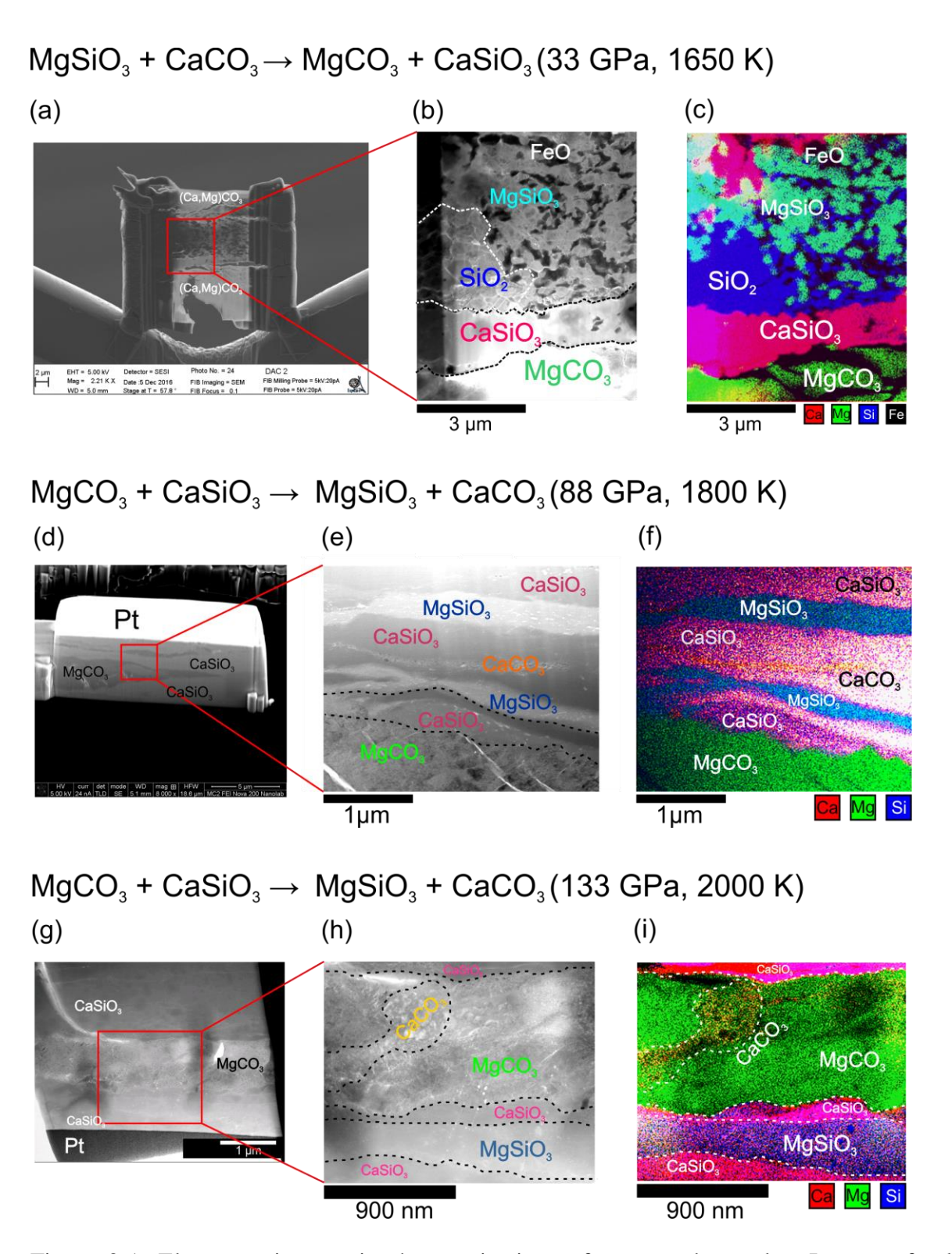


Figure 3-1: Electron microscopic characterizations of recovered samples. Images of selected recovered sample cross-sections obtained using backscattered scanning electron microscopy (a, d, g), scanning transmitted electron microscopy (b, e, h) and energy-dispersive X-ray mapping (c, f,

i) of the cross-section show the silicate layer sandwiched by two carbonate layers, with the reaction region along the contacting interface. (a-c) Ex-situ analysis of sample quenched from 33 GPa and 1650 K heated for 15 min (run #1) demonstrates reaction CaC-to-MgC: CaSiO₃ is not present in starting materials but is indicated in EDX map by colocation of Ca and Si, shown in magenta; (d-f) Ex-situ analysis of sample quenched from 88 GPa and 1800 K heated for 150 min (run #9) demonstrates reaction MgC-to-CaC: MgSiO₃ is not present in starting materials but is indicated in EDX map by colocation of Mg and Si, shown in blue-green. CaCO₃ also appears as red (Ca, but no Si) ribbon within CaSiO₃ starting material. (g-i) Ex-situ analysis of sample quenched from 133 GPa and 2000 K heated for 400 min (run #10) demonstrates reaction MgC-to-CaC: MgSiO₃ appears as Ca-depleted, Si-rich region (blue or blue-green) adjacent to CaSiO₃ starting material (magenta).

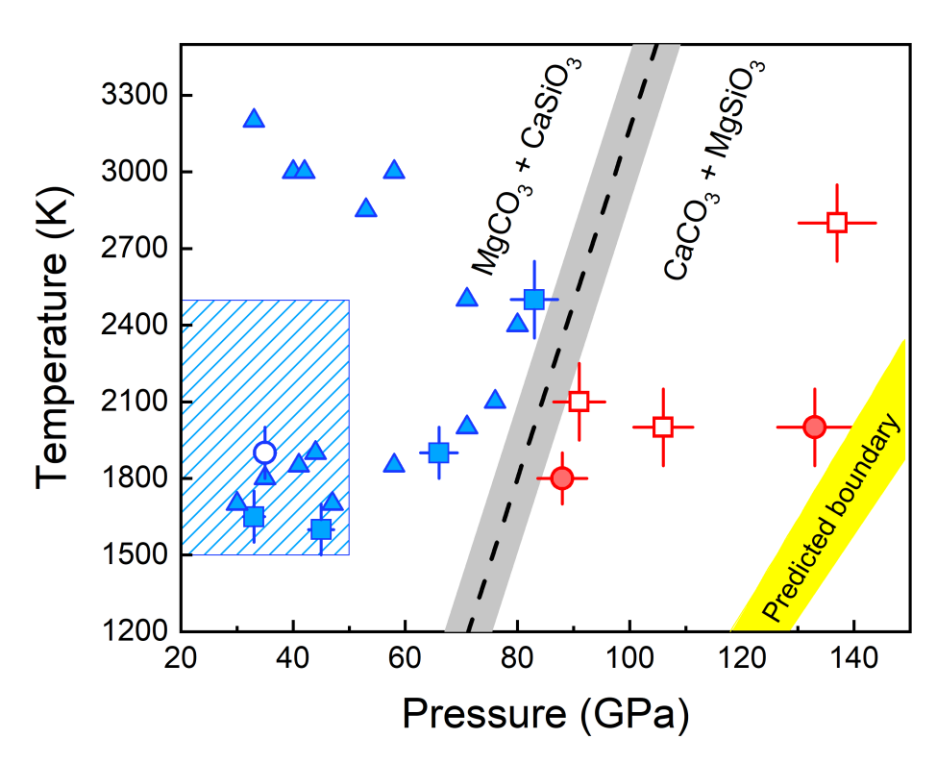


Figure 3-2: Phase diagram for relative stability of the MgCO₃ + CaSiO₃ assemblage versus CaCO₃ + MgSiO₃. The boundary sketched as a black dashed line with gray shadow as uncertainty inferred is based on experimental observations of carbonate-silicate exchange reactions CaC-to-MgC and MgC-to-CaC. Squares represent observations from this work starting with (Ca,Mg)CO₃ and (Mg,Fe)SiO₃, looking for newly-synthesized CaSiO₃ to indicate the CaC-to-MgC reaction takes place. Circle symbols represent observations from this work of experiments starting with (Mg,Fe)CO₃ + CaSiO₃, looking for identification of newly-synthesized MgSiO₃ to indicate the MgC-to-CaC reaction takes place. Open symbols indicate nonreaction and filled for confirmed reaction, and blue and red colors correspond to the inferred stable phase assemblage based on reaction products. Triangles indicate the *P-T* conditions for CaC-to-MgC taking place reported by Seto et al. (2008), and blue shaded region indicates approximate conditions of four experiments conducted by Biellmann et al. (1993) using indirect methods for pressure and temperature calibration, which all produced the run products MgCO₃ + CaSiO₃. The error bars indicate uncertainties of pressure and temperature measurements (see Methods for details). The boundaries

proposed by previous theoretical predictions are illustrated by yellow shaded region (Santos et al., 2019; Yao et al., 2018b; Zhang et al., 2018).

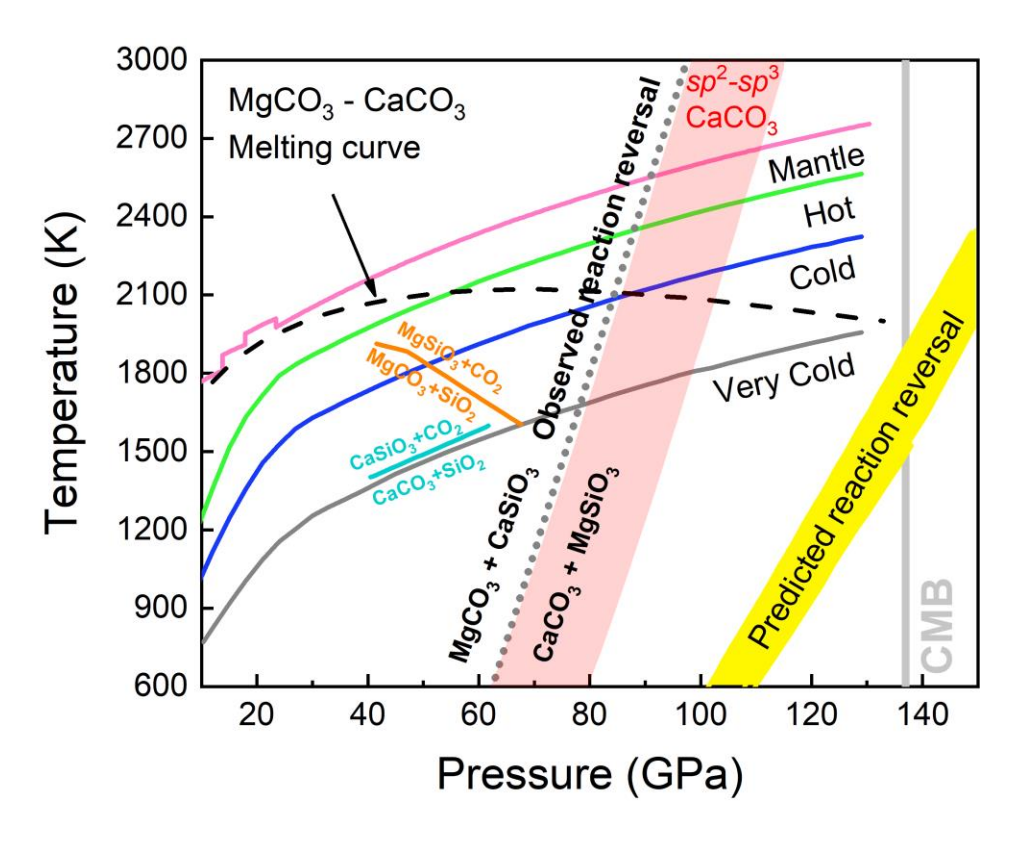


Figure 3-3: Pressure-temperature diagram of reactions between carbonate, silicates, and silica in the subducted oceanic crust to the lower mantle. The grey dotted line indicates the reversal boundary of the carbonate-silicate exchange reaction proposed by this study, whereas previous theoretical predictions are illustrated by yellow shaded region (Santos et al., 2019; Yao et al., 2018b; Zhang et al., 2018). The cyan and orange lines indicate the decarbonation reactions of $CaCO_3 + SiO_2$ (Li et al., 2018) and $MgCO_3 + SiO_2$ (Drewitt et al., 2019), respectively. The black dashed line shows the melting curve of $MgCO_3$ - $CaCO_3$ system constrained by Thomson et al. (Thomson et al., 2014). Four typical mantle geotherms are modified from Maeda et al. (Maeda et al., 2017). The red shaded region indicates the transition boundary of $CaCO_3$ from sp^2 - to sp^3 structure predicted by density functional theory computations (Santos et al., 2020; Zhang et al., 2018).

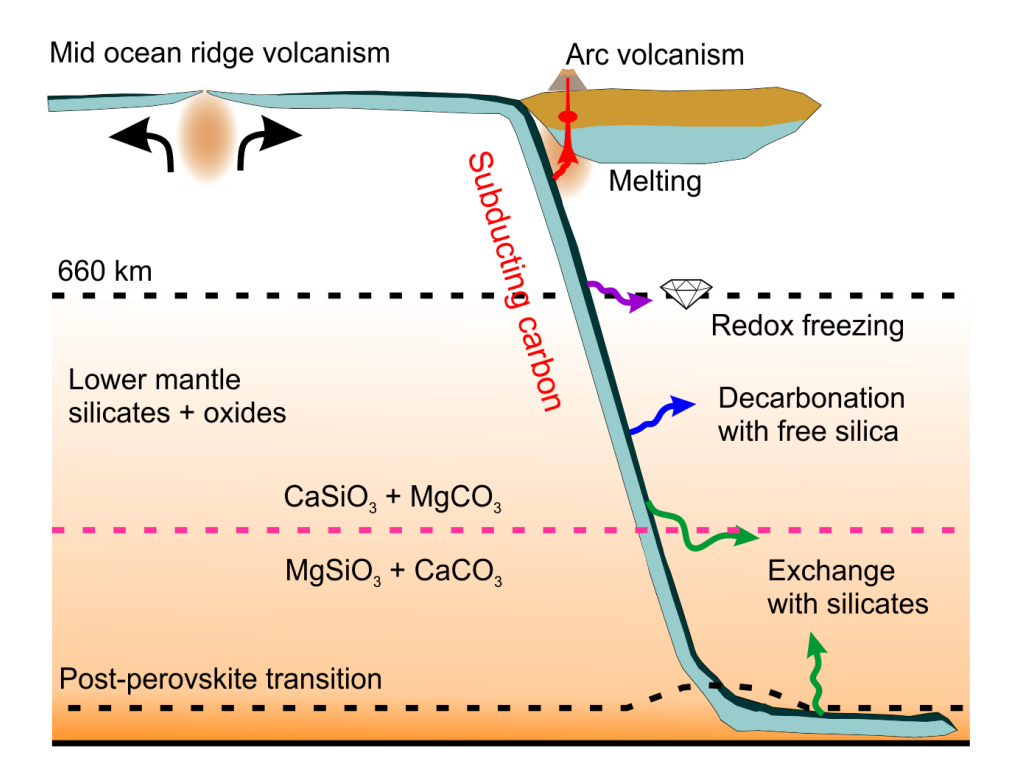


Figure 3-4: Schematic illustration of the fate of carbonates in the oceanic crust (dark blue) subducted to the lower mantle. Through subduction, the carbonates may undergo melting (red arrow), redox freezing with metallic iron (purple arrow), decarbonation reaction with free silica (blue arrow), and exchange reaction with lower mantle silicates (green arrow). Based on the observation of reversal of the carbonate-silicate cation exchange reaction at conditions relevant to cold subducted slabs at mid-lower-mantle depths, CaCO₃ is the potential stable phase that hosts oxidized carbon in the lowermost mantle.

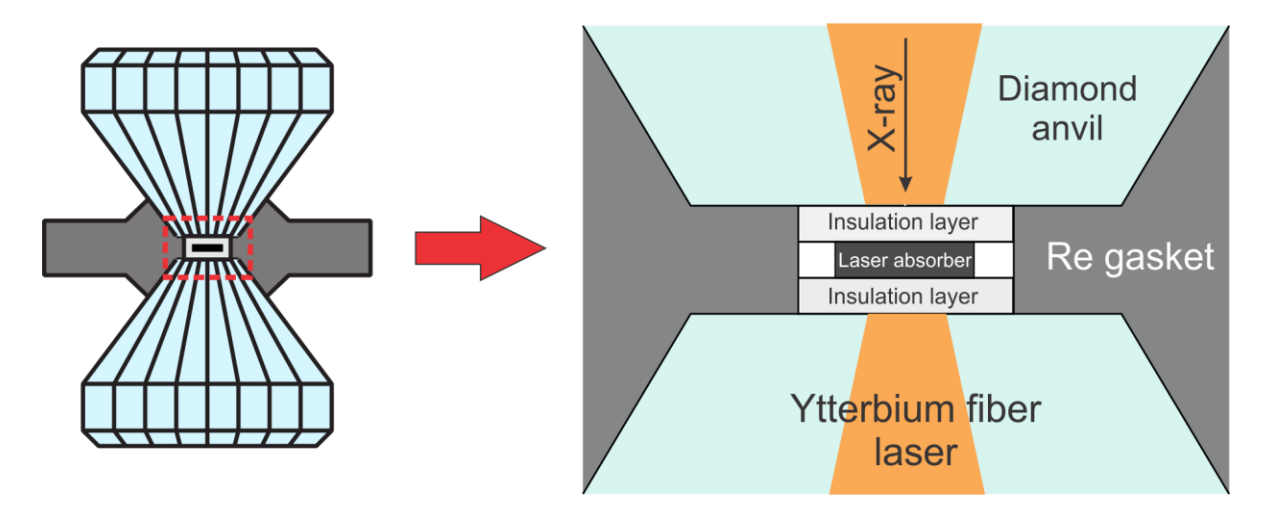


Figure 3-5: Schematic diagram of the laser-heated diamond-anvil cell (LHDAC) and sample loading design. The insulation layer (light gray region) and the laser absorber (black region) for different experimental runs are summarized in Table 3-1.

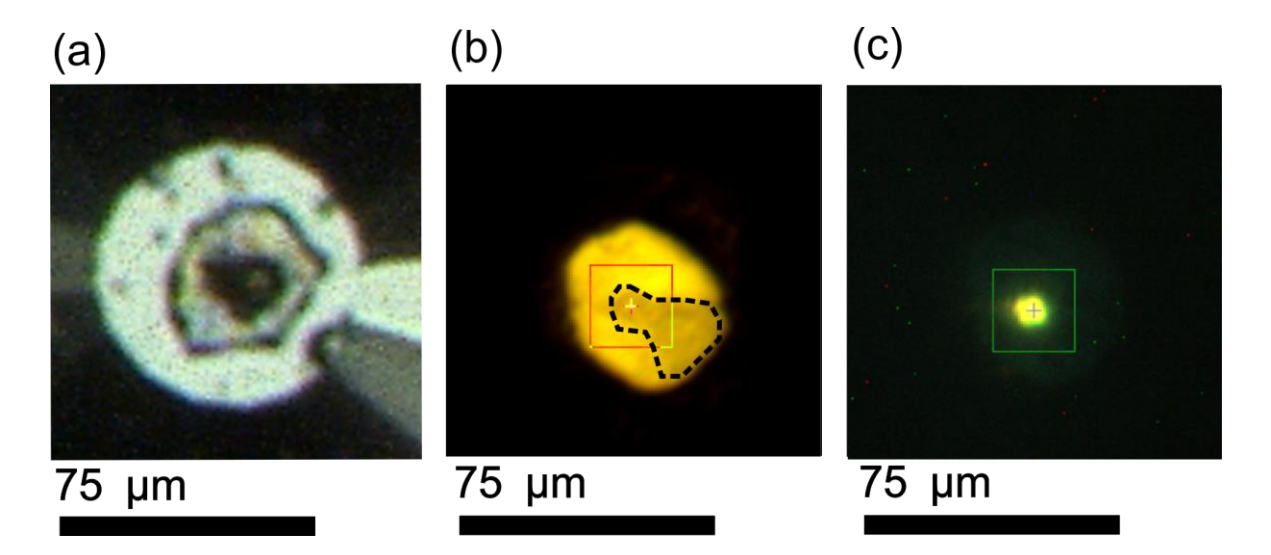


Figure 3-6: Microscope images of loaded sample for run #9. We loaded the Fe-bearing sample on top of the thermal insulation layer on the piston side of DAC (75/300 beveled anvil), then we loaded another insulation layer on the cylinder side of DAC together with Re gasket before we close and compress the DAC to the target pressure. (a) Samples are loaded at ambient conditions on the piston side before closing the cell. (b) Samples are compressed to target pressure before heating, and the dashed circle indicates the dark Fe-bearing sample. (c) The heating spot on the loaded sample during laser heating.

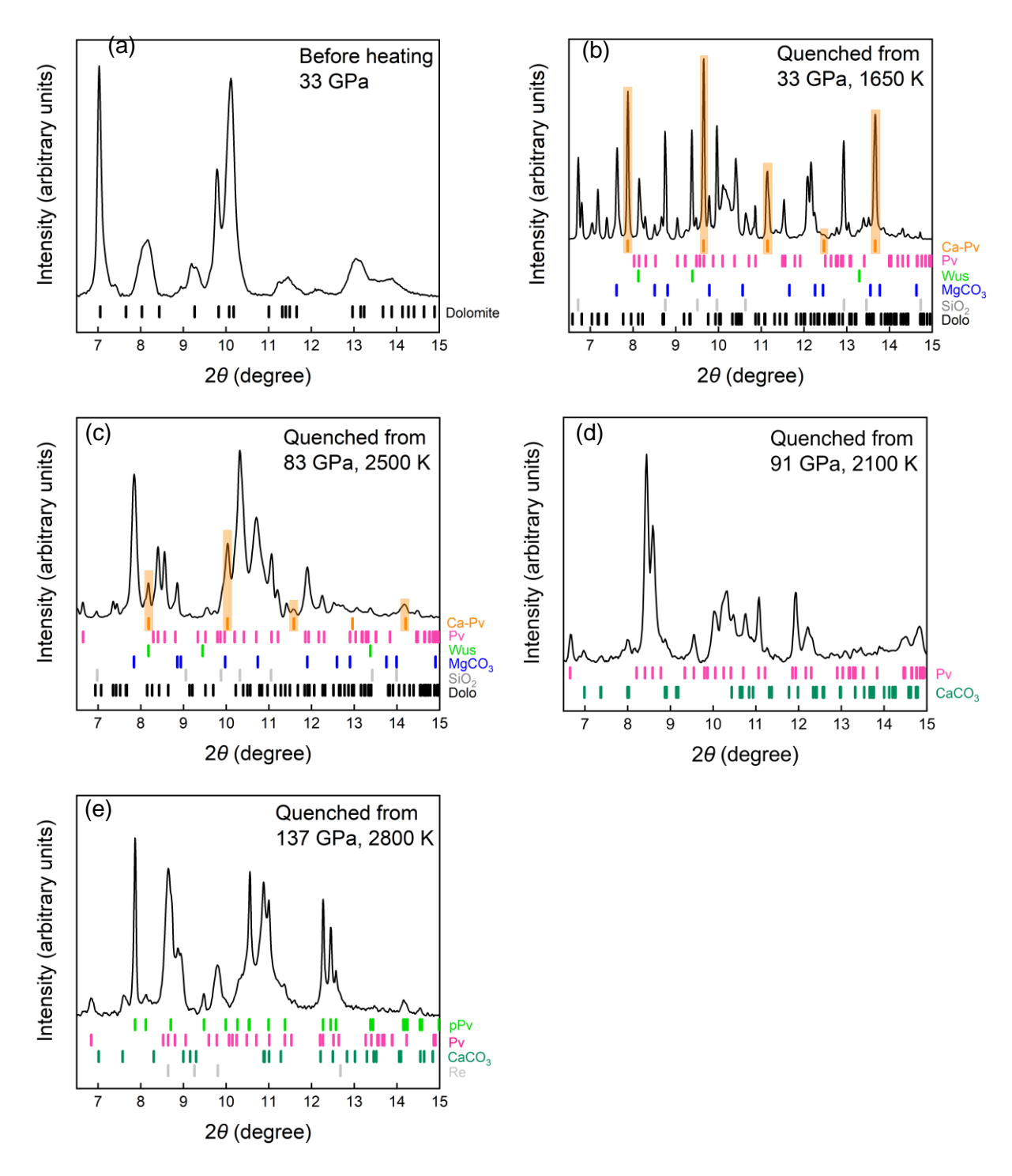


Figure 3-7: X-ray diffraction patterns obtained from the starting material of CaC-to-MgC before heating (a) and products quenched from various *P-T* conditions: (b) run #1, (c) run #4, (d) run #5, and (e) run #7, and phase identifications are indicated by small ticks at the bottom. The wavelength of the incident X-ray beam was 0.3344 Å.

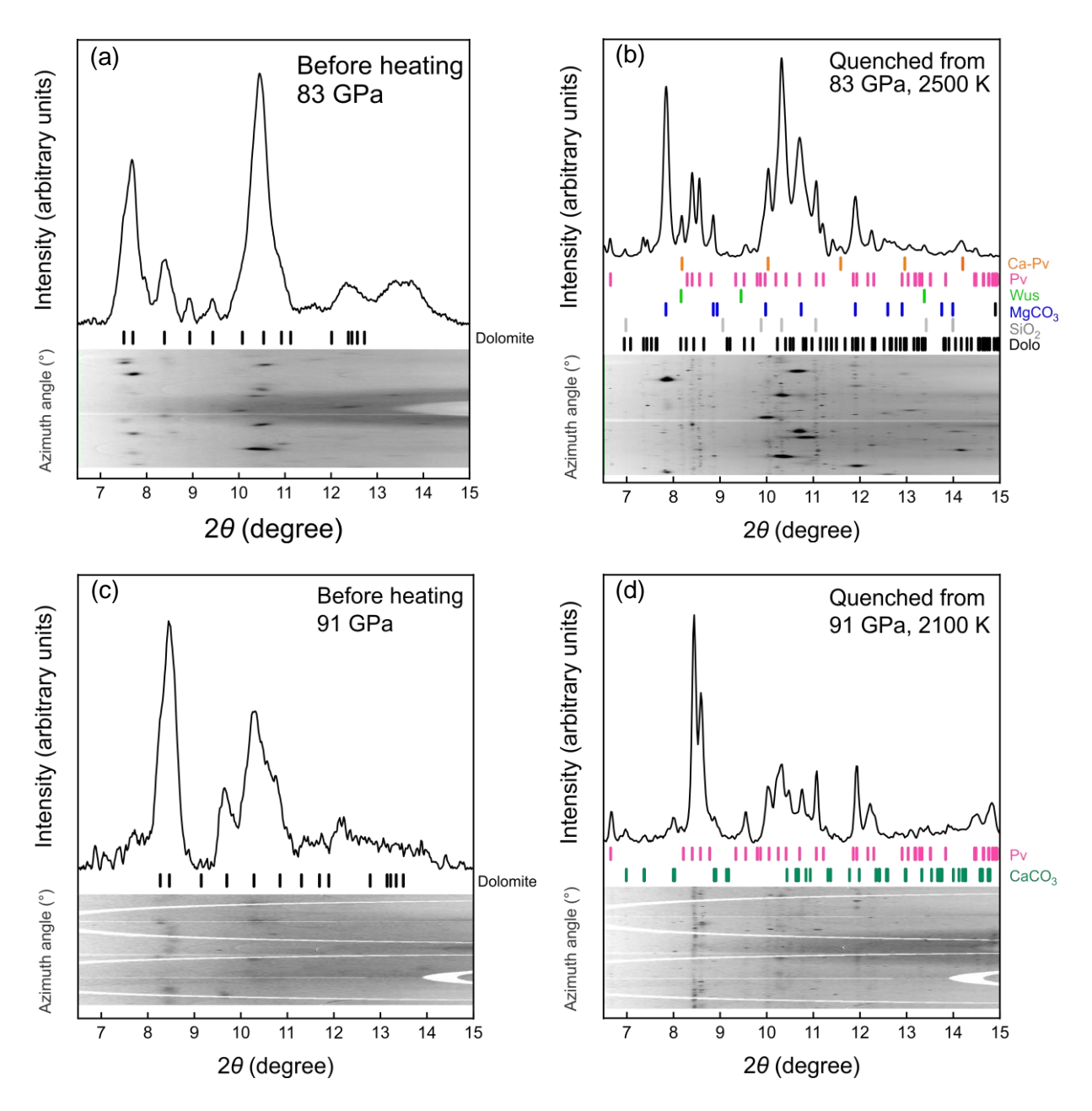


Figure 3-8: Representative unrolled X-ray diffraction images (lower panel) corresponding to X-ray diffraction patterns (upper panel) obtained from the starting materials of CaC-to-MgC before heating and the products quenched from various *P-T* conditions: (a-b) run #4, (c-d) run #5. Large spots in 2D diffraction patterns in (a) and (b) are from untransformed dolomite starting material. The wavelength of the incident X-ray beam was 0.3344 Å.

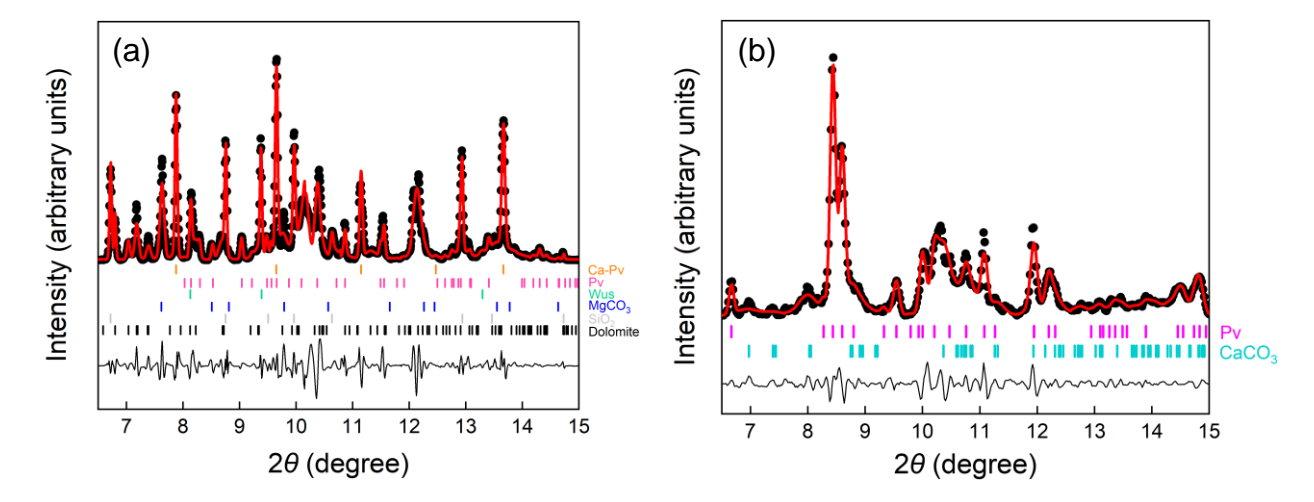


Figure 3-9: Representative full-profile fitting for XRD of (a) run #1 and (b) run #5. Le Bail refinements (red curves) of observed XRD data (black dots) were carried out after background subtraction, demonstrating all the identified phases (vertical ticks below patterns) can account for the peaks and intensities of XRD patterns. Black curves are fitting residues. The wavelength of the incident X-ray beam was 0.3344 Å.

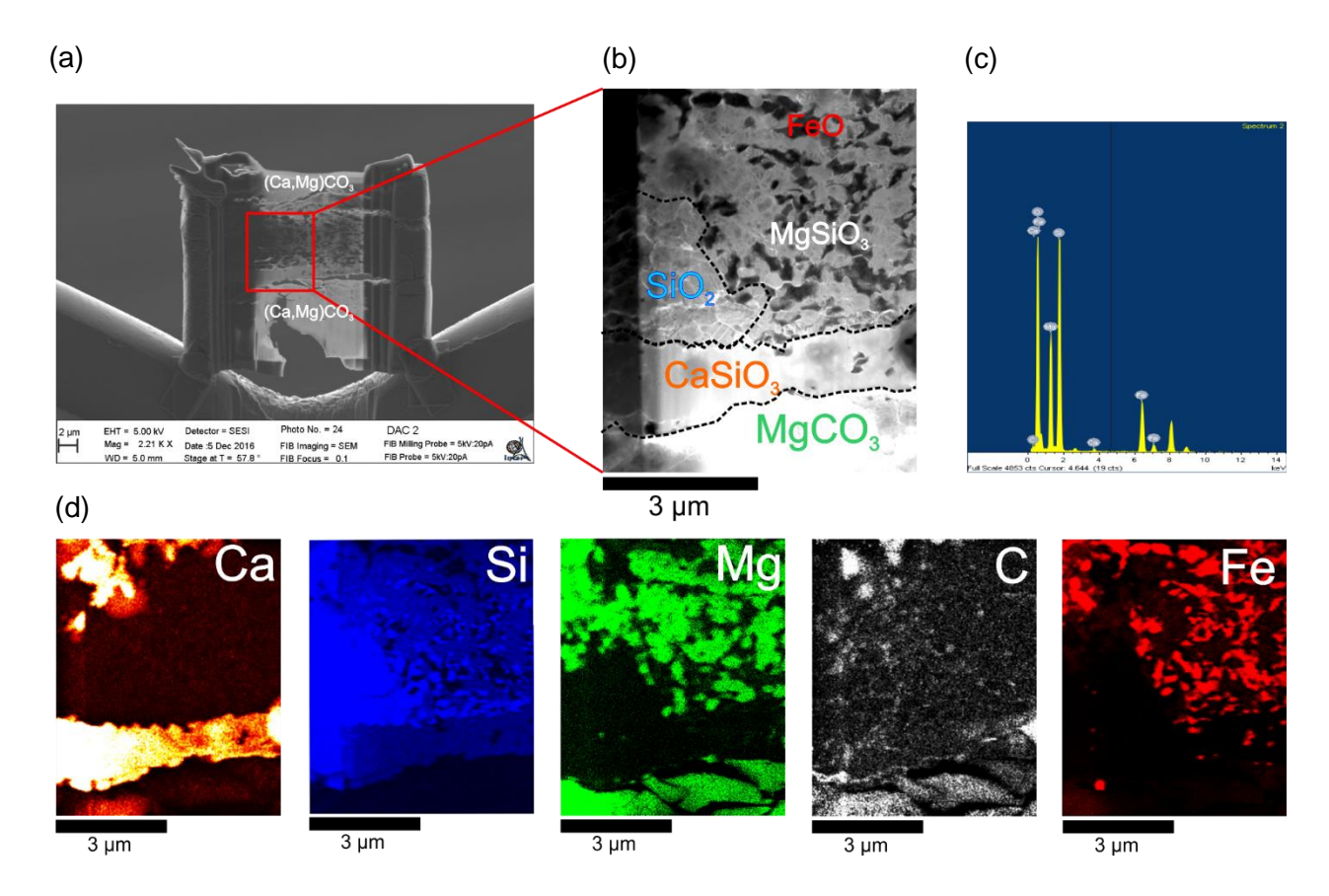


Figure 3-10: Ex-situ analysis of sample quenched from 33 GPa and 1650 K heated for 15 min (run #1) demonstrates CaC-to-MgC. (a) SEM-BSE image obtained during FIB milling. Sample was prepared as a (Mg,Fe)SiO₃ layer sandwiched by two (Ca,Mg)CO₃ layers; (b) dark-field STEM image reveals CaSiO₃ and MgCO₃, as well as SiO₂ and FeO, formed by reaction between (Mg,Fe)SiO₃ and (Ca,Mg)CO₃ layers; (c) EDX spectrum and corresponding (d) chemical maps for calcium, silicon, magnesium, carbon, and iron.

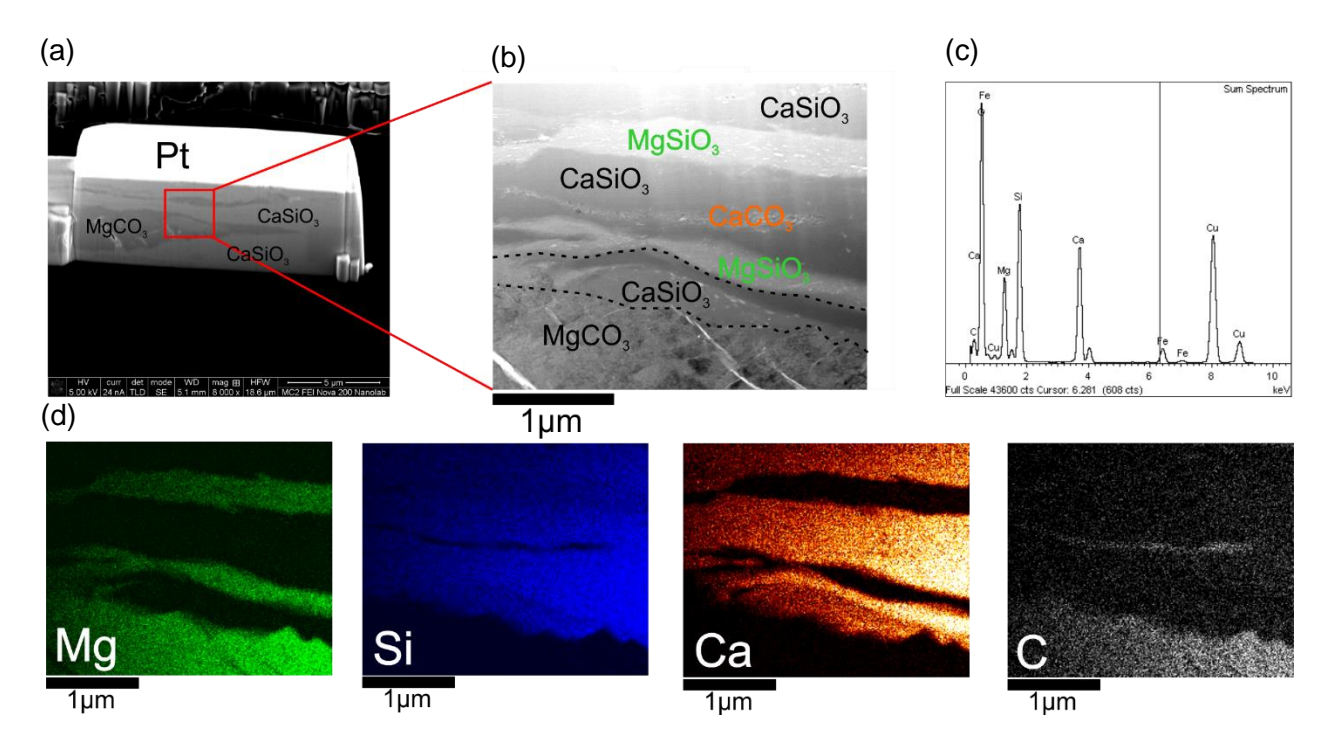


Figure 3-11: Ex-situ analysis of sample quenched from 88 GPa and 1800 K heated for 150 min (run #9) demonstrates MgC-to-CaC. (a) SEM-BSE image obtained during FIB milling. Sample was prepared as an (Mg,Fe)CO₃ layer sandwiched by two CaSiO₃ layers; (b) dark-field STEM image reveals (Mg,Fe)SiO₃ and CaCO₃ formed by reaction of (Mg,Fe)CO₃ and CaSiO₃ layers; (c) STEM-EDX spectrum and corresponding (d) chemical maps for magnesium, silicon, calcium, and carbon.

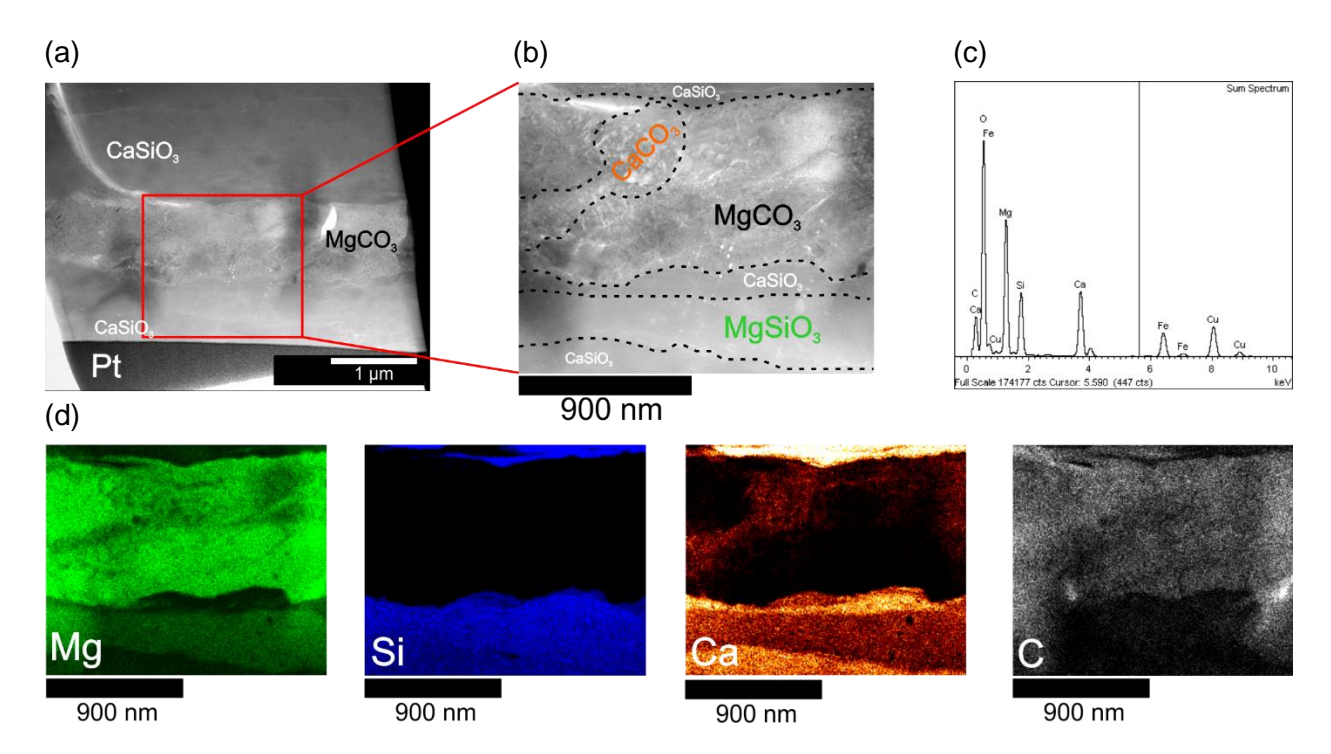


Figure 3-12: Ex-situ analysis of sample quenched from 133 GPa and 2000 K heated for 400 min (run #10) demonstrates MgC-to-CaC. (a) SEM-BSE image obtained during FIB milling. Sample was prepared as a (Mg,Fe)CO₃ layer sandwiched by two CaSiO₃ layers; (b) dark-field STEM image reveals (Mg,Fe)SiO₃ and CaCO₃ formed by reaction of (Mg,Fe)CO₃ and CaSiO₃ layers; (c) EDX spectrum and corresponding (d) chemical maps for magnesium, silicon, calcium, and carbon.

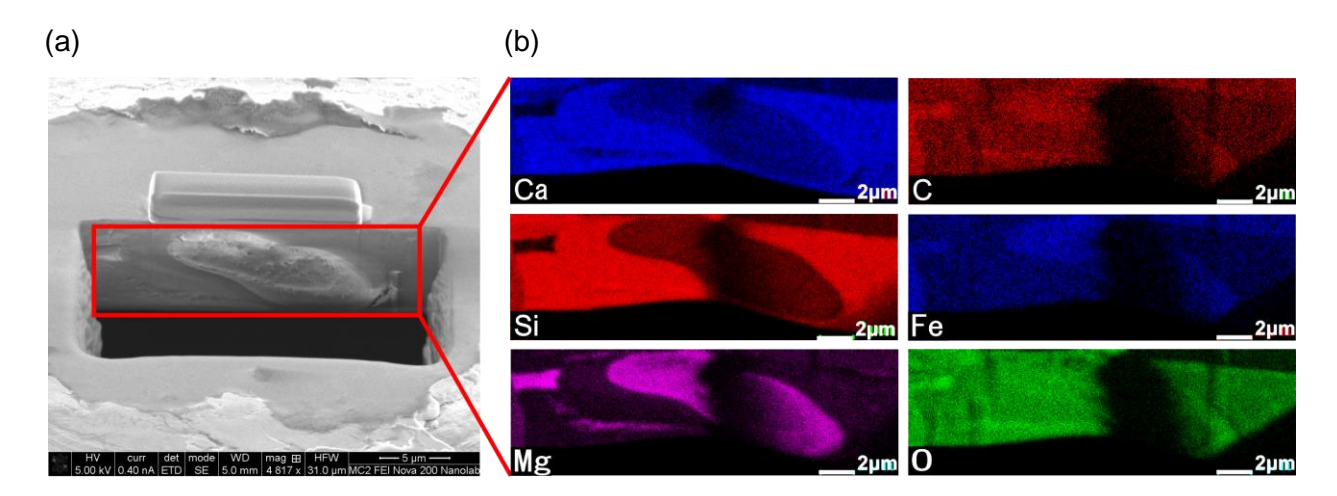


Figure 3-13: Ex-situ analysis of sample quenched from 35 GPa and 1900 K heated for 20 min (run #8) demonstrates MgC-to-CaC. (a) SEM-BSE image obtained during FIB milling. Sample was prepared as a (Mg,Fe)CO₃ layer sandwiched by two CaSiO₃ layers; (b) STEM-EDX chemical maps for calcium, silicon, magnesium, carbon, iron and oxygen.

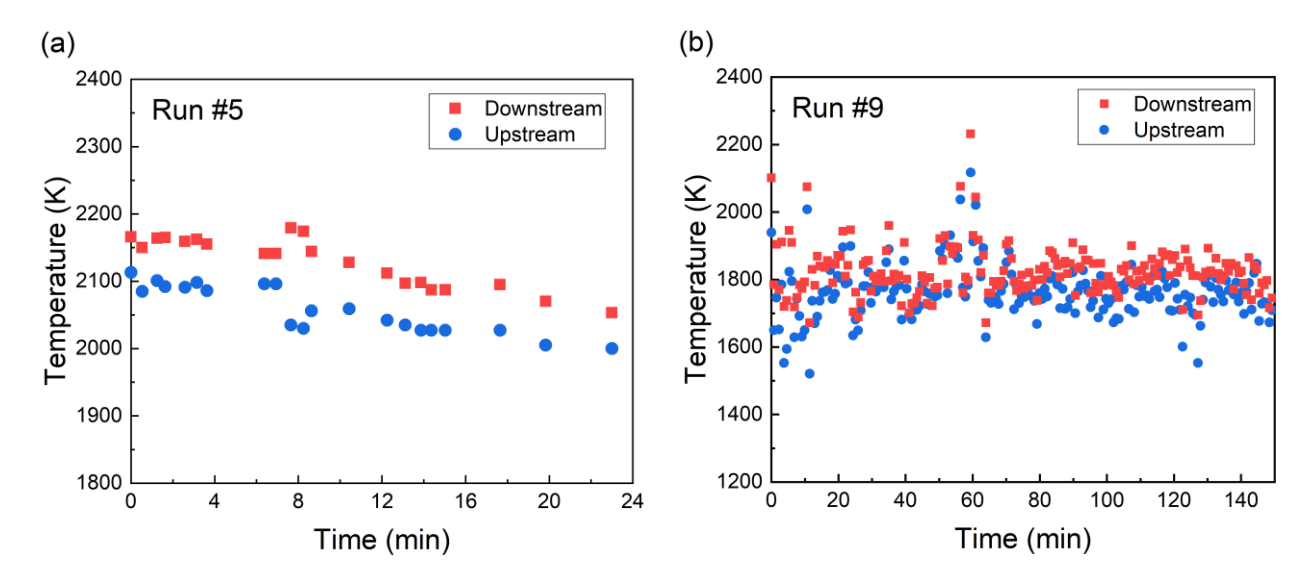


Figure 3-14: Typical temperature measurements of downstream (red squares) and upstream (blue circles) over heating duration of (a) run #5 for CaC-to-MgC and (b) run #9 for MgC-to-CaC, respectively.

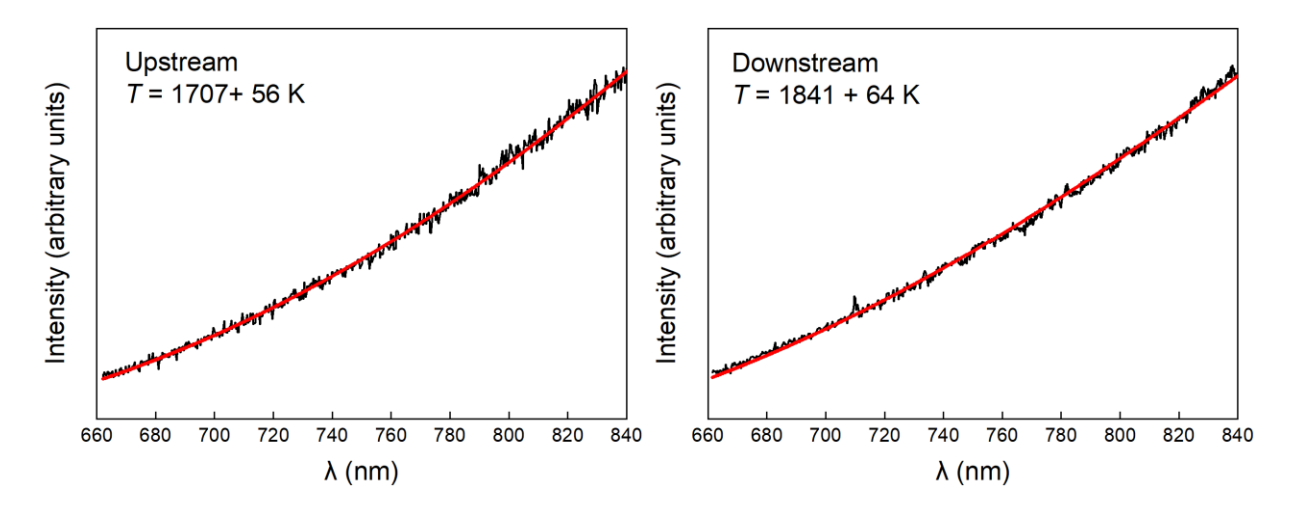


Figure 3-15: Representative temperature measurements and fitting profiles of upstream and downstream for run #9. Temperatures of the heated samples were determined by fitting the measured thermal radiation spectra using the Planck radiation function under the graybody approximation.

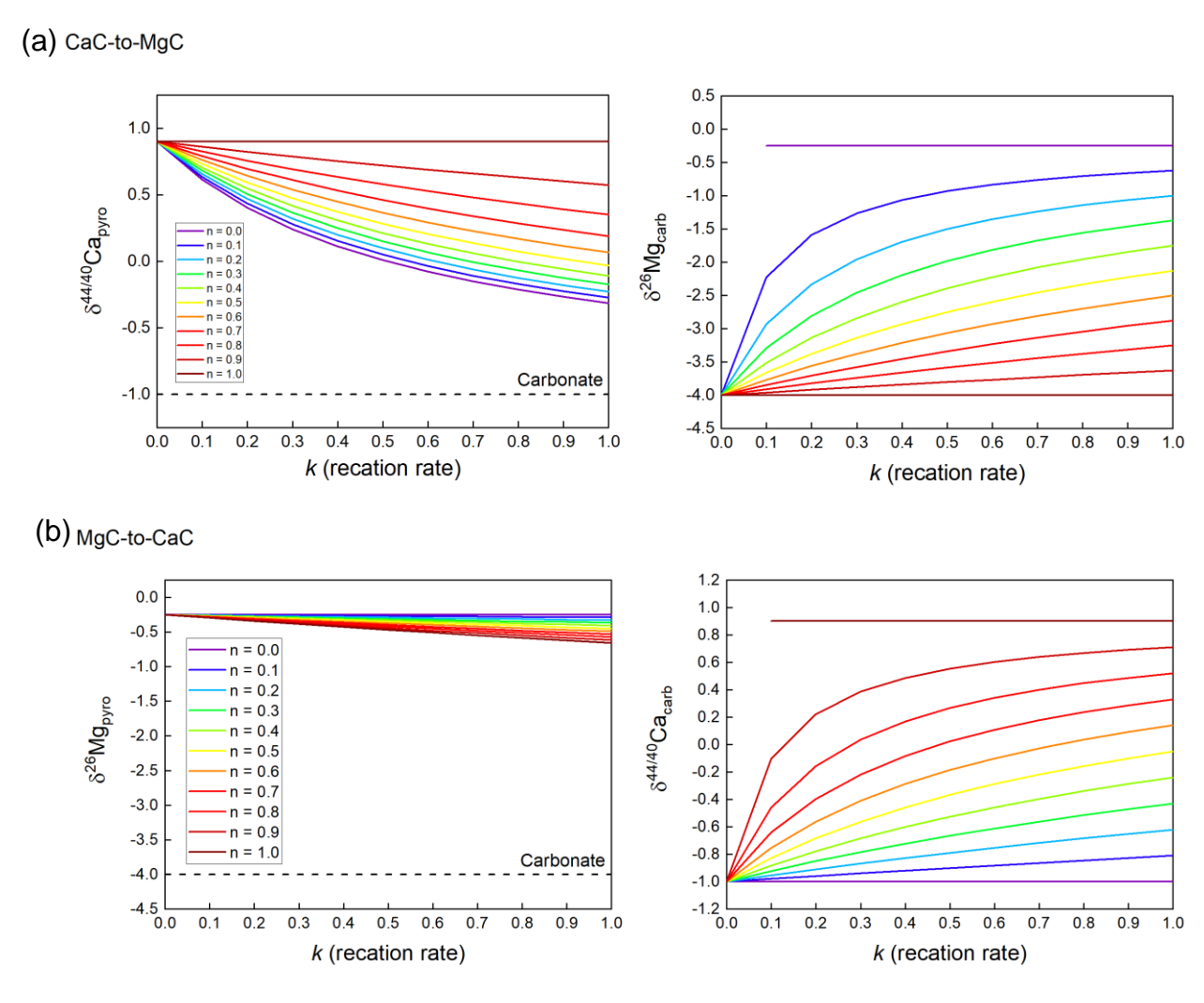


Figure 3-16: Calculated isotopic composition versus reaction rate after the reaction (a) CaC-to-MgC and (b) MgC-to-CaC. n represents the mole fraction of Mg in $(Mg_nCa_{n-1})CO_3$. Black dashed line represents the average $\delta^{44/40}Ca$ and $\delta^{26}Mg$ values in carbonates, respectively.

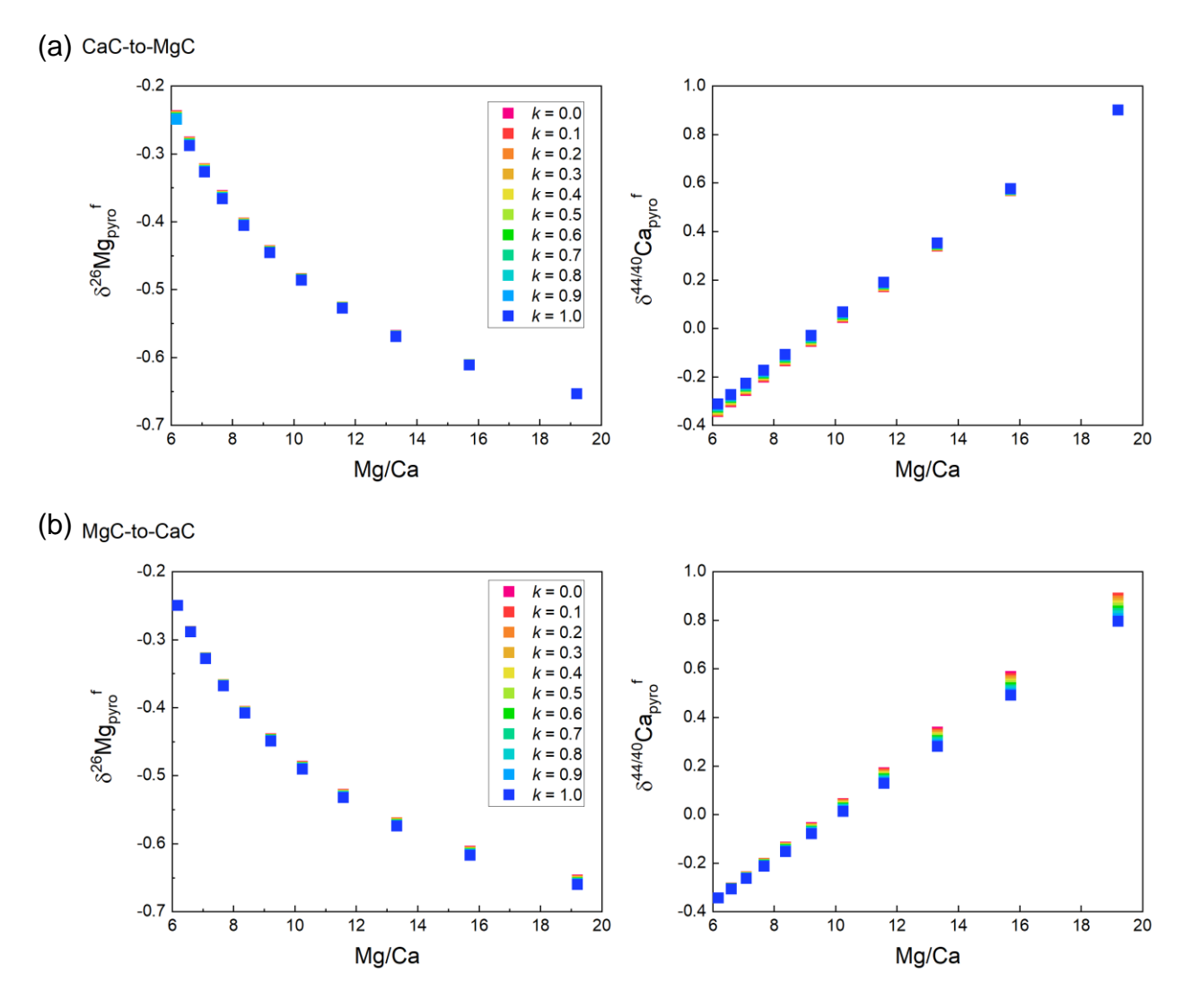


Figure 3-17: Calculated isotopic composition of carbonated pyrolite after isotopic fractionation between carbonates and silicates for the reaction (a) CaC-to-MgC and (b) MgC-to-CaC. The horizontal axis represents the mole ratio of Mg/Ca in the carbonated pyrolite. *k* represents reaction rate.

Table 3-1: Starting materials, experimental conditions, and run products for all experiments. Starting materials for experiments were loaded in sandwich configuration, with laser absorber layer between two thermal insulation layers. Pressures determined from Raman shift of the singlet peak of the diamond anvil at the culet surface (Akahama & Kawamura, 2006) with 2σ uncertainties. The temperature reported is the temporal average of recorded temperatures over the heating duration rounded to the nearest 50 K. Temperature fluctuations over this time scale were less than the specified uncertainty, which is derived from a standard deviation of temperature measurements from both sides of the laser-heated sample (typically ± 100 K below 2000 K and ± 150 K above 2000 K).

| Run # | Insulation | Laser absorber | P (GPa) | $T(\mathbf{K})$ | Heating | Phases observed after heating |
|-------|--------------------|------------------------|-------------|-----------------|----------------|--|
| | | | | | duration (min) | |
| 1 | $(Mg,Ca)CO_3$ | $(Mg,Fe)SiO_3$ | $33(2)^{a}$ | 1650(100) | 15 | $CaSiO_3 + SiO_2 + FeO + MgSiO_3 + MgCO_3$ |
| 2 | $(Mg,Ca)CO_3$ | $(Mg,Fe)SiO_3$ | 45(2) | 1600(100) | 20 | $CaSiO_3 + MgSiO_3 + MgCO_3$ |
| 3 | $(Mg,Ca)CO_3$ | $(Mg,Fe)SiO_3$ | 66(3) | 1900(100) | 11 | $CaSiO_3 + MgSiO_3 + MgCO_3$ |
| 4 | $(Mg,Ca)CO_3$ | $(Mg,Fe)SiO_3$ | 83(4) | 2500(150) | 20 | $CaSiO_3 + MgSiO_3 + MgCO_3$ |
| 5 | $(Mg,Ca)CO_3$ | $(Mg,Fe)SiO_3$ | 91(5) | 2100(150) | 24 | $MgSiO_3 + CaCO_3$ |
| 6 | $(Mg,Ca)CO_3$ | $(Mg,Fe)SiO_3$ | 106(5) | 2000(150) | 10 | $MgSiO_3 + CaCO_3$ |
| 7 | $(Mg,Ca)CO_3$ | $(Mg,Fe)SiO_3$ | 137(7) | 2800(150) | 15 | $MgSiO_3 + CaCO_3$ |
| 8 | CaSiO ₃ | (Mg,Fe)CO ₃ | 35(2) | 1900(100) | 20 | $CaSiO_3 + MgCO_3$ |
| 9 | CaSiO ₃ | $(Mg,Fe)CO_3$ | 88(4) | 1800(100) | 150 | $MgSiO_3 + CaCO_3 + CaSiO_3 + MgCO_3$ |
| 10 | CaSiO ₃ | $(Mg,Fe)CO_3$ | 133(7) | 2000(150) | 400 | $MgSiO_3 + CaCO_3 + CaSiO_3 + MgCO_3$ |

^a Numbers in parenthesis are uncertainties on the last digits.

Table 3-2: Parameters for isotopic mass balance calculations (see Supplementary Note 1 for details).

| Parameter | Value | Reference |
|--|---------|--------------------------|
| $\delta^{44/40}$ Ca _{pyro} ⁱ | 0.9 ‰ | Kang et al. (2017) |
| $\delta^{44/40} \mathrm{Ca_{carb}}^{\mathrm{i}}$ | -1.0 ‰ | Fantle and Tipper (2014) |
| $\delta^{26}{ m Mg_{pyro}}^{ m i}$ | -0.25 ‰ | Teng et al. (2010) |
| $\delta^{26}{ m Mg_{carb}}^{ m i}$ | -4.0 ‰ | Wombacher et al. (2011) |
| CaO abundance in pyrolite | 3.17 % | Workman and Hart (2005) |
| MgO abundance in pyrolite | 38.73 % | Workman and Hart (2005) |
| $\Delta^{44/40}\mathrm{Ca}_{\mathrm{pyro-carb}}$ | -0.05 ‰ | Amsellem et al. (2020) |
| $\Delta^{26}{ m Mg}$ pyro-carb | 0.06 ‰ | Macris et al. (2013) |

Chapter 4 Spin transitions and compressibility of ϵ -Fe₇N₃ and γ '-Fe₄N: implications for iron alloys in terrestrial planet cores

This chapter has been published as Lv et al. (2020b).

4.1 Abstract

Iron nitrides are possible constituents of the cores of Earth and other terrestrial planets. Pressure-induced magnetic changes in iron nitrides and effects on compressibility remain poorly understood. Here we report synchrotron X-ray emission spectroscopy (XES) and X-ray diffraction (XRD) results for ε -Fe₇N₃ and γ '-Fe₄N up to 60 GPa at 300 K. The XES spectra reveal completion of high- to low-spin transition in ε-Fe₇N₃ and γ'-Fe₄N at 43 and 34 GPa, respectively. The completion of the spin transition induces stiffening in bulk modulus of ε-Fe₇N₃ by 22% at ~40 GPa, but has no resolvable effect on the compression behavior of γ'-Fe₄N. Fitting pressure-volume data to the Birch-Murnaghan equation of state yields $V_0 = 83.29 \pm 0.03$ (Å³), $K_0 = 232 \pm 9$ GPa, K_0 ' = 4.1 ± 0.5 for nonmagnetic ε -Fe₇N₃ above the spin transition completion pressure, and V_0 = $54.82\pm0.02 \text{ (Å}^3)$, $K_0 = 152\pm2 \text{ GPa}$, $K_0' = 4.0\pm0.1 \text{ for } \gamma'\text{-Fe}_4\text{N}$ over the studied pressure range. By re-examining evidence for spin transition and effects on compressibility of other candidate components of terrestrial planet cores, Fe₃S, Fe₃P, Fe₇C₃, and Fe₃C based on previous XES and XRD measurements, we located the completion of high- to low-spin transition at ~67, 38, 50, and 30 GPa at 300 K, respectively. The completion of spin transitions of Fe₃S, Fe₃P and Fe₃C induces elastic stiffening, whereas that of Fe₇C₃ induces elastic softening. Changes in compressibility at completion of spin transitions in iron-light element alloys may influence the properties of Earth's and planetary cores.

4.2 Introduction

The Fe-Ni alloy that comprises the Earth's core must also contain light elements based on both geophysical observations (Birch, 1952) and compositions of planetary building blocks (Mcdonough & Sun, 1995), with potential implications for volatile storage and cycling within our planet. The leading candidate light elements for Earth's core include silicon, oxygen, sulfur, carbon, and hydrogen (Poirier, 1994); in addition to a possible mixture of these, nitrogen has been more recently proposed as a candidate light element in the core (e.g., Kusakabe et al., 2019; Minobe et al., 2015) based on structural stability and physical properties of iron nitrides (β-Fe₇N₃) extrapolated to core conditions. Additional support for the presence of iron nitrides in planetary interiors is provided by observations of iron nitrides in iron meteorites (Rubin & Ma, 2017) and in inclusions in superdeep diamonds, which potentially incorporate material from Earth's coremantle boundary region (Kaminsky & Wirth, 2017) or locally reduced domains of Earth's mantle (Zedgenizov & Litasov, 2017). The behavior of nitrogen-bearing iron alloys and compounds at conditions relevant to both accretion and the modern core is thus important to evaluate the potential abundance of nitrogen in Earth's interior (e.g., Kusakabe et al., 2019; Litasov et al., 2017b; Liu et al., 2019; Minobe et al., 2015). The few constraints on the identities and abundances of core light elements include observed seismological characteristics of Earth's inner and outer core, particularly ~4-7% density deficit of the core relative to properties of Fe-Ni noted since (Birch, 1952). Available constraints on thermoelasticity of solid iron nitrides from previous studies (e.g., Adler & Williams, 2005; Breton et al., 2019; Kusakabe et al., 2019; Litasov et al., 2017b) can be extrapolated for comparison to Earth's core, but extrapolation depends on stability and electronic/magnetic properties of these materials under high pressure conditions which remain poorly understood.

A wide range of stable iron nitride compounds with varying stoichiometries are stabilized by different conditions (De Waele et al., 2019; Wriedt et al., 1987). Stable iron nitrides at 1 bar include nonstoichiometric ε -Fe₃N_x (0.75 < x < 1.4) with iron atoms arranged in a hexagonal-closepacked structure, and stoichiometric γ'-Fe₄N adopting a cubic-close-packed structure (Widenmeyer et al., 2014; Wriedt et al., 1987). Previous studies have identified additional structures in the Fe-N system stabilized by high pressure (e.g., De Waele et al., 2019; Wetzel et al., 2019; Widenmeyer et al., 2014). The ε -Fe₇N₃ structure (same stoichiometry as Fe₃N_{x=1,3}, space group P6₃22) remains stable up to 51 GPa and 300 K (Adler & Williams, 2005), and was observed to transform to β-Fe₇N₃ above 41 GPa and ~1000 K (Minobe et al., 2015). γ'-Fe₄N (space group $Pm \ \bar{3} \ m$) is predicted to decompose to β -Fe₇N₃ + ϵ -Fe at ~56 GPa and 300 K based on thermodynamic analysis (Breton et al., 2019). At high temperatures, γ '-Fe₄N was observed to transform to ε -Fe₄N above 1373 K and 8.5 GPa (Guo et al., 2013), and decompose to Fe + β -Fe₇N₃ above 41 GPa at ~1000 K (Minobe et al., 2015). β-Fe₇N₃ was observed to remain stable up to 3100 K and 135 GPa, and proposed to exist in the Earth's solid inner core (Kusakabe et al., 2019). In addition, a new crystal structure of Fe₇N₃ with space group C2/m was predicted to be stable under Earth's core conditions (Sagatov et al., 2019). However, due to the complex stoichiometries and structural variations in iron nitrides at high pressure and temperature conditions, understanding of high-pressure phase stability in this system remains incomplete.

The effects of incorporating nitrogen in iron alloys and compounds include not only modifying stable crystalline structure, but also the arrangement and bonding style of electrons in d orbitals around iron atoms that control magneto-elastic properties (e.g., Sifkovits et al., 1999; Widenmeyer et al., 2014). Electronic structure of iron nitrides have been investigated by first principles calculations and experimental measurements, which indicate that the chemical bonding

in ε-Fe₇N₃ (e.g., Zhang et al., 2012) and γ-Fe₄N (e.g., dos Santos & Samudio Pérez, 2016) are complex mixtures of metallic, covalent, and ionic characters. Additionally, iron nitrides undergo pressure-induced magnetic transitions, which may affect thermodynamics and elasticities of Fe-N alloys and compounds at high pressures (e.g., dos Santos & Samudio Pérez, 2016; Ishimatsu et al., 2003; Popov et al., 2015). At 1 bar, the d-orbital electrons in Fe in all known Fe-N compounds adopt a high-spin ferromagnetic arrangement and are remarkable for high saturation of magnetism (which generally decreases with N concentration): the magnetic moment of ε -Fe₃N_x ranges from 2.0 to 0.2 μ_B per Fe atom as N concentration increases from x = 1 to 1.48 (Leineweber et al., 2001), while the magnetic moment of γ '-Fe₄N is 2.3 μ _B per Fe atom (Dirba et al., 2015). Only a few highpressure studies on magnetism of the Fe-N system exist, and the magnetic transition pressures of iron nitrides and their effects on elasticities are largely unknown. Experiments on pressure-induced magnetic transitions of ε -Fe₃N_x have not been conducted. γ '-Fe₄N undergoes a ferromagnetic to paramagnetic transition at 24 GPa and 300 K as resolved by X-ray magnetic circular dichroism (XMCD) measurements (Ishimatsu et al., 2003), while first-principles calculations predicted the magnetic to nonmagnetic transition in γ'-Fe₄N occurs at 250 GPa (Popov et al., 2015). Systematic experimental constraints on pressure-induced magnetic transitions in both ε-Fe₃N_x and γ'-Fe₄N from ferromagnetic to paramagnetic or nonmagnetic state and the coupling between these electronic arrangements and elasticities and phase stability are necessary for an improved understanding of the physical properties of iron nitrides.

The identification of magneto-elastic coupling behavior in other iron alloy systems such as Fe-C, Fe-S, and Fe-P (recently reviewed by Caracas, 2016) provides additional motivation to test whether the Fe-N system behaves similarly. In the electronically- and structurally-similar Fe-C system, ferromagnetic (FM) Fe-C compounds undergo transitions first to a paramagnetic (PM)

state, and then to a low-spin non-magnetic (NM) state, and these transitions have been proposed to significantly affect compressibility of Fe-C materials (e.g., Chen et al., 2012; Chen et al., 2018a; Lin et al., 2004b; Mookherjee et al., 2011; Prescher et al., 2012). The pressure-induced magnetic transition of Fe-S (e.g., Chen et al., 2007; Lin et al., 2004a) and Fe-P compounds (e.g., Gu et al., 2014, 2016; Lai et al., 2020) have also been reported as well to affect compressibility and sound velocities. Due to the lack of characterization of electronic states at high pressures in previous studies of compression and phase transitions of iron nitrides (e.g., Adler & Williams, 2005; Breton et al., 2019; Litasov et al., 2017b), the amount and role of N in Earth's core relative to other candidate light elements remains poorly constrained.

Magnetic transitions at high pressures have been experimentally detected using methods that directly characterize electronic states, as well as methods that indirectly assess magnetism through its effects on elasticity and compression behavior. The total spin moment of Fe, ranging from high to low spin, can be characterized by X-ray emission spectroscopy (XES). The appearance of the satellite emission peak $K_{\beta'}$ located at the lower energy relative to the main emission peak $K_{\beta 1,3}$ is a result of the 3p-3d core-hole exchange interaction in the final state of the emission process. That is, the intensity of the satellite peak depends on the spin polarization of the 3d shell and is sensitive to the net magnetic spin state. The collapse of the magnetization of Fe is characterized by the disappearance of the low-energy satellite due to the loss of 3d magnetic moment (e.g., Badro et al., 2003; Badro et al., 2004). Therefore, the local spin moment change of iron atoms revealed by XES can distinguish between high-spin (FM or PM) states vs. low-spin (NM) states. XES spectroscopy performed at high pressures using a synchrotron X-ray source has been used to study magnetic spin transitions in Fe-C, Fe-S, and Fe-P compounds (e.g., Chen et al., 2018a; Chen et al., 2014; Gu et al., 2016; Lin et al., 2004b; Shen et al., 2003). Characterizing

magneto-elastic coupling requires complementary information provided by spectroscopic methods such as X-ray emission and structural/elastic methods such as X-ray diffraction to confirm magnetic transitions and discontinuous compression behavior operate in tandem (e.g., Chen et al., 2014). However, no such study has been conducted in the Fe-N system.

Here we present a systematic study of magnetic transitions and compressibility of ironnitrides, ε -Fe₇N₃ and γ '-Fe₄N, using synchrotron XES and XRD measurements up to 60 GPa at 300 K. Compression behavior of both compounds is monitored by dense pressure-volume (*P-V*) data coverage, combined with total spin moment indicated by XES, to determine any effects of magnetic transitions on the incompressibility of iron nitrides. Observed behavior is compared to the effect of magneto-elastic coupling in other Fe alloys studied using the same protocol.

4.3 Experimental methods

High purity nonstoichiometric ε-Fe₇N₃ and γ'-Fe₄N powders (99.9%, Kojundo Chemical Lab. Co. Ltd., average grain size ~1 μm) were used as starting materials. XRD for both samples at ambient conditions confirms unit cell volumes in good agreement with previous studies of ε-Fe₇N₃ (Adler & Williams, 2005; Kusakabe et al., 2019; Litasov et al., 2017b; Minobe et al., 2015) and γ'-Fe₄N (Adler & Williams, 2005; Guo et al., 2013). For the nonstoichiometric ε-Fe₇N₃, the ambient volume measured for our sample $V_0 = 86.32(\pm 0.01)$ Å³ is consistent with a linear relationship between unit-cell volume and nitrogen content in ε-Fe₃N_x, V = 10.637x + 72.858 (Litasov et al., 2017b) when x is 1.27.

XES of ϵ -Fe₇N₃ and γ '-Fe₄N was measured up to 60 GPa at intervals of ~5 GPa. Compression in the diamond anvil cell (DAC) was performed using two pairs of diamond anvils with 200- μ m flat culet. In each DAC, a flake of ϵ -Fe₇N₃ (~ 20 × 20 × 10 μ m³) or γ '-Fe₄N (~ 15 ×

 $23 \times 10 \,\mu\text{m}^3$) sample was loaded in a 100- μ m diameter sample chamber confined by a pre-indented Be gasket. The sample chamber was drilled in the center of the Be gasket with pre-indented thickness of ~30 µm using the laser drilling system at HPCAT (Sector 16) at the Advanced Photon Source (APS), Argonne National Laboratory (ANL) (Hrubiak et al., 2015). Silicone oil (Alfa Aesar) served as the pressure-transmitting medium and a 5-µm ruby ball was loaded into the sample chamber as the pressure standard. Pressures were determined by ruby fluorescence (Mao et al., 1986) before and after each XES collection, and differed by up to 10% due to relaxation of the sample or cell assembly. The XES measurements were performed at 300 K at beamline 16-ID-D of the APS, ANL. The incident X-ray beam was focused to 5×7 μm² full width at half maximum at the sample position. The fluorescence signal was observed through the Be gasket. The incident X-ray energy was 11.3 keV with a bandwidth of ~1 eV was used for the experiments. Fe K_{β} emission was selected by silicon analyzer and reflected to a silicon detector with an energy step of about 0.3 eV. Each spectrum was recorded for about 40 min and 3 spectra were taken to accumulate at least 30,000 counts at the Fe K_{β} main peak at each pressure. All spectra were normalized to area and aligned to the position of the Fe K_{β} main peak (Figure 4-2). The high-spin reference is the sample spectrum at 1 bar, and low-spin references are the spectrum of FeS₂ at 1 bar collected using the same setup and the sample spectrum at 60 GPa. Intensity difference between the sample and references was integrated over the energy range of the satellite K_{β} ' peak (7030-7053.0 eV) using the integrated relative difference method (Mao et al., 2014). Uncertainty in total spin moment was determined based on difference in calculations using FeS₂ vs. pressurized sample as low-spin references.

XRD measurements were carried out at 300 K up to 60 GPa with 1-2 GPa steps. The sample flakes of ϵ -Fe₇N₃ (\sim 20 \times 20 \times 10 μ m³) and γ '-Fe₄N (\sim 15 \times 23 \times 10 μ m³) were loaded side-by-

side in the sample chamber of a DAC with a pair of 300-µm-culet diamonds. The sample chamber was drilled in the center of the Re gasket with a pre-indented thickness of ~30 μm using the laser drilling system at HPCAT (Hrubiak et al., 2015). Au powder (>99.95%, Goodfellow) was spread on top of the samples to serve as the pressure calibrant (Fei et al., 2007). Because the Au (111) peak overlapped with of ε -Fe₇N₃ (110) peak, we use the pressure calculated from Au at the position of the γ'-Fe₄N sample to represent the pressure at all sample positions. A flake of pure Fe (>99.997%, Alfa Aesar) with a size of $\sim 25 \times 23 \times 10 \ \mu \text{m}^3$ was loaded alongside the samples as a secondary reference to monitor the hydrostaticity of stress conditions in the sample chamber (Liu et al., 2016). Ne was loaded into the sample chamber as the pressure-transmitting medium using the COMPRES/GSECARS gas-loading system (Rivers et al., 2008). The uncertainties in pressures were propagated from the standard deviation of the unit-cell volumes of Au and Ne (if applicable). Angle-dispersive X-ray diffraction measurements were performed at beamline 13-BM-C of the APS, ANL. The incident X-ray beam had a monochromatic wavelength of 0.434 Å and was focused to $\sim 15 \times 15 \,\mu\text{m}^2$. Two-dimensional X-ray diffraction images were recorded on a MAR165 CCD detector and the sample-to-detector distance and the tilt angle of the detector relative to the incident X-ray beam were calibrated using 1-bar diffraction of the NIST 660a LaB₆ standard. Xray diffraction images of ε-Fe₇N₃, γ'-Fe₄N, and Fe were exposed for 60 s. At each pressure, the XRD patterns were integrated using Dioptas software (Prescher & Prakapenka, 2015). For selected pressures (lowest, highest, and one intermediate pressure), crystal structures were confirmed from XRD data using the full spectrum Le Bail fitting technique (Le Bail, 2012) implemented in the EXPGUI/GSAS software package (Toby, 2001).

4.4 Results

4.4.1 No structural transition of Fe₇N₃ or Fe₄N

XRD patterns for both iron nitrides within the investigated pressure range at 300 K show sharp and intense peaks from the sample, Au, Ne, and Re, and no new diffraction lines nor splitting of lines were observed. The lattice parameters of ϵ -Fe₇N₃ were obtained by fitting diffraction lines (002), (111) and (112), and that of γ '-Fe₄N was fit from diffraction lines (111) and (200) using PDIndexer (Seto et al., 2010). The uncertainty in the lattice parameters corresponds to one standard deviation obtained in fit using multiple XRD peaks. The pressure at each step was calculated from the lattice parameters of Au by fitting the diffraction lines (111) and (200), and from Ne by fitting (111) and (200) peaks at ~19-60 GPa as well (Table 4-2, Table 4-3, Table 4-4). The uncertainties of pressures were propagated from uncertainties of unit cell volumes of Au and Ne, and uncertainties of their equation of state parameters (Fei et al., 2007).

Diffraction data of ε -Fe₇N₃ were refined using a $P6_322$ space group (averaged wRp = 2.2 %, representatives shown in Figure 4-1a and b) up to 60 GPa. Le Bail refinements of the structure of γ '-Fe₄N were performed with the $Pm\overline{3}m$ space group (averaged wRp = 1.8 %, representatives shown in Figure 4-1c and d) up to 60 GPa. Note that previous work indicates that ε -Fe₇N₃ is metastable above ~40 GPa (Minobe et al., 2015), and γ '-Fe₄N is metastable above ~56 GPa (Breton et al., 2019). Both samples continue to adopt the initial structures without dissociation or phase transition up to 60 GPa at 300 K, but above 40 GPa we assume that ε -Fe₇N₃ is structurally metastable.

4.4.2 Spin states of ε -Fe₇N₃ and γ '-Fe₄N

The net magnetic spin state of 3d electrons of Fe in ε -Fe₇N₃ and γ '-Fe₄N can be probed by XES spectra of the K_{β} fluorescence lines. At ambient conditions, the XES spectra for both iron

nitrides are composed of a dominant $K_{\beta 1,3}$ peak and a lower-energy satellite K_{β} ' peak, as a result of the 3p core-hole-3d exchange interaction in the final state of the emission process, consistent with iron entirely in the high-spin state (Figure 4-2a and b). The intensity of the satellite peak in the magnetic/high spin state is lower than that of iron oxides such as FeO and Fe₂O₃ (Badro et al., 2003; Badro et al., 2002), but similar to that of pure iron and iron alloys (such as Fe-C, Fe-P, Fe-S alloys). As pressure increases, the integrated K_{β} peak intensity begins to decrease. The observed decrease demonstrates that the onsets of spin transitions in both compounds are nearly immediate upon compression and no higher than 10 GPa in ε -Fe₇N₃ and 5 GPa in γ '-Fe₄N. The integrated K_{β} ' peak of ε -Fe₇N₃ and γ '-Fe₄N disappears at 43 and 34 GPa, respectively, with no further change up to 60 GPa (Figure 4-2c and d). The decrease of total spin moment of Fe as a function of pressure illustrates both ε-Fe₇N₃ and γ'-Fe₄N undergo a gradual spin-pairing transition from high to lowspin state, with Fe in ε-Fe₇N₃ and γ'-Fe₄N fully in low-spin state at pressures higher than 43 and 34 GPa, respectively (Figure 4-2c and d). Spin transition pressures are expected to be upper bounds due to possible effects of pressure hysteresis and non-hydrostatic stress on the spin crossover upon compression (Lin et al., 2013). Observed changes in XES spectra of ε-Fe₇N₃ and γ'-Fe₄N correspond to magnetic to nonmagnetic (high to low spin) transitions, but the ferromagnetic to paramagnetic transition, depending on the relative orientations of the individual spins, cannot be detected by XES. However, both ferromagnetic-paramagnetic and magnetic-nonmagnetic transitions may be detected via XRD if they take place and affect compressibility.

4.4.3 Compression behavior of ε -Fe₇N₃ and γ '-Fe₄N

Pressure-volume (P-V) data obtained from XRD of ε -Fe₇N₃ and γ '-Fe₄N at 300 K demonstrate smooth compression without discontinuity in volume (Figure 4-3a and Figure 4-4a). Second-order and order-disorder transitions such as magnetic transitions may be continuous in

volume but discontinuous in the higher-order derivatives of P(V) (Vocadlo et al., 2002). Subtle effects on the unit cell volume with abrupt changes in incompressibility may be emphasized by the relationship between the Eulerian finite strain ($f_E = [(V_0/V)^{2/3}-1]/2$) versus the normalized stress ($F_E = P/[3f_E(1+2f_E)^{5/2}]$) (Angel, 2000) as in previous studies (Chen et al., 2012; Liu et al., 2016). However, it is important to note that the calculation of both F_E and f_E requires priori knowledge of the 1-bar volume (V_0), and using an incorrect value of V_0 produces an anomalous curvature in the f-F plot (Angel, 2000). Thus, to avoid the bias caused by V_0 of the unquenchable nonmagnetic phase, we plot the effective strain ($g = [(V_0/V)^{2/3}-1]/2$), same as f_E , versus the normalized stress ($G = P/[3(1+2g)^{3/2}]$) following the formalism (Jeanloz, 1981) for ε -Fe $_7N_3$ and γ '-Fe $_4N$ (Figure 4-3b and Figure 4-4b), respectively.

As is shown in Figure 4-3b, the g-G plot of ε -Fe₇N₃ reveals that the pressure-dependent stress exhibits a linear response to applied strain up to 40 GPa within the established errors. Above 40 GPa, the slope of linearized g-G increases, implying a discontinuity of compression behavior and an increase in the incompressibility given that dG/dg is positively correlated with (K_0+P) . This pressure is within the uncertainty of the completion of the magnetic to nonmagnetic transition (i.e., completion of spin transition) pressure of ~40 GPa determined independently by XES, indicating the elastic stiffening coincides with the magnetic collapse of Fe in ε -Fe₇N₃. In addition, this change of compressibility is similar to the pressure of ε - to β -Fe₇N₃ transition (Minobe et al., 2015) observed with laser-heating to promote equilibrium phase transitions. Due to the low pressure of the onset of the spin transition observed by XES, with upper bound ~10 GPa, and gradual, broad pressure range of the transition, it is difficult to resolve a transition from high to mixed spin state in the compression behavior. The compression behavior up to 40 GPa may thus represent the mixed-spin state. The crossing point of the g axis (i.e., G = 0) and the fitted curve constrain the

zero-pressure volume of the nonmagnetic (or low spin state) phase to 83.29 ± 0.03 Å³, with the error propagated from the error of linear fitting and volume at ambient conditions. No stiffening is observed at pressures lower than the spin transition pressure, so no clear evidence is available for any ferromagnetic-paramagnetic transition in ϵ -Fe₇N₃.

In contrast, the calculated G of γ '-Fe₄N can be linearized as a function of g within the investigated pressure range, and no discontinuity is observed (Figure 4-4b). That is, both onset and completion of spin transition of Fe have little effect on the compression behavior γ '-Fe₄N, and no anomalous compressibility behavior needs to be explained by any other magnetic transition such as a ferromagnetic-paramagnetic transition.

Discontinuities in higher derivatives of compression behavior can also be generated by nonhydrostatic stress in the sample chamber. To rule out this effect on iron nitrides, we consider the pressure gradient observed in Ne medium, microstrain in Au calibrant as determined by peak width, and the behavior of the Fe foil relative to previous measurements under quasi-hydrostatic conditions. The pressure difference determined from the Ne medium at positions of the two iron nitride samples is remains less than ~0.5 GPa up to the peak pressure of 60 GPa (Table 4-2, Table 4-3), consistent with the low strength of Ne. Nonhydrostatic stress generally results in diffraction peak broadening due to microstrain (e.g., Takemura & Dewaele, 2008). We choose the Au (111) peak obtained at the γ'-Fe₄N sample position (Figure 4-1c and d) to examine changes in diffraction peak width as a function of pressure. The normalized FWHM of the Au peak and its trend with pressure are comparable to previous measurements of Au foil and powder in He pressure medium (Takemura & Dewaele, 2008) (Figure 4-8), indicating hydrostatic conditions up to 17 GPa and quasi-hydrostatic conditions at higher pressures, in agreement with previous characterization of the stress gradient sustained by the pressure medium Ne (Klotz et al., 2009). In addition,

compression of both phases of pure Fe remains smooth over the entire pressure range and the condition of the phase transition and compressibility are in agreement with previous studies conducted under quasi-hydrostatic stress (e.g., Dewaele et al., 2006) (Figure 4-7). We investigated the P-V data and g-G plot of pure Fe loaded in the same sample chamber as a reference (Figure 4-7). The discontinuities of both compression curve and g-G plot of Fe at ~15 GPa reflect a phase transition of α - to ε -Fe, which is in good agreement with previous studies (Dewaele et al., 2006). Therefore, the change in hydrostaticity of Ne at ~17 GPa (Figure 4-8) was not manifested in the compression behavior of the samples, and the change in G-g at ~40 GPa of ε -Fe $_7$ N $_3$ is not associated with nonhydrostaticity. Relative to previous studies (Adler & Williams, 2005; Litasov et al., 2017b), the design of this study provides greater sensitivity to discontinuities in the compression behavior of ε -Fe $_7$ N $_3$ due to denser data coverage with pressure intervals of ~1 GPa (Figure 4-3a) and quasi-hydrostatic medium.

Given the compression and magnetic behaviors described above, we separately fit the P-V data of ε -Fe₇N₃ using third-order Birch-Murnaghan equation of state (BM3-EoS) over two distinct pressure ranges above and below 40 GPa, and that of γ '-Fe₄N with a single curve for the entire data range in order to better describe the compressibility. Below 40 GPa ε -Fe₇N₃ has a continuously-evolving, mixed-spin state, and the resulting EoS parameters are expected to be anomalously soft relative to the high-spin state. The parameters of the BM3-EoS, isothermal bulk modulus, K_0 , its pressure derivative, K_0 ', and volume at 1 bar V_0 , obtained in the present study and previous studies are summarized in Table 4-1.

The BM3-EoS parameters of magnetic, mixed spin ε-Fe₇N₃ obtained by fitting the *P-V* data from 1 bar and 40 GPa to BM3-EoS are compared with previous experimental constraints on the same stoichiometry (Adler & Williams, 2005; Litasov et al., 2017b) (Table 4-1), showing

consistency with the parameters obtained by (Litasov et al., 2017b) within uncertainties, whereas 5% (or higher given the tradeoff between K_0 and K_0) elastic softer than that constrained by (Adler & Williams, 2005). Figure 4-3a shows our measured P-V data are in good agreement with data obtained by (Litasov et al., 2017b) from 1 bar to 31 GPa using a multi-anvil press, supporting a quasi-hydrostatic conditions in this study. However, the volume data reported by Adler and Williams (2005) deviate from our measurements at pressures higher than 30 GPa, likely due to the nonhydrostatic stress supported by methanol:ethanol:water pressure transmitting medium. Properties predicted for magnetic ε -Fe₃N_{1,25} by density functional theory (Popov et al., 2015) are significantly offset, with V_0 lower by 6% and K_0 higher by 38% compared to experimental constraints. For nonmagnetic, low spin ε-Fe₇N₃, EoS fit for the data from 40 GPa to 60 GPa with a fixed V_0 [83.28(± 2) Å³] constrained by g-G plot (Figure 4-3b) yields K_0 45% higher than that of magnetic phase (22% increase in bulk modulus at 40 GPa, Figure 4-5), indicating a significant elastic stiffening associated with the magnetic collapse. Popov et al. (2015) predicted a magneticnonmagnetic transition of ε -Fe₇N₃ completed at 130 GPa, inducing a 35% difference in K_0 , but both the transition pressure and bulk modulus are much higher than our constraints (Table 4-1). An increase in incompressibility induced by the collapse of magnetic momentum has been observed in other Fe-alloys such as Fe₃C (Prescher et al., 2012) and Fe₃P (Lai et al., 2020). These alloys are also not observed to soften during the spin transition, in contrast to pressure-induced Invar behavior of Fe alloys such as Fe-Ni (Dubrovinsky et al., 2001) and Fe₇C₃ (Chen et al., 2012) which undergo elastic softening during the transition followed by reaching a stiffer nonmagnetic state.

The EoS parameters of γ '-Fe₄N derived by fitting the measured *P-V* data up to 60 GPa to BM3-EoS agree with the parameters reported by Adler and Williams (2005) and (Guo et al., 2013)

within uncertainties (Table 4-1). However, the K_0 reported by Breton et al. (2019), 169(±6) GPa, is 13% higher than our result, and the measured volumes deviate from our measurements as illustrated in Figure 4-4a. This discrepancy can be attributed to nonhydrostatic conditions in the sample chamber produced using KCl as the pressure transmitting medium, and lack of data at 0-20 GPa regime may cause a fitting bias when fixing the V_0 constrained by (Adler & Williams, 2005). K_0 computed by density functional theory with generalized gradient approximation studies (Niewa et al., 2009b; Popov et al., 2015) spans a range from 0 to 9% higher than that constrained by experiments, whereas the K_0 calculated from single-crystal elastic constants by first-principles total-energy method is 26% higher than that constrained by experiments. Popov et al. (2015) predicted a magnetic-nonmagnetic transition of γ '-Fe₄N completed at 250 GPa, inducing an +87.5% jump of K_0 , in contrast to our observation of this transition at much lower pressure with no significant effect on elasticity. γ '-Fe₄N is also less incompressible than both magnetic and nonmagnetic ε-Fe₇N₃, which leads to its destabilization at pressures above 60 GPa (Breton et al., 2019).

4.5 Discussion

4.5.1 Magnetic transitions of ε -Fe₇N₃ and γ '-Fe₄N

Both ϵ -Fe₇N₃ and γ '-Fe₄N adopt a ferromagnetic state at 1 bar with Curie temperatures of 400 K (Leineweber et al., 2001) and 750 K (Wriedt et al., 1987), respectively. Based on the XES observations described above, these compounds have fully reached a non-magnetic state by 43 and 34 GPa, respectively. Iron-light element compounds and alloys in Fe-P, Fe-C, Fe-S and other systems typically undergo a transition from ferromagnetic to paramagnetic state before the transition to a fully non-magnetic state (Chen et al., 2018a; Chen et al., 2014; Gu et al., 2016; Lin

et al., 2004a), so it can be inferred that an additional FM-PM transition may take place in Fe-N compounds below the completion of the spin transition. The only previous experimental investigation of pressure-induced magnetic transitions of iron nitrides was conducted by (Ishimatsu et al., 2003) on γ '-Fe₄N using XMCD, and showed the spin polarization was suppressed by pressure and finally vanished at 24 GPa. This loss of spin polarization was interpreted as a ferromagnetic to paramagnetic transition. This combined with our XES results indicates that paramagnetic γ '-Fe₄N has completely transitioned to the nonmagnetic state by 34 GPa. However, the pressure of any FM-PM transition in ϵ -Fe₇N₃ has not been directly observed by experiments, due to the lack of studies using Mössbauer spectroscopy or XMCD.

Indirect measurement of a FM-PM transition in Fe-N compounds through compression behavior has been inconclusive, and in iron-light element compounds more broadly, effects of FM-PM transitions on compressibility are either not observed or controversial. For example, the pressure of the FM-PM transition in Fe₃C was determined at ~8-10 GPa using Mössbauer spectroscopy, and no effect on the compression behavior was observed (Prescher et al., 2012); whereas Litasov et al. (2013) observed this transition at ~7-9 GPa by based on anomalous compression behavior of the a-axis, and proposed an elastic stiffening. Conditions of FM-PM transitions identified in previous work on ϵ -Fe₇N₃ and γ '-Fe₄N do not correspond to any significant changes in incompressibility.

In contrast, most Fe-light element compounds and alloys do exhibit stiffening after completing the transition to nonmagnetic state. Comparison between compression behavior and spin transition of ε -Fe₇N₃ reveals elastic stiffening associated with magnetic-nonmagnetic (i.e., high to low spin) transition at ~40 GPa. Similar behaviors have been observed and predicted in iron alloys, such as Fe-C, Fe-P, Fe-S systems (see section 4.2 for more discussion), which

consistently show that the PM-NM transition induces elastic stiffening, whereas elastic softening of Fe₇C₃ is due to Invar behavior (Chen et al., 2012; Chen et al., 2014; Mookherjee et al., 2011). γ '-Fe₄N is unique among the Fe-light element compounds and alloys discussed here: while the pressure of the PM-NM transition is constrained through complementary spectroscopic methods, it has no significant effect on compression behavior.

Ab initio calculations of magnetic states of Fe-N compounds have predicted magnetic transition pressures much higher than those observed in experiments. The transitions from magnetic to non-magnetic states of ε -Fe₃N_{1.25} and γ '-Fe₄N at 0 K were predicted to complete at 130 GPa and 250 GPa, respectively (Popov et al., 2015). Popov et al. (2015) also predicted significant volume collapse of iron nitrides due to the changes in the magnetic moment, which is in contrast to experimental observations, and not reported in previous *ab initio* calculations on iron carbides (Mookherjee et al., 2011; Vocadlo et al., 2002) although both studies used the generalized gradient approximation (GGA).

The difference in magneto-elastic coupling behavior between ε -Fe₇N₃ and γ '-Fe₄N may be attributed to the difference in strengths of Fe-N bonds associated with the crystal structures. In the idealized model of the crystal structure of ε -Fe₃N, the iron atoms are distributed according to hexagonal close packing (ε -Fe) and nitrogen atoms occupy one-third of octahedral voids between the iron layers in an ordered manner (Figure 4-9). However, nonstoichiometric ε -Fe₃N_x (0.75 < x < 1.4) exhibits a broad homogeneity range together with some entropy-driven transfer of nitrogen to further octahedral voids (Niewa et al., 2009a). Iron atoms in γ '-Fe₄N are distributed according to the cubic close packing (γ -Fe) and nitrogen atoms occupy one-fourth of octahedral voids (Figure 4-9). The resulting different 3*d* band structure affected by stronger 3*p*-3*d* hybridization of Fe and N in ε -Fe₇N₃ leads to a magnetic to nonmagnetic transition pressure of ε -Fe₇N₃ ~10 GPa higher

than that observed in γ '-Fe₄N (Figure 4-2). The difference in transition pressures may also be due to the relationship between anisotropic compressibility and the orientation of the magnetic moment relative to the crystal structure. For ε -Fe₇N₃, a collinear ferromagnetic arrangement of moments was determined to be parallel to the c-axis by neutron diffraction measurements (Robbins & White, 1964), and c-axis is more incompressible than a-axis (Shi et al., 2013) (c/a ratio increases with pressure, Figure 4-10); while for γ '-Fe₄N, magnetic arrangement of moments was proposed to be parallel to the a-axis (Costa-Krämer et al., 2004), which is the stiffest direction (Gressmann et al., 2007). To better understand the effect of spin transition on elastic anisotropy of both iron nitrides, further measurements on elastic constants up to spin transition pressures are necessary.

4.5.2 Magneto-elastic coupling in Fe-light element alloys/compounds

Previous studies have identified multiple candidate Fe alloys and light element compounds that can match the observed density and elastic properties of Earth's core (reviewed by Hirose et al., 2013; Li & Fei, 2014), and many of them undergo pressure-induced magnetic transitions with effects on elasticity (reviewed by Caracas, 2016). As a result, the extrapolation of density and velocity of ambient or low-pressure data to Earth's core conditions may be misleading, and experiments at higher pressures and temperatures are critical. However, the pressure of magnetic collapse and its coupling with elastic properties were inconsistent in previous results: for example, the pressure of PM to NM transition for Fe₃C from different studies spans a large range of 22 to 68 GPa (reviewed by Chen & Li, 2016). This inconsistency is partially caused by different criteria for magnetic transitions constrained using different methods.

The spin transition (or PM - NM transition) of ionic or covalent materials is usually accompanied by a change in interatomic distance due to a decrease in the size of the Fe atom,

which results in a volume collapse (Lin et al., 2013). In Fe alloys, the effect of the spin transition on structure and volume is subtle, leading to difficulties in detection. For direct comparison to this work on ε -Fe₇N₃ and γ '-Fe₄N, in which complementary methods determine the collapse of magnetic momentum and changes in compression behavior, we re-examine evidence for magnetic collapse and its effect on the compression behavior of other Fe-light element compounds Fe₃S, Fe₃P, Fe₇C₃, and Fe₃C, for which previous authors have obtained both XES measurements and dense *P-V* data coverage up to ~150 GPa.

Fe₃S remains in the tetragonal structure up to at least 200 GPa, with the completion of magnetic-nonmagnetic transition determined to occur at ~25 GPa by XES (Shen et al., 2003). A previous study argued that the magnetic transition did not affect the structure or compression behavior of Fe₃S (Kamada et al., 2014). However, a *g-G* plot (Figure 4-6a) of the compression measurements from (Chen et al., 2007; Kamada et al., 2014; Seagle et al., 2006) illustrates a discontinuity in compression behavior at ~67 GPa, which could have been induced by a magnetic collapse. The spin transition pressure may be underestimated by XES (Shen et al., 2003), due to the limitations of the spectral analysis method (no low spin reference applied) and the limited pressure range (up to 30 GPa) of the study.

Fe₃P is isostructural with the Fe₃S tetragonal phase at ambient conditions, and in-situ XRD patterns suggest no structural phase transition up to 111 GPa (Lai et al., 2020), although the structural evolution of Fe₃P upon compression remains controversial (Gu et al., 2014; Sagatov et al., 2020; Scott et al., 2007). The *g-G* plot based on the *P-V* measurements by (Lai et al., 2020) shows an increase in incompressibility at ~38 GPa (Figure 4-6b), which coincides with the pressure of magnetic spin momentum collapse determined by XES (Gu et al., 2016). Lai et al. (2020) propose the completion of magnetic-nonmagnetic transition occurred at 21 GPa based on the

disappearance of fast oscillation in Mössbauer spectra, which can be attributed to a ferromagnetic to paramagnetic transition.

Fe₇C₃ adopts a hexagonal structure from ~7-8 GPa to 167 GPa (Chen et al., 2012; Lord et al., 2009), and its magneto-elastic coupling effects have been thoroughly studied. By plotting the measurements from (Chen et al., 2012; Liu et al., 2016) as a *g*-*G* relation, an elastic stiffening occurs at 16 GPa and a softening occurs at 50 GPa (Figure 4-6c). These discontinuities in the compression behavior can be explained by a noncollinear to paramagnetic transition proposed by (Liu et al., 2016) and a magnetic collapse determined by XES (Chen et al., 2014), respectively.

Fe₃C, known as the mineral cohenite, has an orthorhombic structure with *Pnma* space group, and no structural change in Fe₃C was observed up to 187 GPa (Sata et al., 2010). The pressure of PM-NM (or high- to low-spin) transition in Fe₃C determined by XES has ranged widely from ~25 GPa by (Lin et al., 2004b) to ~50 GPa by (Chen et al., 2018a). The *g-G* plot of *P-V* measurements combined from (Li et al., 2002; Litasov et al., 2013; Ono & Mibe, 2010; Sata et al., 2010) indicates an elastic stiffening occurring at ~30 GPa (Figure 4-6d), which is consistent with the decreasing of the emission satellite peak intensity until 30 GPa observed by (Lin et al., 2004b). We thus interpret the discontinuity in compression behavior of Fe₃C at ~30 GPa is induced by the completion of the spin transition.

In summary, XES and g-G plots generally reveal the collapse of magnetic moment and effects on the compression behavior of Fe-light element alloys and compounds, which are candidate constituents of the Earth' core. A change in incompressibility induced by magnetic-nonmagnetic transitions may be common throughout Fe-light element compound systems, whereas the effects from FM-PM transition on compression are not significant for most compounds. To extrapolate physical properties to conditions of Earth's core, low

spin/nonmagnetic thermodynamic parameters should be used, and the effects of temperature should be considered. It has been shown that the pressure range for mixed-spin ferropericlase [(Mg_{0.75}Fe_{0.25})O] is broadened by 30 GPa as the temperature increases from 300 to 2000 K (Mao et al., 2011b). The thermal equations of state of Fe-light element alloys up to Earth's core conditions await further investigation.

4.5.3 Implications for iron alloys in Earth's and planetary cores

Our results suggest that although magnetic-to-nonmagnetic transitions do not produce sharp discontinuities in the compression behavior of Fe₇N₃, Fe₃S, Fe₃P, Fe₇C₃, and Fe₃C, their effect is non-negligible and additional tools, such as XES experiments and an analysis of *g-G* plots, are required to accurately determine the pressure range of the magnetic transitions. Consequently, the effect of magnetic transitions on the compression behavior of other light-element-bearing iron compounds may have been overlooked in previous experiments based only on an analysis of the pressure-volume data (e.g., Kamada et al., 2014). The effects of magnetic transitions should not be ignored when investigating the roles of iron alloys in Earth's and planetary cores under relevant conditions.

For example, distribution of iron isotopes in the Earth, which has been used to trace planetary differentiation processes, is dependent on isotope fractionation between various candidate host phases for iron in planetary cores and silicate melts under different pressure, temperature, composition, and oxygen fugacity conditions (Dauphas et al., 2017). Pressure effects on iron isotope fractionation determined by nuclear resonant inelastic X-ray scattering spectroscopy measurements have been different for different alloys, which is explained by differences in bond strength between combinations of iron with different alloying elements (Liu

et al., 2017; Shahar et al., 2016). Considering the effects of magnetic transitions on bond lengths and strengths of iron alloys presented in this study, magnetic transitions of iron alloys may impact the pressure dependence of the $^{57/54}$ Fe β factor (reduced partition function ratios) and thus the iron isotope fractionation over Earth's history.

The pressure conditions of the magnetic transitions in ε-Fe₇N₃, Fe₃S, Fe₃P, Fe₇C₃, and Fe₃C revealed by this study overlap with the moderate *P-T* range of the cores of relatively small planets, such as Mercury (~8 to 40 GPa, ~1700 to 2200 K) (Chen et al., 2008) and Mars (~24 to 42 GPa, ~2000 to 2600 K) (Fei & Bertka, 2005). Whether Mercury and Mars have fully molten cores (Margot et al., 2007; Yoder et al., 2003) or include solid inner cores (Genova et al., 2019; Stevenson, 2001) is under debate. In either case, planetary cooling may entail a present and/or past "snowing-core" scenario where iron-rich solids nucleate at the liquidus and sink or rise based on buoyancy. Minor solid iron alloys may thus significantly affect planetary core dynamics through powering magnetic dynamos (Breuer et al., 2015 and references therein). The effects of magnetic transition on physical properties [such as incompressibility and density (Figure 4-11)] of these candidate constituents of planetary cores may play an important role in deciphering the potential role of N, C, S, and P in these planetary cores.

4.6 Conclusions

In this work, we report spin/magnetic transitions and compressibility of ϵ -Fe₇N₃ and γ '-Fe₄N, the two stable iron nitrides at ambient conditions. Synchrotron XES and XRD measurements were carried out up to 60 GPa at 300 K using DAC. The completion of magnetic collapse in ϵ -Fe₇N₃ and γ '-Fe₄N is observed at 43 and 34 GPa, respectively, indicated by the completion of high-to low-spin state transition. Comparing spin transition and discontinuities in compression behavior

monitored by g-G plot, the completion of spin transition induces elastic stiffening in ε -Fe₇N₃ by 22% at ~40 GPa, but has no resolvable effect on the compression behavior of γ '-Fe₄N. Accordingly, fitting P-V data to BM3-EoS yields: $V_0 = 86.55 \pm 0.02$ (ų), $K_0 = 160 \pm 2$ GPa, and K_0 ' = 4.3 \pm 0.2 for magnetic, mixed spin ε -Fe₇N₃; $V_0 = 83.29 \pm 0.03$ (ų), $K_0 = 232 \pm 9$ GPa, and K_0 ' = 4.1 \pm 0.5 for nonmagnetic, low spin ε -Fe₇N₃; $V_0 = 54.82 \pm 0.02$ (ų), $K_0 = 152 \pm 2$ GPa, and K_0 ' = 4.0 \pm 0.1 for γ '-Fe₄N within the investigated pressure range.

Using the same protocol, we re-examine evidence for magnetic collapse and its effect on the compression behavior of other Fe-light element compounds as candidate components of terrestrial planet's core, Fe₃S, Fe₃P, Fe₇C₃, and Fe₃C. We summarize previous reported dense *P-V* data up to ~150 GPa and comparing with XES measurements, which indicate the completion of the magnetic transition in Fe₃S, Fe₃P, and Fe₇C₃ is at about 67, 38, 50, and 30 GPa, respectively. The completion of the magnetic transition of Fe₃S and Fe₃P induces elastic stiffening, whereas that of Fe₇C₃ induces elastic softening. The changes of incompressibility induced by magnetic-nonmagnetic transition may have potential implications in deciphering the role of iron-light element alloys in Earth's and planetary cores.

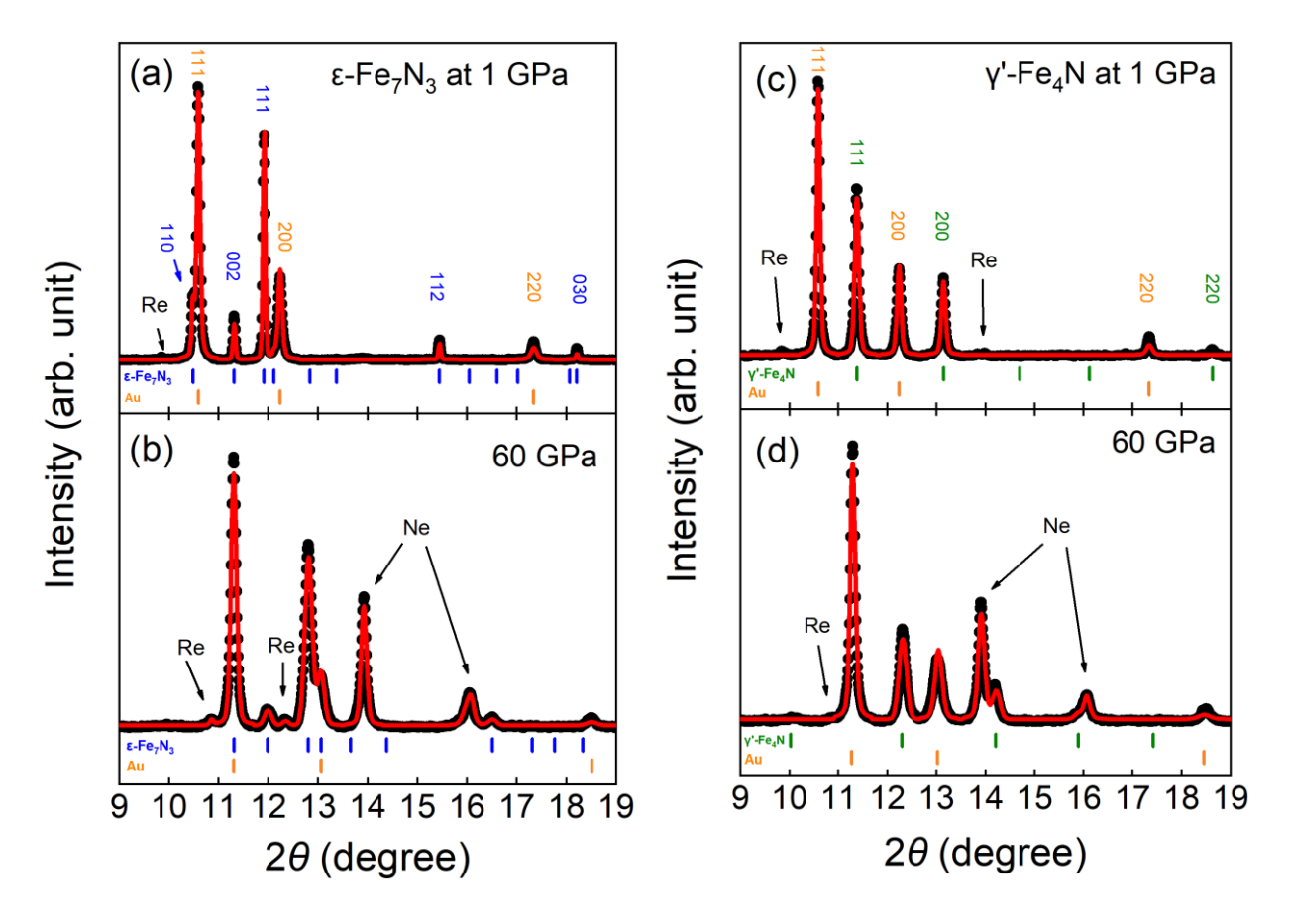


Figure 4-1: (a) and (b) are representative X-ray diffraction patterns of ε -Fe₇N₃ at 1 and 60 GPa at 300 K, respectively; (c) and (d) are representative X-ray diffraction patterns of γ '-Fe₄N at 1 and 60 GPa at 300 K, respectively. Le Bail refinements (red solid curves) of observed XRD data (black dots) were carried out after background subtraction, demonstrating all sample peaks match hexagonal ε -Fe₇N₃ and cubic γ '-Fe₄N, respectively, within the investigated pressure range. The vertical ticks are ε -Fe₇N₃ (blue), γ '-Fe₄N (dark green), and the pressure calibrant, Au (orange). The wavelength of the incident X-ray beam was 0.434 Å.

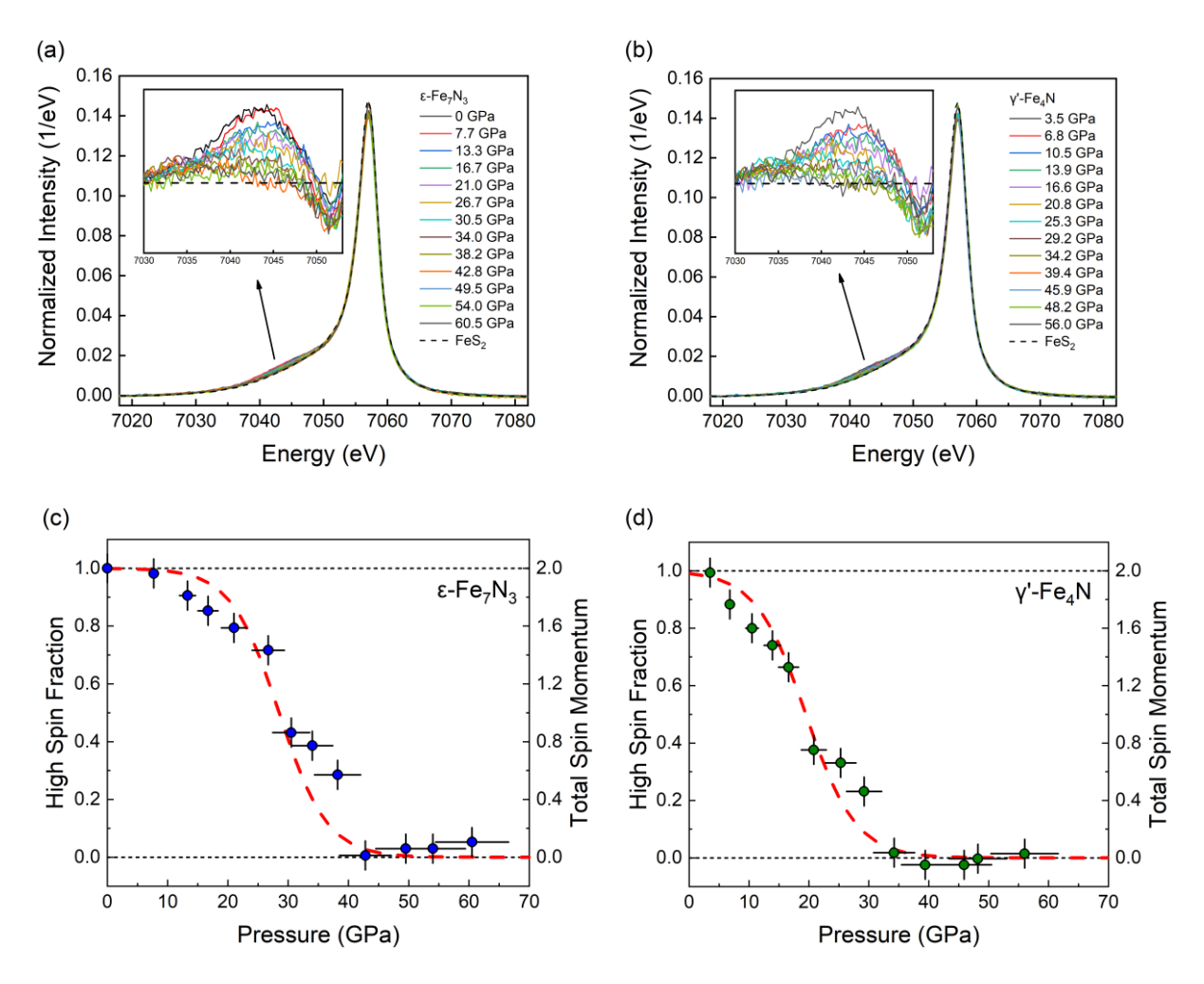


Figure 4-2: (a-b) Fe- K_{β} fluorescence spectra of ε -Fe₇N₃ and γ '-Fe₄N up to 60.5 GPa at 300 K. The XES spectra were normalized to unity in integrated intensity. The top-left inset shows intensity difference of observed satellite emission peak (K_{β} ') between 7030 and 7053 eV relative to the low-spin reference FeS₂ at 0 GPa (black dashed line). (c-d) High-spin fraction of Fe in ε -Fe₇N₃ and γ '-Fe₄N as a function of pressure derived from the XES measurements following integrated relative difference method (Mao et al., 2014). Completion of the spin transition of ε -Fe₇N₃ is at ~40 GPa, and for γ '-Fe₄N at ~30 GPa. The dashed line is fitted by Boltzmann function, and error bars determined by comparing results using FeS₂ vs. sample at 60 GPa as low-spin references. Pressures were determined by ruby fluorescence (Mao et al., 1986) before

and after each XES collection, which differed by up to 10% due to relaxation of the sample or cell assembly.

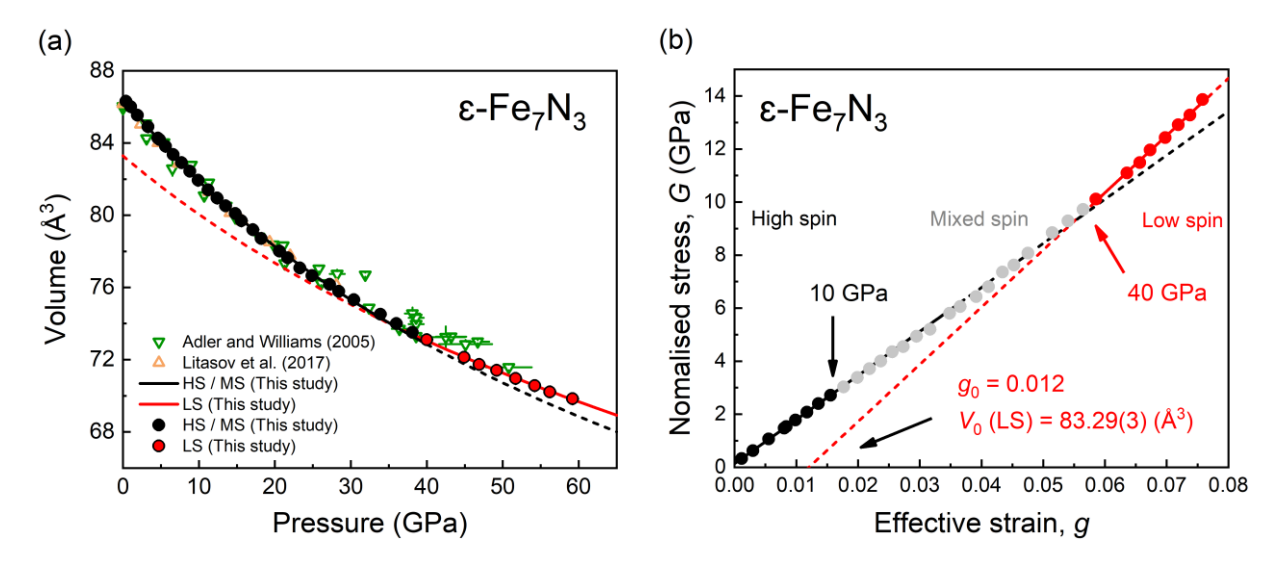


Figure 4-3: Compression behavior of ε -Fe₇N₃ at 300 K. (a) Unit-cell volume of ε -Fe₇N₃ up to 60 GPa at 300 K determined from X-ray diffraction measurements in this work (solid circles), together with previous experimental results. The black and red curves represent the 3rd-order Birch-Murnaghan equation of state (BM3-EoS) fits for the data for high spin (HS) and mixed spin (MS) / magnetic state (1 bar-40 GPa), low spin (LS) / nonmagnetic state (40-60 GPa), respectively. (b) Normalized stress G as a function of effective strain g. Solid black, gray, and red circles represent the results of high spin, mixed spin, and low spin state, respectively, as determined by XES. Black and red lines indicate fits of the high spin and low spin state G(g) data, respectively. The V_0 for the nonmagnetic state is obtained by extrapolating g to g_0 .

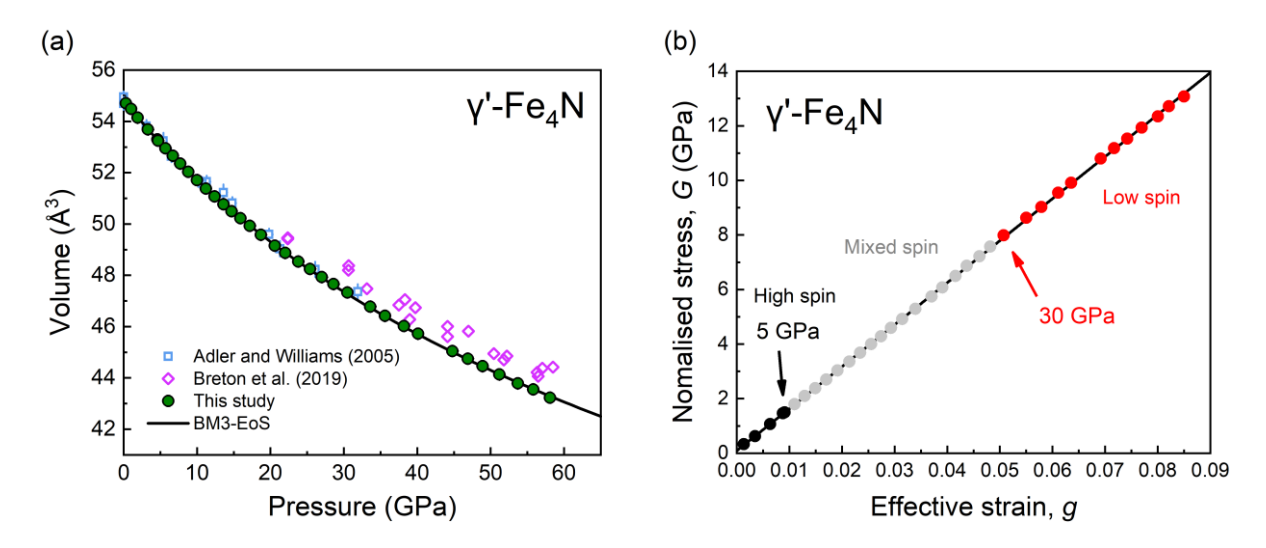


Figure 4-4: Compression behavior of γ '-Fe₄N at 300 K. (a) Unit-cell volume of γ '-Fe₄N up to 60 GPa at 300 K determined from X-ray diffraction measurements in this work (dark green circles), together with previous experimental results. The black curve represents the 3rd-order Birch-Murnaghan equation of state (BM-EoS) fit of all pressure-volume data from this study. (b) Normalized stress G as a function of effective strain g. Solid black, gray, and red circles represent the results of high spin, mixed spin, and low spin state, respectively, as determined by XES. The black solid line indicates a linear fit for all data. The pressure of onset and completion of spin transition is indicated by XES, but no change in compressibility can be observed in either plot.

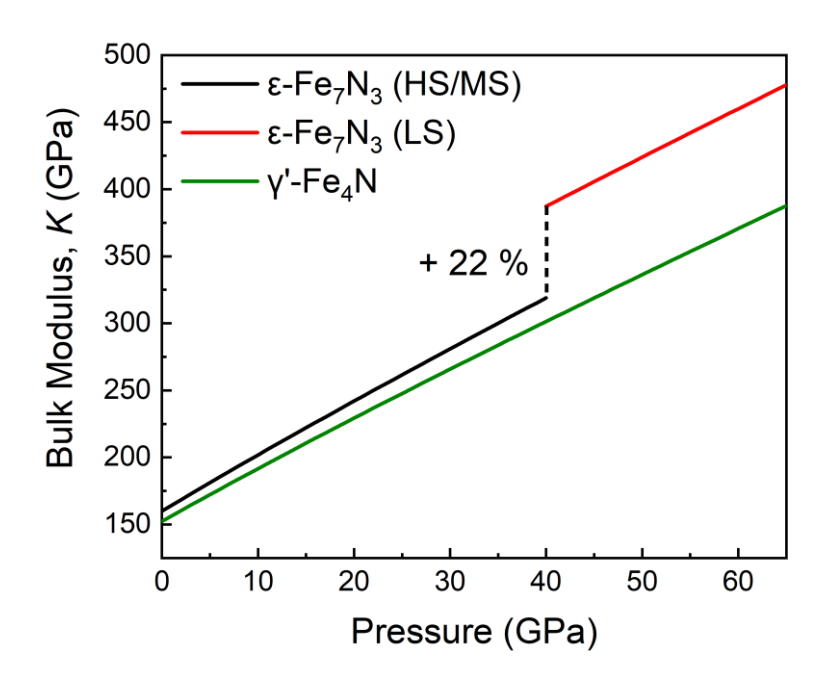


Figure 4-5: Isothermal bulk modulus (K) of high spin and mixed spin (magnetic) state ϵ -Fe₇N₃ (black curve), low spin (nonmagnetic) state ϵ -Fe₇N₃ (red curve), and γ '-Fe₄N (dark green curve) at 300 K as a function of pressure, calculated from the fitted BM-EOS parameters (Table 4-1). The magnetic to nonmagnetic transition of ϵ -Fe₇N₃ induces +22% increase in incompressibility at 40 GPa.

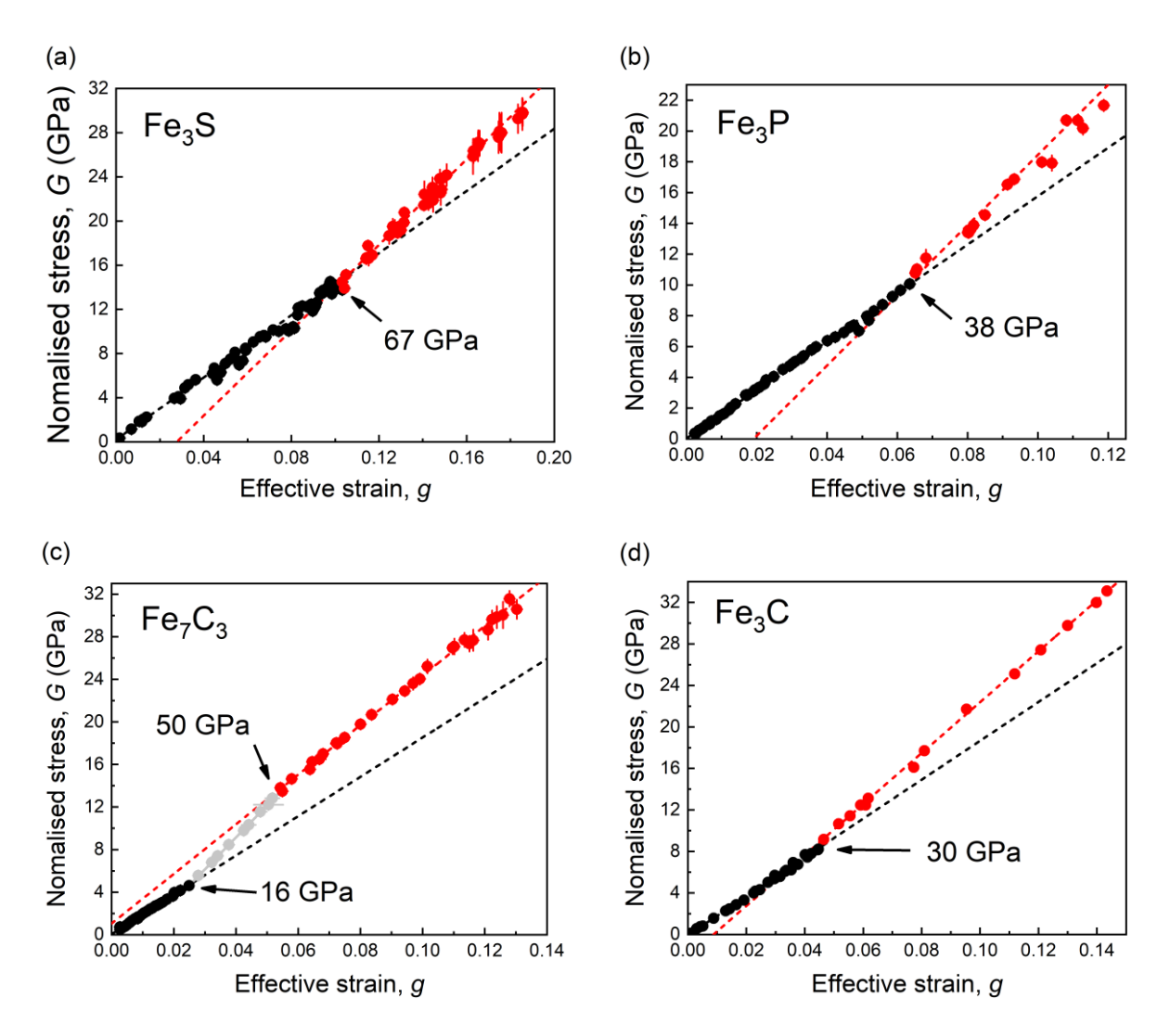


Figure 4-6: Normalized stress G as a function of effective strain g for (a) Fe₃S (Chen et al., 2007; Kamada et al., 2014; Seagle et al., 2006), (b) Fe₃P (Lai et al., 2020), (c) Fe₇C₃ (Chen et al., 2012; Liu et al., 2016), and (d) Fe₃C (Li et al., 2002; Litasov et al., 2013; Ono & Mibe, 2010; Sata et al., 2010). Dashed lines are linear fits to g-G, and the discontinuity in compression behavior corresponds to the change of slope of the linearized g-G plot.

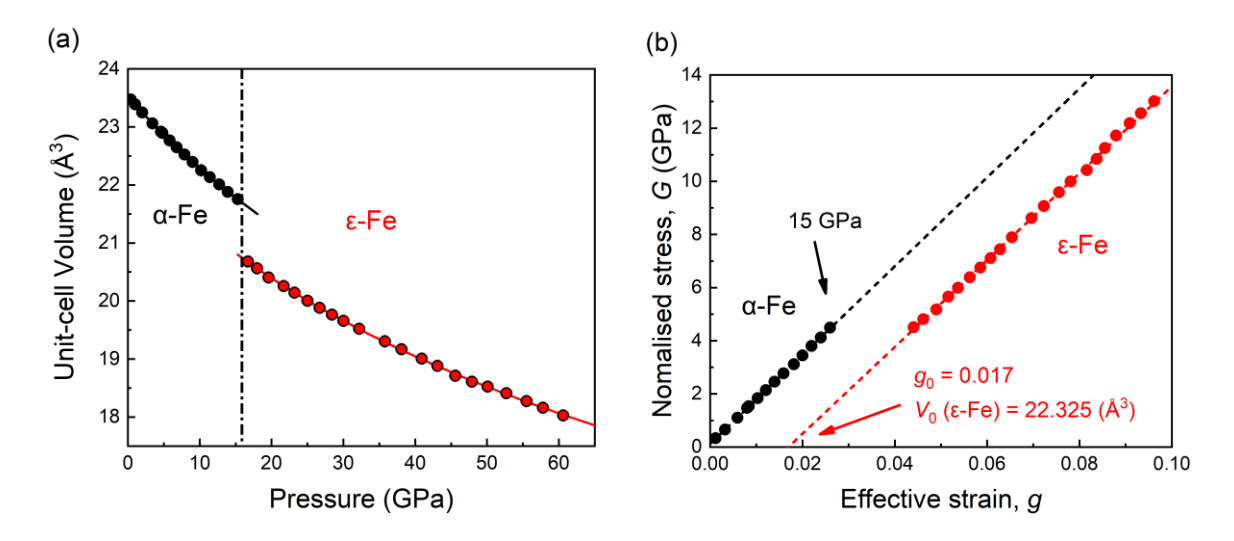


Figure 4-7: Compression behavior of pure Fe at 300 K. (a) Unit-cell volume of α -Fe (black circles) and ϵ -Fe (red circles) up to 60 GPa at 300 K determined from X-ray diffraction measurements. The solid black curves and solid red curves represent the 3rd-order Birch-Murnaghan equation of state (BM-EoS) fits for the data for α -Fe (1-15 GPa) and ϵ -Fe (15-60 GPa), respectively. (b) Normalized stress G as a function of effective strain g. Solid black and red circles represent the results of α -Fe and ϵ -Fe, respectively. The black and red lines indicate linear fits for α -Fe and ϵ -Fe, respectively. The V_0 for the ϵ -Fe is obtained by extrapolating g to g_0 .

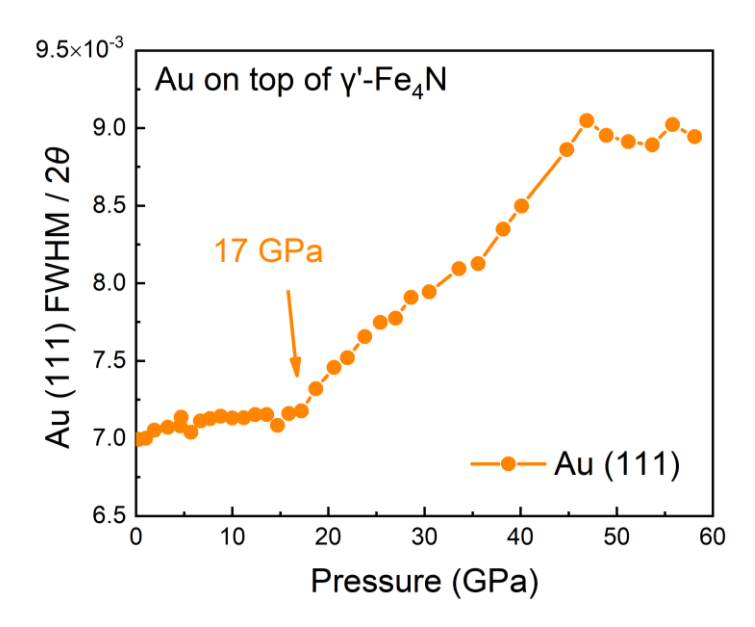


Figure 4-8: Full width at half maximum (FWHM) for Au (111) normalized to 2θ . Orange circles are data obtained from Au at position of γ '-Fe₄N sample in the diamond anvil cell. The peak broadening induced by the onset of nonhydrostaticity of Ne medium (Klotz et al., 2009) in this study starts at ~17 GPa. The magnitude of peak broadening remains small above this pressure, consistent with quasi-hydrostatic conditions in the sample chamber.

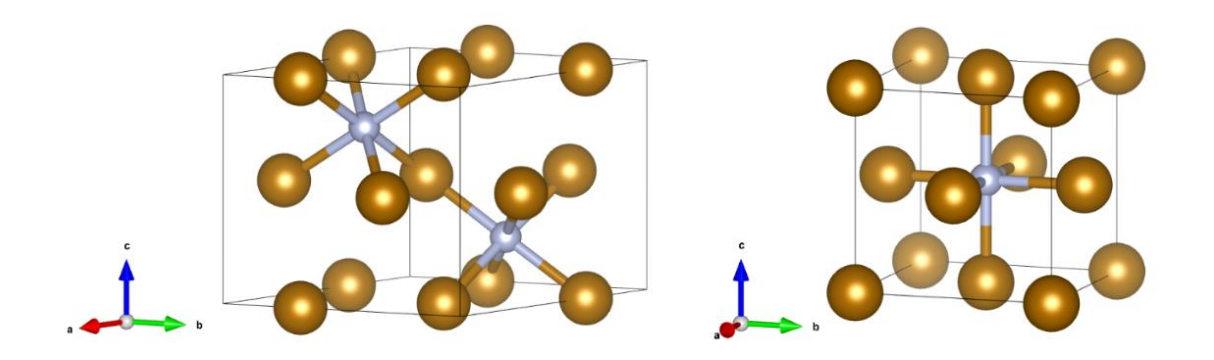


Figure 4-9: Crystal structure of ϵ -Fe₇N₃ (left) and γ '-Fe₄N (right) at ambient conditions. Gray spheres in polyhedra represent the N atoms and brown spheres represent Fe atoms.

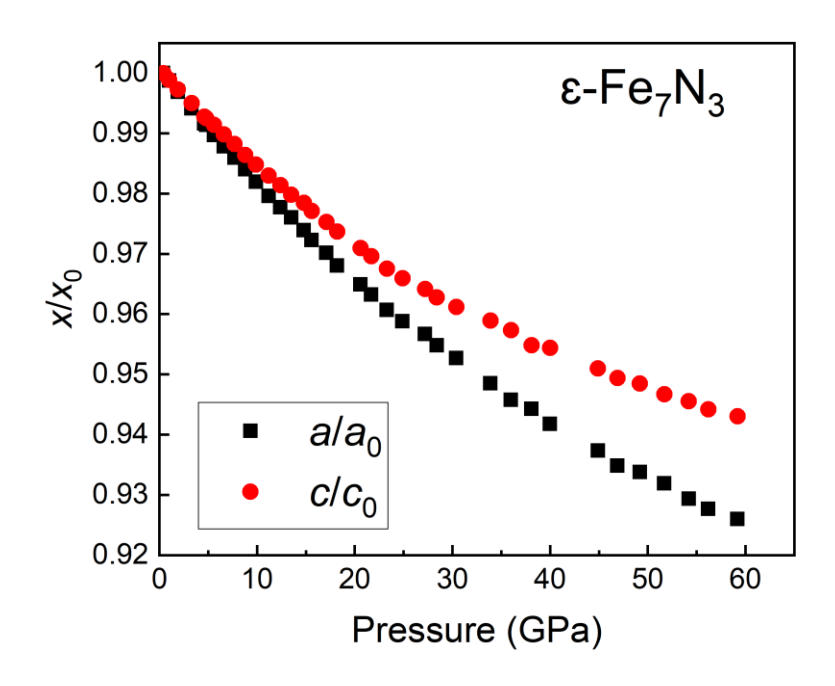


Figure 4-10: Axial compressibility of ϵ -Fe₇N₃ at 300 K.

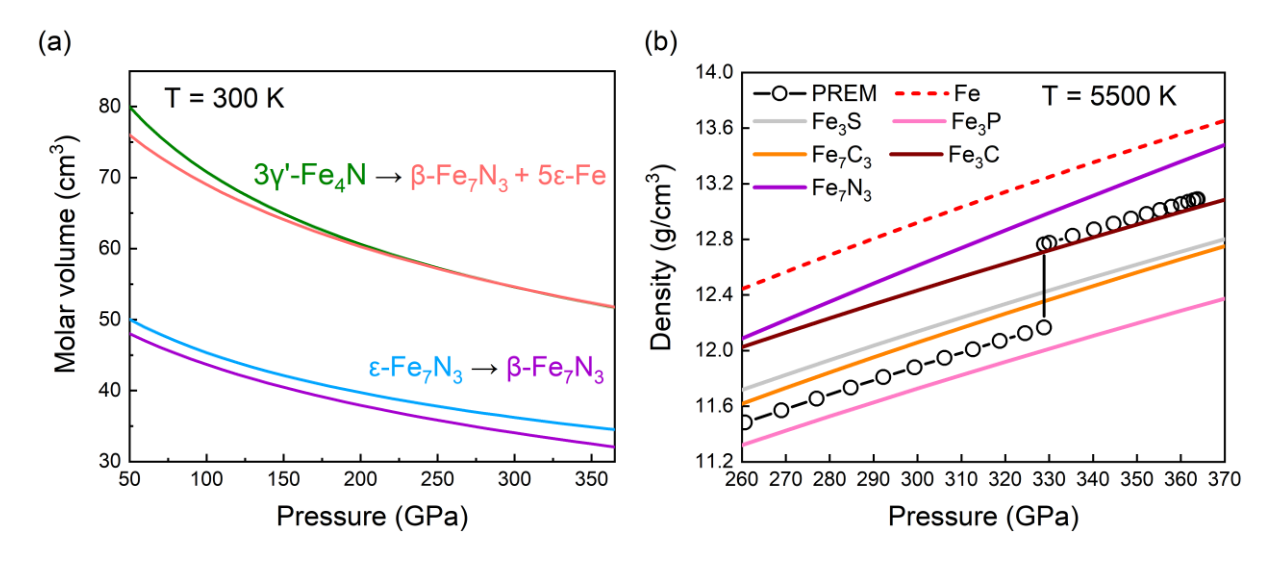


Figure 4-11: (a) Molar volumes of nonmagnetic ε -Fe₇N₃ (light blue), β -Fe₇N₃ (purple), $3\gamma'$ -Fe₄N (green) and its isochemical assemblage of β -Fe₇N₃ + 5ε -Fe (light red) as a function of pressure at 300 K. The calculation is based on BM3 EoS with parameters of relevant phases summarized in Table 1 and 2. (b) Isothermal density profiles of nonmagnetic β -Fe₇N₃ (purple), Fe₇C₃ (orange), Fe₃C (brown), Fe₃S (gray), Fe₃P (pink) along a 5500 K isotherm. For comparison, a density profile of pure ε -Fe and seismologically constrained density profile (Preliminary Reference Earth Model, Dziewonski & Anderson, 1981) are also plotted. The calculation is based on Mie-Grüneisen-Debye equation of state with parameters of relevant phases listed in Table 4-5.

Table 4-1: Equation of state parameters of ϵ -Fe₇N₃ and γ '-Fe₄N.

| Phase | Magnetism | P (GPa) | V_0 (Å ³) | <i>K</i> ₀ | <i>K</i> ₀ ' | Method | Reference |
|---|------------------------|---------|-------------------------|-----------------------|-------------------------|----------------------|---------------------------|
| ε-Fe ₇ N ₃ | Magnetic (mixed spin) | 0-40 | 86.55(2) ^a | 160(2) | 4.3(2) | DAC ^c | This study |
| ϵ -Fe ₇ N ₃ | Nonmagnetic (low spin) | 40-60 | 83.29(3) | 232(9) | 4.1(5) | DAC | This study |
| ϵ -Fe ₇ N ₃ | - | 0-51 | 86.04(10) | 168(10) | 5.7(2) | DAC | Adler and Williams (2005) |
| $\epsilon\text{-Fe}_3N_{1.26}$ | - | 0-31 | 86.18(3) | 163(2) | 5.3(2) | MA^d | Litasov et al. (2017) |
| ϵ -Fe ₃ N _{1.25} | Magnetic (mixed spin) | 0-100 | 81.35 | 224(1) | 4.30(5) | DFT-GGA ^e | Popov et al. (2015) |
| ϵ -Fe ₃ N _{1.25} | Nonmagnetic | 0-500 | 77.44 | 303(1) | 4.38(1) | DFT-GGA | Popov et al. (2015) |
| γ'-Fe ₄ N | - | 0-60 | 54.82(2) | 152(2) | 4.0(1) | DAC | This study |
| γ '-Fe ₄ N | - | 0-31 | 54.95(22) | 155(3) | 4 ^b | DAC | Adler and Williams (2005) |
| γ'-Fe ₄ N | - | 0-33 | 54.81 | 154(3) | 5.3(1) | DAC | Guo et al. (2013) |
| γ'-Fe ₄ N | - | 22-60 | 54.95 ^b | 169(6) | 4.1(4) | DAC | Breton et al. (2019) |
| γ'-Fe ₄ N | - | - | - | 166(1) | 4.2(1) | DFT-GGA | Niewa et al. (2009) |
| γ '-Fe ₄ N | Magnetic | - | 54.64 | 192(1) | - | FP-TEC ^f | Gressmann et al. (2007) |
| γ '-Fe ₄ N | Magnetic (mixed spin) | 0-200 | 54.10 | 152(4) | 5.41(17) | DFT-GGA | Popov et al. (2015) |
| γ'-Fe ₄ N | Nonmagnetic | 0-500 | 49.25 | 285(3) | 4.38(1) | DFT-GGA | Popov et al. (2015) |

^a Numbers in parentheses are uncertainties on the last digits. ^b Fixed value

^c Diamond anvil cell

d Multi-anvil press
e Density functional theory -generalized gradient approximation
f First-principles total-energy calculations

Table 4-2: Volume and unit-cell parameters of ε -Fe₇N₃ at 300 K. The uncertainties of pressures were propagated from uncertainties of unit cell volumes of Au and Ne, and uncertainties of their equation of state parameters (Fei et al., 2007), respectively.

| | | 77 (9 3) | γ γ γ | 2 |
|-------------|-------------|---------------------|----------|----------|
| P (Au, GPa) | P (Ne, GPa) | $V(\mathring{A}^3)$ | a (Å) | c (Å) |
| 0.4(1) | - | 86.31(2) | 4.756(1) | 4.407(1) |
| 1.0(1) | - | 86.01(2) | 4.750(1) | 4.402(1) |
| 1.9(1) | - | 85.54(2) | 4.741(1) | 4.395(1) |
| 3.3(1) | - | 84.90(2) | 4.728(1) | 4.385(1) |
| 4.6(1) | - | 84.27(3) | 4.716(1) | 4.375(1) |
| 4.8(1) | - | 84.19(4) | 4.715(1) | 4.374(1) |
| 5.6(1) | - | 83.82(4) | 4.707(1) | 4.369(1) |
| 6.6(1) | - | 83.36(2) | 4.698(1) | 4.362(1) |
| 7.7(1) | - | 82.91(5) | 4.689(1) | 4.355(1) |
| 8.8(1) | - | 82.44(5) | 4.680(1) | 4.347(1) |
| 9.9(1) | - | 81.93(7) | 4.670(1) | 4.340(1) |
| 11.2(1) | - | 81.41(7) | 4.659(1) | 4.332(1) |
| 12.4(1) | - | 80.95(7) | 4.650(1) | 4.325(1) |
| 13.5(1) | - | 80.52(7) | 4.642(2) | 4.318(1) |
| 14.8(1) | - | 80.09(7) | 4.632(1) | 4.312(1) |
| 15.6(1) | - | 79.69(6) | 4.624(1) | 4.306(1) |
| 17.1(1) | - | 79.20(9) | 4.614(2) | 4.298(1) |
| 18.2(1) | 19.2(2) | 78.72(8) | 4.604(1) | 4.291(1) |
| 20.6(1) | 21.4(2) | 78.02(2) | 4.589(1) | 4.279(1) |
| 21.7(2) | 22.8(3) | 77.64(4) | 4.581(1) | 4.273(1) |
| 23.3(2) | 24.7(3) | 77.09(4) | 4.569(1) | 4.264(1) |
| 24.9(2) | 26.3(3) | 76.66(3) | 4.560(1) | 4.257(1) |
| 27.2(2) | 28.2(3) | 76.18(2) | 4.550(1) | 4.249(1) |
| 28.4(2) | 29.7(3) | 75.79(1) | 4.541(1) | 4.243(1) |
| 30.4(3) | 31.8(4) | 75.32(2) | 4.531(1) | 4.236(1) |
| 33.9(3) | 35.3(4) | 74.52(9) | 4.511(2) | 4.226(1) |
| 35.8(3) | 37.5(4) | 74.00(4) | 4.498(1) | 4.219(1) |
| 38.1(3) | 40.1(5) | 73.51(1) | 4.491(1) | 4.208(1) |
| 40.0(4) | 41.5(5) | 73.11(3) | 4.479(1) | 4.206(1) |
| 44.9(4) | 45.6(5) | 72.13(5) | 4.458(1) | 4.191(1) |
| 46.9(4) | 48.0(5) | 71.73(3) | 4.446(1) | 4.184(1) |
| 49.2(5) | 49.9(6) | 71.41(4) | 4.441(1) | 4.180(1) |
| 51.6(5) | 52.7(6) | 70.95(7) | 4.432(1) | 4.172(1) |
| 54.1(5) | 55.4(6) | 70.56(7) | 4.420(1) | 4.167(1) |
| 56.2(5) | 57.6(7) | 70.22(9) | 4.412(2) | 4.161(1) |
| 58.2(5) | 60.1(7) | 69.84(1) | 4.404(1) | 4.156(1) |

Numbers in parentheses are uncertainties on the last digits.

Table 4-3: Volume and unit-cell parameters of γ '-Fe₄N at 300 K. The uncertainties of pressures were propagated from uncertainties of unit cell volumes of Au and Ne, and uncertainties of their equation of state parameters (Fei et al., 2007), respectively.

| P (Au, GPa) | P (Ne, GPa) | $V(\mathring{A}^3)$ | a (Å) |
|-------------|-------------|---------------------|----------|
| 0.3(1) | - | 54.71(1) | 3.796(1) |
| 1.0(1) | - | 54.49(1) | 3.791(1) |
| 1.9(1) | - | 54.14(1) | 3.783(1) |
| 3.3(1) | - | 53.69(1) | 3.773(1) |
| 4.6(1) | - | 53.30(1) | 3.763(1) |
| 4.7(1) | - | 53.25(1) | 3.762(1) |
| 5.7(1) | - | 52.95(1) | 3.755(1) |
| 6.7(1) | - | 52.66(1) | 3.748(1) |
| 7.7(1) | - | 52.35(1) | 3.741(1) |
| 8.8(1) | - | 52.03(1) | 3.733(1) |
| 10.0(1) | - | 51.71(2) | 3.725(1) |
| 11.2(1) | - | 51.38(3) | 3.717(1) |
| 12.4(1) | - | 51.08(4) | 3.710(1) |
| 13.6(1) | - | 50.77(2) | 3.702(1) |
| 14.7(1) | - | 50.50(6) | 3.695(1) |
| 15.9(1) | - | 50.23(6) | 3.689(1) |
| 17.2(2) | - | 49.93(6) | 3.681(1) |
| 18.7(2) | 19.3(2) | 49.58(6) | 3.672(1) |
| 20.6(2) | 21.3(2) | 49.15(7) | 3.662(1) |
| 22.0(2) | 22.8(3) | 48.87(8) | 3.655(1) |
| 23.8(2) | 24.6(3) | 48.54(8) | 3.646(1) |
| 25.4(2) | 26.2(3) | 48.25(9) | 3.639(1) |
| 27.0(2) | 28.0(3) | 47.93(8) | 3.631(1) |
| 28.6(2) | 29.6(3) | 47.66(8) | 3.624(1) |
| 30.5(2) | 31.5(4) | 47.33(7) | 3.615(1) |
| 33.6(2) | 34.8(4) | 46.78(8) | 3.602(1) |
| 35.6(2) | 36.9(4) | 46.42(8) | 3.594(1) |
| 38.2(3) | 39.6(4) | 46.02(8) | 3.584(1) |
| 40.1(3) | 41.6(5) | 45.72(8) | 3.576(1) |
| 44.8(3) | 46.2(5) | 45.05(7) | 3.558(1) |
| 46.9(3) | 48.3(5) | 44.75(8) | 3.550(1) |
| 48.9(3) | 50.3(6) | 44.46(8) | 3.542(1) |
| 51.2(3) | 52.6(6) | 44.13(8) | 3.530(1) |
| 53.7(4) | 55.1(6) | 43.79(8) | 3.521(1) |
| 55.8(4) | 57.2(7) | 43.50(7) | 3.514(1) |
| 58.1(4) | 59.6(7) | 43.23(8) | 3.506(1) |

Numbers in parentheses are uncertainties on the last digits.

Table 4-4: Volume and unit-cell parameters of Fe at 300 K. The uncertainties of pressures were propagated from uncertainties of unit cell volumes of Au and Ne, and uncertainties of their equation of state parameters (Fei et al., 2007), respectively.

| P (GPa) | $V(\mathring{A}^3)$ | a (Å) | c (Å) |
|----------------------|---------------------|----------|----------|
| $0.4(1)^{a}$ | 23.47(4) | 2.863(1) | _ |
| $1.0(1)^{a}$ | 23.39(4) | 2.860(1) | - |
| $2.0(1)^{a}$ | 23.25(4) | 2.854(1) | - |
| $3.4(2)^{a}$ | 23.06(4) | 2.846(1) | - |
| $4.6(2)^1$ | 22.92(3) | 2.841(1) | - |
| $4.8(2)^{a}$ | 22.90(4) | 2.840(1) | - |
| $5.8(2)^{a}$ | 22.77(4) | 2.834(1) | - |
| $6.8(2)^{a}$ | 22.65(3) | 2.829(1) | - |
| $7.9(2)^{a}$ | 22.52(3) | 2.824(1) | - |
| $9.0(2)^{a}$ | 22.40(3) | 2.819(1) | - |
| $10.2(2)^{a}$ | 22.25(5) | 2.813(1) | - |
| $11.4(2)^{a}$ | 22.13(3) | 2.808(1) | - |
| $12.7(2)^{a}$ | 22.01(3) | 2.802(1) | - |
| $13.9(2)^{a}$ | 21.88(3) | 2.797(1) | - |
| $15.3(2)^{a}$ | 21.76(3) | 2.792(1) | - |
| $16.7(2)^{b}$ | 20.68(4) | 2.460(1) | 3.945(1) |
| $18.0(2)^{b}$ | 20.56(4) | 2.454(1) | 3.943(1) |
| $19.6(3)^{b}$ | 20.40(4) | 2.449(1) | 3.927(1) |
| $21.7(3)^{b}$ | 20.26(4) | 2.442(1) | 3.922(1) |
| $23.2(3)^{b}$ | 20.14(3) | 2.438(1) | 3.913(1) |
| $25.0(3)^{b}$ | 20.00(4) | 2.432(1) | 3.904(1) |
| $26.7(3)^{b}$ | 19.88(4) | 2.428(1) | 3.895(1) |
| $28.4(3)^{b}$ | 19.76(4) | 2.423(1) | 3.887(1) |
| $30.0(3)^{b}$ | 19.66(3) | 2.419(1) | 3.879(1) |
| $32.2(3)^{b}$ | 19.52(3) | 2.413(1) | 3.870(1) |
| $35.8(4)^{b}$ | 19.31(5) | 2.405(1) | 3.855(1) |
| 38.1(4) ^b | 19.17(3) | 2.399(1) | 3.846(1) |
| $40.9(4)^{b}$ | 19.01(3) | 2.392(1) | 3.836(1) |
| $43.1(4)^{b}$ | 18.88(3) | 2.387(1) | 3.828(1) |
| $45.6(4)^{b}$ | 18.71(3) | 2.380(1) | 3.814(1) |
| $47.9(5)^{b}$ | 18.61(4) | 2.376(1) | 3.806(1) |
| $50.1(5)^{b}$ | 18.52(4) | 2.373(1) | 3.799(1) |
| $52.7(5)^2$ | 18.41(3) | 2.368(1) | 3.791(1) |
| 55.5(5) ^b | 18.27(4) | 2.362(1) | 3.783(1) |
| 57.8(5) ^b | 18.16(4) | 2.357(1) | 3.776(1) |
| 60.6(6) ^b | 18.03(4) | 2.351(1) | 3.768(1) |

^a α-Fe

^b ε-Fe Numbers in parentheses are uncertainties on the last digits. Table 4-5: Mie-Grüneisen-Debye equation of state parameters of nonmagnetic iron alloys and pure iron.

| Phase | P (GPa) | V_0 (Å ³) | K ₀ (GPa) | K_0 ' | $\theta_0(\mathbf{K})$ | γο | \overline{q} |
|---|----------|-------------------------|----------------------|----------|------------------------|---------------|----------------|
| β-Fe ₇ N ₃ ^a | _ | 181.4(5) ^c | 316(5) | 3.2 | 430 | 2.1(3) | 4.5(9) |
| Fe ₃ S | 67-197 | 348.2(32) | 224(5) | 4.2(2) | 417^{d} | $1.01(3)^{d}$ | 1^{d} |
| Fe ₃ P | 38-110 | 350.2(17) | 260(5) | 4.0(2) | 417^{d} | $1.01(3)^{d}$ | 1^{d} |
| Fe ₇ C ₃ | 50-167 | 188.7(11) | 223(2) | 4.1(1) | 920(140) ^e | $2.57(5)^{e}$ | $2.2(5)^{e}$ |
| Fe ₃ C | 30-186.6 | 151.24(25) | 264(3) | 4.0(1) | $490(120)^{f}$ | $2.09(4)^{f}$ | $-0.1(3)^{f}$ |
| ε-Fe ^b | - | 22.14(19) | 185(2) | 4.94(12) | 1173(62) | 3.2(2) | 0.8(3) |

^a Data from (Kusakabe et al., 2019)

but from (Rusakube et al., 2019)

b Data from (Sakai et al., 2014)

c Numbers in parentheses are uncertainties on the last digits.

d Data from (Thompson et al., 2020)

e Data from (Nakajima et al., 2011)

f Data from (Litasov et al., 2013)

BIBLIOGRAPHY

BIBLIOGRAPHY

- Adler, J. F., & Williams, Q. (2005). A high-pressure X-ray diffraction study of iron nitrides: Implications for Earth's core. *Journal of Geophysical Research-Solid Earth*, 110(B1). http://10.1029/2004jb003103
- Akahama, Y., & Kawamura, H. (2006). Pressure calibration of diamond anvil Raman gauge to 310GPa. *Journal of Applied Physics*, 100(4), 043516. http://10.1063/1.2335683
- Albarede, F. (2009). Volatile accretion history of the terrestrial planets and dynamic implications. *Nature*, *461*(7268), 1227-1233. http://10.1038/nature08477
- Alt, J. C., & Teagle, D. A. H. (1999). The uptake of carbon during alteration of ocean crust. *Geochimica et Cosmochimica Acta*, 63(10), 1527-1535. http://10.1016/S0016-7037(99)00123-4
- Amsellem, E., Moynier, F., Bertrand, H., Bouyon, A., Mata, J., Tappe, S., & Day, J. M. D. (2020). Calcium isotopic evidence for the mantle sources of carbonatites. *Sci Adv*, 6(23), eaba3269. http://10.1126/sciadv.aba3269
- Angel, R. J. (2000). Equations of state. *High-Temperature and High-Pressure Crystal Chemistry*, 41(1), 35-59. http://10.2138/rmg.2000.41.2
- Badro, J. (2014). Spin Transitions in Mantle Minerals. *Annual Review of Earth and Planetary Sciences*, Vol 42, 42(1), 231-248. http://10.1146/annurev-earth-042711-105304
- Badro, J., Fiquet, G., Guyot, F., Rueff, J. P., Struzhkin, V. V., Vanko, G., & Monaco, G. (2003). Iron partitioning in Earth's mantle: toward a deep lower mantle discontinuity. *Science*, 300(5620), 789-791. http://10.1126/science.1081311
- Badro, J., Fiquet, G., Struzhkin, V. V., Somayazulu, M., Mao, H. K., Shen, G., & Le Bihan, T. (2002). Nature of the high-pressure transition in Fe₂O₃ hematite. *Physical Review Letters*, 89(20), 205504. http://10.1103/PhysRevLett.89.205504
- Badro, J., Rueff, J. P., Vanko, G., Monaco, G., Fiquet, G., & Guyot, F. (2004). Electronic transitions in perovskite: possible nonconvecting layers in the lower mantle. *Science*, 305(5682), 383-386. http://10.1126/science.1098840
- Bayarjargal, L., Fruhner, C. J., Schrodt, N., & Winkler, B. (2018). CaCO₃ phase diagram studied with Raman spectroscopy at pressures up to 50 GPa and high temperatures and DFT modeling. *Physics of the Earth and Planetary Interiors*, 281, 31-45. http://10.1016/j.pepi.2018.05.002
- Bergin, E. A., Blake, G. A., Ciesla, F., Hirschmann, M. M., & Li, J. (2015). Tracing the ingredients for a habitable earth from interstellar space through planet formation. *Proceedings of the National Academy of Sciences of the United States of America*, 112(29), 8965-8970. http://10.1073/pnas.1500954112

- Biellmann, C., Gillet, P., Peyronneau, J., & Reynard, B. (1993). Experimental evidence for carbonate stability in the Earth's lower mantle. *Earth and Planetary Science Letters*, 118(1-4), 31-41.
- Binck, J., Bayarjargal, L., Lobanov, S. S., Morgenroth, W., Luchitskaia, R., Pickard, C. J., et al. (2020). Phase stabilities of MgCO₃ and MgCO₃-II studied by Raman spectroscopy, X-ray diffraction, and density functional theory calculations. *Physical Review Materials*, 4(5). http://10.1103/PhysRevMaterials.4.055001
- Birch, F. (1952). Elasticity and constitution of the Earth's interior. *Journal of Geophysical Research*, 57(2), 227-286. http://10.1029/JZ057i002p00227
- Boujibar, A., Andrault, D., Bouhifd, M. A., Bolfan-Casanova, N., Devidal, J.-L., & Trcera, N. (2014). Metal—silicate partitioning of sulphur, new experimental and thermodynamic constraints on planetary accretion. *Earth and Planetary Science Letters*, *391*, 42-54. http://10.1016/j.epsl.2014.01.021
- Boulard, E., Gloter, A., Corgne, A., Antonangeli, D., Auzende, A. L., Perrillat, J. P., et al. (2011). New host for carbon in the deep Earth. *Proceedings of the National Academy of Sciences*, 108(13), 5184-5187. Article. http://10.1073/pnas.1016934108
- Brenker, F. E., Vollmer, C., Vincze, L., Vekemans, B., Szymanski, A., Janssens, K., et al. (2007). Carbonates from the lower part of transition zone or even the lower mantle. *Earth and Planetary Science Letters*, 260(1-2), 1-9. http://10.1016/j.epsl.2007.02.038
- Breton, H., Komabayashi, T., Thompson, S., Potts, N., McGuire, C., Suehiro, S., et al. (2019). Static compression of Fe₄N to 77 GPa and its implications for nitrogen storage in the deep Earth. *American Mineralogist*, 104(12), 1781-1787. http://10.2138/am-2019-7065
- Breuer, D., Rueckriemen, T., & Spohn, T. (2015). Iron snow, crystal floats, and inner-core growth: modes of core solidification and implications for dynamos in terrestrial planets and moons. *Progress in Earth and Planetary Science*, 2(1). http://10.1186/s40645-015-0069-y
- Brown, J. M., & Shankland, T. J. (1981). Thermodynamic Parameters in the Earth as Determined from Seismic Profiles. *Geophysical Journal of the Royal Astronomical Society*, 66(3), 579-596. http://10.1111/j.1365-246X.1981.tb04891.x
- Bulanova, G. P., Walter, M. J., Smith, C. B., Kohn, S. C., Armstrong, L. S., Blundy, J., & Gobbo, L. (2010). Mineral inclusions in sublithospheric diamonds from Collier 4 kimberlite pipe, Juina, Brazil: subducted protoliths, carbonated melts and primary kimberlite magmatism. *Contributions to Mineralogy and Petrology*, *160*(4), 489-510. http://10.1007/s00410-010-0490-6
- Caracas, R. (2016). Crystal structures of Core materials. *Deep Earth: Physics and Chemistry of the Lower Mantle and Core*, 217, 57-68.

- Carlson, R. W., Garnero, E., Harrison, T. M., Li, J., Manga, M., McDonough, W. F., et al. (2014). How Did Early Earth Become Our Modern World? *Annual Review of Earth and Planetary Sciences*, 42(1), 151-178. http://10.1146/annurev-earth-060313-055016
- Cartigny, P., Palot, M., Thomassot, E., & Harris, J. W. (2014). Diamond Formation: A Stable Isotope Perspective. *Annual Review of Earth and Planetary Sciences*, *Vol* 42, 42(1), 699-732. http://10.1146/annurev-earth-042711-105259
- Chen, B., Gao, L., Funakoshi, K., & Li, J. (2007). Thermal expansion of iron-rich alloys and implications for the Earth's core. *Proceedings of the National Academy of Sciences*, 104(22), 9162-9167. http://10.1073/pnas.0610474104
- Chen, B., Gao, L. L., Lavina, B., Dera, P., Alp, E. E., Zhao, J. Y., & Li, J. (2012). Magneto-elastic coupling in compressed Fe₇C₃ supports carbon in Earth's inner core. *Geophysical Research Letters*, 39(18). http://10.1029/2012gl052875
- Chen, B., Lai, X. J., Li, J., Liu, J. C., Zhao, J. Y., Bi, W. L., et al. (2018a). Experimental constraints on the sound velocities of cementite Fe₃C to core pressures. *Earth and Planetary Science Letters*, 494, 164-171. http://10.1016/j.epsl.2018.05.002
- Chen, B., & Li, J. (2016). Carbon in the core. *Deep Earth: Physics and Chemistry of the Lower Mantle and Core*, 277-288.
- Chen, B., Li, J., & Hauck, S. A. (2008). Non-ideal liquidus curve in the Fe-S system and Mercury's snowing core. *Geophysical Research Letters*, *35*(7). http://10.1029/2008gl033311
- Chen, B., Li, Z., Zhang, D., Liu, J., Hu, M. Y., Zhao, J., et al. (2014). Hidden carbon in Earth's inner core revealed by shear softening in dense Fe₇C₃. *Proceedings of the National Academy of Sciences*, 111(50), 17755-17758. http://10.1073/pnas.1411154111
- Chen, C., Liu, Y., Feng, L., Foley, S. F., Zhou, L., Ducea, M. N., & Hu, Z. (2018b). Calcium isotope evidence for subduction-enriched lithospheric mantle under the northern North China Craton. *Geochimica et Cosmochimica Acta*, 238, 55-67. http://10.1016/j.gca.2018.06.038
- Corgne, A., Liebske, C., Wood, B. J., Rubie, D. C., & Frost, D. J. (2005). Silicate perovskite-melt partitioning of trace elements and geochemical signature of a deep perovskitic reservoir. *Geochimica et Cosmochimica Acta*, 69(2), 485-496. http://10.1016/j.gca.2004.06.041
- Costa-Krämer, J. L., Borsa, D. M., García-Martín, J. M., Martín-González, M. S., Boerma, D. O., & Briones, F. (2004). Structure and magnetism of single-phase epitaxial γ′–Fe₄N. *Physical Review B*, 69(14). http://10.1103/PhysRevB.69.144402
- Cottaar, S., Heister, T., Rose, I., & Unterborn, C. (2014). BurnMan: A lower mantle mineral physics toolkit. *Geochemistry Geophysics Geosystems*, 15(4), 1164-1179. http://10.1002/2013gc005122

- Dasgupta, R. (2013). Ingassing, Storage, and Outgassing of Terrestrial Carbon through Geologic Time. *Carbon in Earth*, 75, 183-229. http://10.2138/rmg.2013.75.7
- Dasgupta, R., & Hirschmann, M. M. (2006). Melting in the Earth's deep upper mantle caused by carbon dioxide. *Nature*, 440(7084), 659-662. Article. http://10.1038/nature04612
- Dasgupta, R., & Hirschmann, M. M. (2010). The deep carbon cycle and melting in Earth's interior. *Earth and Planetary Science Letters*, 298(1-2), 1-13. http://10.1016/j.epsl.2010.06.039
- Dauphas, N., John, S. G., & Rouxel, O. (2017). Iron isotope systematics. *Reviews in Mineralogy and Geochemistry*, 82(1), 415-510.
- De Waele, S., Lejaeghere, K., Leunis, E., Duprez, L., & Cottenier, S. (2019). A first-principles reassessment of the Fe-N phase diagram in the low-nitrogen limit. *Journal of Alloys and Compounds*, 775, 758-768. http://10.1016/j.jallcom.2018.09.356
- Dewaele, A., Loubeyre, P., Occelli, F., Mezouar, M., Dorogokupets, P. I., & Torrent, M. (2006). Quasihydrostatic equation of state of iron above 2 Mbar. *Physical Review Letters*, 97(21), 215504. http://10.1103/PhysRevLett.97.215504
- Dirba, I., Yazdi, M. B., Radetinac, A., Komissinskiy, P., Flege, S., Gutfleisch, O., & Alff, L. (2015). Growth, structure, and magnetic properties of *y*'-FeN₄ thin films. *Journal of Magnetism and Magnetic Materials*, *379*, 151-155. http://10.1016/j.jmmm.2014.12.033
- Dorfman, S. M. (2016). Phase Diagrams and Thermodynamics of Lower Mantle Materials. *Deep Earth: Physics and Chemistry of the Lower Mantle and Core*, 217, 241-252. http://10.1002/9781118992487
- Dorfman, S. M., Badro, J., Nabiei, F., Prakapenka, V. B., Cantoni, M., & Gillet, P. (2018). Carbonate stability in the reduced lower mantle. *Earth and Planetary Science Letters*, 489, 84-91. http://10.1016/j.epsl.2018.02.035
- Dorfman, S. M., Potapkin, V., Lv, M., Greenberg, E., Kupenko, I., Chumakov, A. I., et al. (2020). Effects of composition and pressure on electronic states of iron in bridgmanite. *American Mineralogist*, 105(7), 1030-1039. http://10.2138/am-2020-7309
- dos Santos, A. V., & Samudio Pérez, C. A. (2016). Ab initio investigation of the substitution effects of 2p elements on the electronic structure of γ -Fe₄X (X = B, C, N, and O) in the ground state. *Journal of Materials Research*, 31(2), 202-212. http://10.1557/jmr.2015.394
- Drewitt, J. W. E., Walter, M. J., Zhang, H. L., McMahon, S. C., Edwards, D., Heinen, B. J., et al. (2019). The fate of carbonate in oceanic crust subducted into earth's lower mantle. *Earth and Planetary Science Letters*, 511, 213-222. http://10.1016/j.epsl.2019.01.041
- Dubrovinsky, L., Dubrovinskaia, N., Abrikosov, I. A., Vennstrom, M., Westman, F., Carlson, S., et al. (2001). Pressure-induced Invar effect in Fe-Ni alloys. *Physical Review Letters*, 86(21), 4851-4854. http://10.1103/PhysRevLett.86.4851

- Dziewonski, A. M., & Anderson, D. L. (1981). Preliminary Reference Earth Model. *Physics of the Earth and Planetary Interiors*, 25(4), 297-356. http://10.1016/0031-9201(81)90046-7
- Fabrichnaya, O., Saxena, S. K., Richet, P., & Westrum, E. F. (2004). Thermodynamic data, models, and phase diagrams in multicomponent oxide systems: an assessment for materials and planetary scientists based on calorimetric, volumetric and phase equilibrium data: Springer Science & Business Media.
- Fantle, M. S., & Tipper, E. T. (2014). Calcium isotopes in the global biogeochemical Ca cycle: implications for development of a Ca isotope proxy. *Earth-Science Reviews*, 129, 148-177.
- Fei, Y. (1995). Thermal expansion. *Mineral physics and crystallography: a handbook of physical constants*, 2, 29-44.
- Fei, Y., & Bertka, C. (2005). Planetary science. The interior of Mars. *Science*, 308(5725), 1120-1121. http://10.1126/science.1110531
- Fei, Y., Ricolleau, A., Frank, M., Mibe, K., Shen, G., & Prakapenka, V. (2007). Toward an internally consistent pressure scale. *Proceedings of the National Academy of Sciences*, 104(22), 9182-9186. http://10.1073/pnas.0609013104
- Fiquet, G., Auzende, A. L., Siebert, J., Corgne, A., Bureau, H., Ozawa, H., & Garbarino, G. (2010). Melting of peridotite to 140 gigapascals. *Science*, 329(5998), 1516-1518. http://10.1126/science.1192448
- Fischer, R. A., Cottrell, E., Hauri, E., Lee, K. K. M., & Le Voyer, M. (2020). The carbon content of Earth and its core. *Proceedings of the National Academy of Sciences of the United States of America*, 117(16), 8743-8749. http://10.1073/pnas.1919930117
- French, S. W., & Romanowicz, B. (2015). Broad plumes rooted at the base of the Earth's mantle beneath major hotspots. *Nature*, 525(7567), 95-99. http://10.1038/nature14876
- Frost, D. J., & McCammon, C. A. (2008). The redox state of Earth's mantle. *Annual Review of Earth and Planetary Sciences*, 36(1), 389-420. http://10.1146/annurev.earth.36.031207.124322
- Gavryushkin, P. N., Martirosyan, N. S., Inerbaev, T. M., Popov, Z. I., Rashchenko, S. V., Likhacheva, A. Y., et al. (2017). Aragonite-II and CaCO₃-VII: New High-Pressure, High-Temperature Polymorphs of CaCO₃. *Crystal Growth & Design*, *17*(12), 6291-6296. http://10.1021/acs.cgd.7b00977
- Genova, A., Goossens, S., Mazarico, E., Lemoine, F. G., Neumann, G. A., Kuang, W., et al. (2019). Geodetic Evidence That Mercury Has A Solid Inner Core. *Geophysical Research Letters*, 46(7), 3625-3633. http://10.1029/2018gl081135
- Ghosh, S., Litasov, K., & Ohtani, E. (2014). Phase relations and melting of carbonated peridotite between 10 and 20 GPa: a proxy for alkali- and CO₂-rich silicate melts in the deep mantle.

- Contributions to Mineralogy and Petrology, 167(2), 23. Article. http://10.1007/s00410-014-0964-z
- Gressmann, T., Wohlschlögel, M., Shang, S., Welzel, U., Leineweber, A., Mittemeijer, E. J., & Liu, Z. K. (2007). Elastic anisotropy of γ' -Fe₄N and elastic grain interaction in γ' -Fe₄N_{1-y} layers on α -Fe: First-principles calculations and diffraction stress measurements. *Acta Materialia*, 55(17), 5833-5843. http://10.1016/j.actamat.2007.07.001
- Gu, T., Fei, Y., Wu, X., & Qin, S. (2014). High-pressure behavior of Fe₃P and the role of phosphorus in planetary cores. *Earth and Planetary Science Letters*, *390*, 296-303. http://10.1016/j.epsl.2014.01.019
- Gu, T., Fei, Y., Wu, X., & Qin, S. (2016). Phase stabilities and spin transitions of Fe₃($S_{1-x}P_x$) at high pressure and its implications in meteorites. *American Mineralogist*, 101(1), 205-210. http://10.2138/am-2016-5466
- Guo, K., Rau, D., von Appen, J., Prots, Y., Schnelle, W., Dronskowski, R., et al. (2013). High pressure high-temperature behavior and magnetic properties of Fe₄N: experiment and theory. *High Pressure Research*, *33*(3), 684-696. http://10.1080/08957959.2013.809715
- Hazen, R. M., & Schiffries, C. M. (2013). Why Deep Carbon? *Reviews in Mineralogy and Geochemistry*, 75(1), 1-6. http://10.2138/rmg.2013.75.1
- Hirose, K., Labrosse, S., & Hernlund, J. (2013). Composition and State of the Core. In R. Jeanloz (Ed.), *Annual Review of Earth and Planetary Sciences*, *Vol* 41 (Vol. 41, pp. 657-691): Annual Reviews.
- Hirschmann, M. M. (2016). Constraints on the early delivery and fractionation of Earth's major volatiles from C/H, C/N, and C/S ratios. *American Mineralogist*, 101(3), 540-553.
- Howell, D., Stachel, T., Stern, R. A., Pearson, D. G., Nestola, F., Hardman, M. F., et al. (2020). Deep carbon through time: Earth's diamond record and its implications for carbon cycling and fluid speciation in the mantle. *Geochimica et Cosmochimica Acta*, 275, 99-122. http://10.1016/j.gca.2020.02.011
- Hrubiak, R., Sinogeikin, S., Rod, E., & Shen, G. (2015). The laser micro-machining system for diamond anvil cell experiments and general precision machining applications at the High Pressure Collaborative Access Team. *Review of Scientific Instruments*, 86(7), 072202. Article. http://10.1063/1.4926889
- Ionov, D. A., Qi, Y.-H., Kang, J.-T., Golovin, A. V., Oleinikov, O. B., Zheng, W., et al. (2019). Calcium isotopic signatures of carbonatite and silicate metasomatism, melt percolation and crustal recycling in the lithospheric mantle. *Geochimica et Cosmochimica Acta*, 248, 1-13. http://10.1016/j.gca.2018.12.023
- Ishimatsu, N., Maruyama, H., Kawamura, N., Suzuki, M., Ohishi, Y., Ito, M., et al. (2003). Pressure-induced magnetic transition in Fe₄N probed by Fe *K*-edge XMCD measurement. *Journal of the Physical Society of Japan*, 72(9), 2372-2376. http://10.1143/JPSJ.72.2372

- Isshiki, M., Irifune, T., Hirose, K., Ono, S., Ohishi, Y., Watanuki, T., et al. (2004). Stability of magnesite and its high-pressure form in the lowermost mantle. *Nature*, 427(6969), 60-63. http://10.1038/nature02181
- Jackson, I. (1998). Elasticity, composition and temperature of the Earth's lower mantle: a reappraisal. *Geophysical Journal International*, 134(1), 291-311. http://10.1046/j.1365-246x.1998.00560.x
- Jackson, I., & Rigden, S. M. (1996). Analysis of *P-V-T* data: Constraints on the thermoelastic properties of high-pressure minerals. *Physics of the Earth and Planetary Interiors*, 96(2-3), 85-112. http://10.1016/0031-9201(96)03143-3
- Jeanloz, R. (1981). Finite-Strain Equation of State for High-Pressure Phases. *Geophysical Research Letters*, 8(12), 1219-1222. http://10.1029/GL008i012p01219
- Kakizawa, S., Inoue, T., Suenami, H., & Kikegawa, T. (2015). Decarbonation and melting in MgCO₃–SiO₂ system at high temperature and high pressure. *Journal of Mineralogical and Petrological Sciences*, 110(4), 179-188. http://10.2465/jmps.150124
- Kamada, S., Ohtani, E., Terasaki, H., Sakai, T., Takahashi, S., Hirao, N., & Ohishi, Y. (2014). Equation of state of Fe₃S at room temperature up to 2 megabars. *Physics of the Earth and Planetary Interiors*, 228, 106-113. http://10.1016/j.pepi.2013.11.001
- Kaminsky, F., & Wirth, R. (2017). Nitrides and carbonitrides from the lowermost mantle and their importance in the search for Earth's "lost" nitrogen. *American Mineralogist*, 102(8), 1667-1676. http://10.2138/am-2017-6101
- Kang, J.-T., Ionov, D. A., Liu, F., Zhang, C.-L., Golovin, A. V., Qin, L.-P., et al. (2017). Calcium isotopic fractionation in mantle peridotites by melting and metasomatism and Ca isotope composition of the Bulk Silicate Earth. *Earth and Planetary Science Letters*, 474, 128-137.
- Kelemen, P. B., & Manning, C. E. (2015). Reevaluating carbon fluxes in subduction zones, what goes down, mostly comes up. *Proceedings of the National Academy of Sciences*, 112(30), E3997-4006. Article. http://10.1073/pnas.1507889112
- Kerrick, D. M., & Connolly, J. A. (2001). Metamorphic devolatilization of subducted marine sediments and the transport of volatiles into the Earth's mantle. *Nature*, *411*(6835), 293-296. http://10.1038/35077056
- Kiseeva, E. S., Litasov, K. D., Yaxley, G. M., Ohtani, E., & Kamenetsky, V. S. (2013). Melting and Phase Relations of Carbonated Eclogite at 9-21 GPa and the Petrogenesis of Alkali-Rich Melts in the Deep Mantle. *Journal of Petrology*, *54*(8), 1555-1583. Article. http://10.1093/petrology/egt023
- Kiseeva, E. S., Yaxley, G. M., Hermann, J., Litasov, K. D., Rosenthal, A., & Kamenetsky, V. S. (2012). An Experimental Study of Carbonated Eclogite at 3.5-5.5 GPa-Implications for Silicate and Carbonate Metasomatism in the Cratonic Mantle. *Journal of Petrology*, 53(4), 727-759. Article. http://10.1093/petrology/egr078

- Klotz, S., Chervin, J. C., Munsch, P., & Le Marchand, G. (2009). Hydrostatic limits of 11 pressure transmitting media. *Journal of Physics D-Applied Physics*, 42(7), 075413. http://10.1088/0022-3727/42/7/075413
- Kusakabe, M., Hirose, K., Sinmyo, R., Kuwayama, Y., Ohishi, Y., & Helffrich, G. (2019). Melting Curve and Equation of State of β -Fe₇N₃: Nitrogen in the Core? *Journal of Geophysical Research: Solid Earth.* http://10.1029/2018jb015823
- Lai, X., Zhu, F., Liu, Y., Bi, W., Zhao, J., Alp, E. E., et al. (2020). Elastic and magnetic properties of Fe₃P up to core pressures: Phosphorus in the Earth's core. *Earth and Planetary Science Letters*, *531*, 115974. http://10.1016/j.epsl.2019.115974
- Le Bail, A. (2012). Whole powder pattern decomposition methods and applications: A retrospection. *Powder Diffraction*, 20(4), 316-326. http://10.1154/1.2135315
- Le Bail, A., Duroy, H., & Fourquet, J. (1988). Ab-initio structure determination of LiSbWO₆ by X-ray powder diffraction. *Materials Research Bulletin*, 23(3), 447-452.
- Leineweber, A., Jacobs, H., Hüning, F., Lueken, H., & Kockelmann, W. (2001). Nitrogen ordering and ferromagnetic properties of ϵ -Fe₃N_{1+ x} (0.10 \leq x \leq 0.39) and ϵ -Fe₃(N_{0.80}C_{0.20})_{1.38}. *Journal of Alloys and Compounds, 316*(1-2), 21-38. http://10.1016/S0925-8388(00)01435-3
- Li, J., & Fei, Y. (2014). Experimental Constraints on Core Composition. In H. D. Holland & K. K. Turekian (Eds.), *Treatise on Geochemistry* (pp. 527-557). Oxford: Elsevier.
- Li, J., Mao, H. K., Fei, Y., Gregoryanz, E., Eremets, M., & Zha, C. S. (2002). Compression of Fe₃C to 30 GPa at room temperature. *Physics and Chemistry of Minerals*, 29(3), 166-169. http://10.1007/s00269-001-0224-4
- Li, X. Y., Zhang, Z. G., Lin, J. F., Ni, H. W., Prakapenka, V. B., & Mao, Z. (2018). New High-Pressure Phase of CaCO₃ at the Topmost Lower Mantle: Implication for the Deep-Mantle Carbon Transportation. *Geophysical Research Letters*, 45(3), 1355-1360. http://10.1002/2017gl076536
- Li, Y., Zou, Y. T., Chen, T., Wang, X. B., Qi, X. T., Chen, H. Y., et al. (2015). *P-V-T* equation of state and high-pressure behavior of CaCO₃ aragonite. *American Mineralogist*, 100(10), 2323-2329. Article. http://10.2138/am-2015-5246
- Li, Z. Y., Li, J., Lange, R., Liu, J. C., & Mintzer, B. (2017). Determination of calcium carbonate and sodium carbonate melting curves up to Earth's transition zone pressures with implications for the deep carbon cycle. *Earth and Planetary Science Letters*, 457, 395-402. http://10.1016/j.epsl.2016.10.027
- Lin, J.-F., Fei, Y., Sturhahn, W., Zhao, J., Mao, H.-k., & Hemley, R. J. (2004a). Magnetic transition and sound velocities of Fe₃S at high pressure: implications for Earth and planetary cores. *Earth and Planetary Science Letters*, 226(1-2), 33-40. http://10.1016/j.epsl.2004.07.018

- Lin, J. F., Speziale, S., Mao, Z., & Marquardt, H. (2013). Effects of the Electronic Spin Transitions of Iron in Lower Mantle Minerals: Implications for Deep Mantle Geophysics and Geochemistry. *Reviews of Geophysics*, *51*(2), 244-275. http://10.1002/rog.20010
- Lin, J. F., Struzhkin, V. V., Mao, H. K., Hemley, R. J., Chow, P., Hu, M. Y., & Li, J. (2004b). Magnetic transition in compressed Fe₃C from x-ray emission spectroscopy. *Physical Review B*, 70(21). http://10.1103/PhysRevB.70.212405
- Litasov, K. D., Fei, Y., Ohtani, E., Kuribayashi, T., & Funakoshi, K. (2008). Thermal equation of state of magnesite to 32GPa and 2073K. *Physics of the Earth and Planetary Interiors*, 168(3-4), 191-203. http://10.1016/j.pepi.2008.06.018
- Litasov, K. D., Sharygin, I. S., Dorogokupets, P. I., Shatskiy, A., Gavryushkin, P. N., Sokolova, T. S., et al. (2013). Thermal equation of state and thermodynamic properties of iron carbide Fe₃C to 31 GPa and 1473 K. *Journal of Geophysical Research-Solid Earth*, *118*(10), 5274-5284. http://10.1002/2013jb010270
- Litasov, K. D., Shatskiy, A., Gavryushkin, P. N., Bekhtenova, A. E., Dorogokupets, P. I., Danilov, B. S., et al. (2017a). *P-V-T* equation of state of CaCO₃ aragonite to 29 GPa and 1673 K: In situ X-ray diffraction study. *Physics of the Earth and Planetary Interiors*, 265, 82-91. http://10.1016/j.pepi.2017.02.006
- Litasov, K. D., Shatskiy, A., Ponomarev, D. S., & Gavryushkin, P. N. (2017b). Equations of state of iron nitrides ϵ -Fe₃N_x and γ -Fe₄N_y to 30 GPa and 1200 K and implication for nitrogen in the Earth's core. *Journal of Geophysical Research: Solid Earth.* http://10.1002/2017JB014059
- Liu, J., Dauphas, N., Roskosz, M., Hu, M. Y., Yang, H., Bi, W., et al. (2017). Iron isotopic fractionation between silicate mantle and metallic core at high pressure. *Nature Communications*, 8, 14377. http://10.1038/ncomms14377
- Liu, J., Dorfman, S. M., Lv, M., Li, J., Zhu, F., & Kono, Y. (2019). Loss of immiscible nitrogen from metallic melt explains Earth's missing nitrogen. *Geochemical Perspectives Letters*, 18-22. http://10.7185/geochemlet.1919
- Liu, J. C., Li, J., & Ikuta, D. (2016). Elastic softening in Fe₇C₃ with implications for Earth's deep carbon reservoirs. *Journal of Geophysical Research-Solid Earth*, 121(3), 1514-1524. Article. http://10.1002/2015jb012701
- Lobanov, S. S., Dong, X., Martirosyan, N. S., Samtsevich, A. I., Stevanovic, V., Gavryushkin, P. N., et al. (2017). Raman spectroscopy and X-ray diffraction of sp^3 CaCO₃ at lower mantle pressures. *Physical Review B*, 96(10), 104101. http://10.1103/PhysRevB.96.104101
- Lord, O. T., Walter, M. J., Dasgupta, R., Walker, D., & Clark, S. M. (2009). Melting in the Fe–C system to 70 GPa. *Earth and Planetary Science Letters*, 284(1-2), 157-167. http://10.1016/j.epsl.2009.04.017

- Luth, R. W. (1999). Carbon and carbonates in the mantle. *Mantle Petrology: Field Observations and High Pressure Experimentation: A Tribute to Francis R. (Joe) Boyd, 6*, 297-316.
- Luth, R. W. (2004). Experimental determination of the reaction aragonite + magnesite = dolomite at 5 to 9 GPa. *Contributions to Mineralogy and Petrology*, 141(2), 222-232. http://10.1007/s004100100238
- Lv, M., Dorfman, S. M., Badro, J., Borensztajn, S., Greenberg, E., & Prakapenka, V. B. (2021). Reversal of carbonate-silicate cation exchange in cold slabs in Earth's lower mantle. *Nature Communications*, 12(1). http://10.1038/s41467-021-21761-9
- Lv, M., Liu, J., Greenberg, E., Prakapenka, V. B., & Dorfman, S. M. (2020a). Thermal equation of state of post-aragonite CaCO₃-Pmmn. American Mineralogist, 105(9), 1365-1374. http://10.2138/am-2020-7279
- Lv, M., Liu, J., Zhu, F., Li, J., Zhang, D., Xiao, Y., & Dorfman, S. M. (2020b). Spin Transitions and Compressibility of ϵ -Fe₇N₃ and γ' -Fe₄N: Implications for Iron Alloys in Terrestrial Planet Cores. *Journal of Geophysical Research: Solid Earth*, 125(11). http://10.1029/2020jb020660
- Macris, C. A., Young, E. D., & Manning, C. E. (2013). Experimental determination of equilibrium magnesium isotope fractionation between spinel, forsterite, and magnesite from 600 to 800 C. *Geochimica et Cosmochimica Acta, 118*, 18-32.
- Maeda, F., Ohtani, E., Kamada, S., Sakamaki, T., Hirao, N., & Ohishi, Y. (2017). Diamond formation in the deep lower mantle: a high-pressure reaction of MgCO₃ and SiO₂. *Scientific Reports*, 7, 40602. http://10.1038/srep40602
- Mao, H. K., Xu, J., & Bell, P. M. (1986). Calibration of the ruby pressure gauge to 800 Kbar under quasi-hydrostatic conditions. *Journal of Geophysical Research-Solid Earth and Planets*, 91(B5), 4673-4676. http://10.1029/JB091iB05p04673
- Mao, Z., Armentrout, M., Rainey, E., Manning, C. E., Dera, P., Prakapenka, V. B., & Kavner, A. (2011a). Dolomite III: A new candidate lower mantle carbonate. *Geophysical Research Letters*, *38*(22), n/a-n/a. http://10.1029/2011gl049519
- Mao, Z., Lin, J. F., Liu, J., & Prakapenka, V. B. (2011b). Thermal equation of state of lower-mantle ferropericlase across the spin crossover. *Geophysical Research Letters*, 38(23). http://10.1029/2011gl049915
- Mao, Z., Lin, J. F., Yang, J., Wu, J. J., Watson, H. C., Xiao, Y. M., et al. (2014). Spin and valence states of iron in Al-bearing silicate glass at high pressures studied by synchrotron Mossbauer and X-ray emission spectroscopy. *American Mineralogist*, 99(2-3), 415-423. http://10.2138/am.2014.4490
- Marcondes, M. L., Justo, J. F., & Assali, L. V. C. (2016). Carbonates at high pressures: Possible carriers for deep carbon reservoirs in the Earth's lower mantle. *Physical Review B*.

- Margot, J. L., Peale, S. J., Jurgens, R. F., Slade, M. A., & Holin, I. V. (2007). Large longitude libration of Mercury reveals a molten core. *Science*, 316(5825), 710-714. http://10.1126/science.1140514
- Martirosyan, N. S., Yoshino, T., Shatskiy, A., Chanyshev, A. D., & Litasov, K. D. (2016). The CaCO₃–Fe interaction: Kinetic approach for carbonate subduction to the deep Earth's mantle. *Physics of the Earth and Planetary Interiors*, 259, 1-9. http://10.1016/j.pepi.2016.08.008
- Marty, B. (2012). The origins and concentrations of water, carbon, nitrogen and noble gases on Earth. *Earth and Planetary Science Letters*, 313-314, 56-66. http://10.1016/j.epsl.2011.10.040
- Mcdonough, W. F., & Sun, S. S. (1995). The Composition of the Earth. *Chemical Geology*, *120*(3-4), 223-253. http://10.1016/0009-2541(94)00140-4
- Minobe, S., Nakajima, Y., Hirose, K., & Ohishi, Y. (2015). Stability and compressibility of a new iron-nitride β -Fe₇N₃ to core pressures. *Geophysical Research Letters*, 42(13), 5206-5211. http://10.1002/2015gl064496
- Mookherjee, M., Nakajima, Y., Steinle-Neumann, G., Glazyrin, K., Wu, X. A., Dubrovinsky, L., et al. (2011). High-pressure behavior of iron carbide (Fe₇C₃) at inner core conditions. *Journal of Geophysical Research-Solid Earth*, 116(B4). http://10.1029/2010jb007819
- Nakajima, Y., Takahashi, E., Sata, N., Nishihara, Y., Hirose, K., Funakoshi, K., & Ohishi, Y. (2011). Thermoelastic property and high-pressure stability of Fe₇C₃: Implication for iron-carbide in the Earth's core. *American Mineralogist*, *96*(7), 1158-1165. http://10.2138/am.2011.3703
- Nestola, F., Korolev, N., Kopylova, M., Rotiroti, N., Pearson, D. G., Pamato, M. G., et al. (2018). CaSiO₃ perovskite in diamond indicates the recycling of oceanic crust into the lower mantle. *Nature*, 555(7695), 237-241. http://10.1038/nature25972
- Niewa, R., Rau, D., Wosylus, A., Meier, K., Hanfland, M., Wessel, M., et al. (2009a). High-pressure, high-temperature single-crystal growth, ab initio electronic structure calculations, and equation of state of ε -Fe₃N_{1+x}. *Chemistry of Materials*, 21(2), 392-398.
- Niewa, R., Rau, D., Wosylus, A., Meier, K., Wessel, M., Hanfland, M., et al. (2009b). High-pressure high-temperature phase transition of γ'-Fe₄N. *Journal of Alloys and Compounds*, 480(1), 76-80. http://10.1016/j.jallcom.2008.09.178
- Nomura, R., Hirose, K., Uesugi, K., Ohishi, Y., Tsuchiyama, A., Miyake, A., & Ueno, Y. (2014). Low core-mantle boundary temperature inferred from the solidus of pyrolite. *Science*, 343(6170), 522-525. http://10.1126/science.1248186
- Oganov, A. R., Glass, C. W., & Ono, S. (2006). High-pressure phases of CaCO₃: Crystal structure prediction and experiment. *Earth and Planetary Science Letters*, 241(1-2), 95-103. http://10.1016/j.epsl.2005.10.014

- Oganov, A. R., Hemley, R. J., Hazen, R. M., & Jones, A. P. (2013). Structure, Bonding, and Mineralogy of Carbon at Extreme Conditions. *Carbon in Earth*, 75(1), 47-77. http://10.2138/rmg.2013.75.3
- Oganov, A. R., Ono, S., Ma, Y. M., Glass, C. W., & Garcia, A. (2008). Novel high-pressure structures of MgCO₃, CaCO₃ and CO₂ and their role in Earth's lower mantle. *Earth and Planetary Science Letters*, 273(1-2), 38-47. Article. http://10.1016/j.epsl.2008.06.005
- Ono, S., Kikegawa, T., & Ohishi, Y. (2007). High-pressure transition of CaCO₃. *American Mineralogist*, 92(7), 1246-1249. http://10.2138/am.2007.2649
- Ono, S., Kikegawa, T., Ohishi, Y., & Tsuchiya, J. (2005). Post-aragonite phase transformation in CaCO₃ at 40 GPa. *American Mineralogist*, 90(4), 667-671. http://10.2138/am.2005.1610
- Ono, S., & Mibe, K. (2010). Magnetic transition of iron carbide at high pressures. *Physics of the Earth and Planetary Interiors*, 180(1-2), 1-6. http://10.1016/j.pepi.2010.03.008
- Palaich, S. E. M., Heffern, R. A., Hanfland, M., Lausi, A., Kavner, A., Manning, C. E., & Merlini, M. (2016). High-pressure compressibility and thermal expansion of aragonite. *American Mineralogist*, 101(7-8), 1651-1658. http://10.2138/am-2016-5528
- Palyanov, Y. N., Bataleva, Y. V., Sokol, A. G., Borzdov, Y. M., Kupriyanov, I. N., Reutsky, V. N., & Sobolev, N. V. (2013). Mantle-slab interaction and redox mechanism of diamond formation. *Proceedings of the National Academy of Sciences*, 110(51), 20408-20413. http://10.1073/pnas.1313340110
- Pickard, C. J., & Needs, R. J. (2015). Structures and stability of calcium and magnesium carbonates at mantle pressures. *Physical Review B*, *91*(10). http://10.1103/PhysRevB.91.104101
- Plank, T., & Manning, C. E. (2019). Subducting carbon. *Nature*, *574*(7778), 343-352. http://10.1038/s41586-019-1643-z
- Poirier, J.-P. (1994). Light elements in the Earth's outer core: A critical review. *Physics of the Earth and Planetary Interiors*, 85(3-4), 319-337. http://10.1016/0031-9201(94)90120-1
- Poirier, J.-P. (2000). *Introduction to the Physics of the Earth's Interior*: Cambridge University Press.
- Poli, S., Franzolin, E., Fumagalli, P., & Crottini, A. (2009). The transport of carbon and hydrogen in subducted oceanic crust: An experimental study to 5 GPa. *Earth and Planetary Science Letters*, 278(3-4), 350-360. http://10.1016/j.epsl.2008.12.022
- Poli, S., & Schmidt, M. W. (2002). Petrology of subducted slabs. *Annual Review of Earth and Planetary Sciences*, 30(1), 207-235. http://10.1146/annurev.earth.30.091201.140550
- Popov, Z. I., Litasov, K. D., Gavryushkin, P. N., Ovchinnikov, S. G., & Fedorov, A. S. (2015). Theoretical study of γ' -Fe₄N and ε-Fe_xN iron nitrides at pressures up to 500 GPa. *JETP Letters*, 101(6), 371-375. http://10.1134/s0021364015060090

- Prakapenka, V. B., Kubo, A., Kuznetsov, A., Laskin, A., Shkurikhin, O., Dera, P., et al. (2008). Advanced flat top laser heating system for high pressure research at GSECARS: application to the melting behavior of germanium. *High Pressure Research*, 28(3), 225-235. http://10.1080/08957950802050718
- Prescher, C., Dubrovinsky, L., McCammon, C., Glazyrin, K., Nakajima, Y., Kantor, A., et al. (2012). Structurally hidden magnetic transitions in Fe₃C at high pressures. *Physical Review B*, 85(14). http://10.1103/PhysRevB.85.140402
- Prescher, C., & Prakapenka, V. B. (2015). DIOPTAS: a program for reduction of two-dimensional X-ray diffraction data and data exploration. *High Pressure Research*, *35*(3), 223-230. http://10.1080/08957959.2015.1059835
- Rivers, M., Prakapenka, V. B., Kubo, A., Pullins, C., Holl, C. M., & Jacobsen, S. D. (2008). The COMPRES/GSECARS gas-loading system for diamond anvil cells at the Advanced Photon Source. *High Pressure Research*, 28(3), 273-292. http://10.1080/08957950802333593
- Robbins, M., & White, J. G. (1964). Magnetic Properties of Epsilon-Iron Nitride. *Journal of Physics and Chemistry of Solids*, 25(7), 717-&. http://10.1016/0022-3697(64)90182-9
- Rohrbach, A., & Schmidt, M. W. (2011). Redox freezing and melting in the Earth's deep mantle resulting from carbon-iron redox coupling. *Nature*, 472(7342), 209-212. Article. http://10.1038/nature09899
- Rubie, D. C., & Ross, C. R. (1994). Kinetics of the Olivine-Spinel Transformation in Subducting Lithosphere Experimental Constraints and Implications for Deep Slab Processes. *Physics of the Earth and Planetary Interiors*, 86(1-3), 223-241. http://Doi 10.1016/0031-9201(94)05070-8
- Rubin, A. E., & Ma, C. (2017). Meteoritic minerals and their origins. *Geochemistry*, 77(3), 325-385. http://10.1016/j.chemer.2017.01.005
- Sagatov, N., Gavryushkin, P. N., Inerbaev, T. M., & Litasov, K. D. (2019). New high-pressure phases of Fe₇N₃ and Fe₇C₃ stable at Earth's core conditions: evidences for carbon–nitrogen isomorphism in Fe-compounds. *RSC Advances*, *9*(7), 3577-3581. http://10.1039/c8ra09942a
- Sagatov, N. E., Gavryushkin, P. N., Banayev, M. V., Inerbaev, T. M., & Litasov, K. D. (2020). Phase relations in the Fe-P system at high pressures and temperatures from ab initio computations. *High Pressure Research*, 40(2), 235-244. http://10.1080/08957959.2020.1740699
- Sakai, T., Takahashi, S., Nishitani, N., Mashino, I., Ohtani, E., & Hirao, N. (2014). Equation of state of pure iron and Fe_{0.9}Ni_{0.1} alloy up to 3 Mbar. *Physics of the Earth and Planetary Interiors*, 228, 114-126. http://10.1016/j.pepi.2013.12.010

- Santos, S. S. M., Marcondes, M. L., Justo, J. F., & Assali, L. V. C. (2019). Stability of calcium and magnesium carbonates at Earth's lower mantle thermodynamic conditions. *Earth and Planetary Science Letters*, 506, 1-7. http://10.1016/j.epsl.2018.10.030
- Santos, S. S. M., Marcondes, M. L., Justo, J. F., & Assali, L. V. C. (2020). Calcium carbonate at high pressures and high temperatures: A first-principles investigation. *Physics of the Earth and Planetary Interiors*, 299, 106327. http://10.1016/j.pepi.2019.106327
- Sata, N., Hirose, K., Shen, G., Nakajima, Y., Ohishi, Y., & Hirao, N. (2010). Compression of FeSi, Fe₃C, Fe_{0.95}O, and FeS under the core pressures and implication for light element in the Earth's core. *Journal of Geophysical Research*, 115(B9). http://10.1029/2009jb006975
- Scott, H. P., Huggins, S., Frank, M. R., Maglio, S. J., Martin, C. D., Meng, Y., et al. (2007). Equation of state and high-pressure stability of Fe₃P-schreibersite: Implications for phosphorus storage in planetary cores. *Geophysical Research Letters*, 34(6). http://10.1029/2006gl029160
- Seagle, C. T., Campbell, A. J., Heinz, D. L., Shen, G., & Prakapenka, V. B. (2006). Thermal equation of state of Fe₃S and implications for sulfur in Earth's core. *Journal of Geophysical Research: Solid Earth*, 111(B6). http://10.1029/2005jb004091
- Seto, Y., Hamane, D., Nagai, T., & Fujino, K. (2008). Fate of carbonates within oceanic plates subducted to the lower mantle, and a possible mechanism of diamond formation. *Physics and Chemistry of Minerals*, 35(4), 223-229. http://10.1007/s00269-008-0215-9
- Seto, Y., Nishio-Hamane, D., Nagai, T., & Sata, N. (2010). Development of a software suite on X-ray diffraction experiments. *The Review of High Pressure Science and Technology*, 20(3), 269-276. http://10.4131/jshpreview.20.269
- Shahar, A., Driscoll, P., Weinberger, A., & Cody, G. (2019). What makes a planet habitable? *Science*, 364(6439), 434-435.
- Shahar, A., Schauble, E. A., Caracas, R., Gleason, A. E., Reagan, M. M., Xiao, Y., et al. (2016). Pressure-dependent isotopic composition of iron alloys. *Science*, *352*(6285), 580-582. http://10.1126/science.aad9945
- Shen, G., Lin, J. F., Fei, Y., Mao, H. K., Hu, M., & Chow, P. (2003). Magnetic and structural transition in Fe₃S at high pressures. *Eos Trans. AGU*, 84(46), F1548-F1549.
- Shi, Y.-J., Du, Y.-L., & Chen, G. (2013). First-principles study on the elastic and electronic properties of hexagonal ε-Fe₃N. *Computational Materials Science*, 67, 341-345. http://10.1016/j.commatsci.2012.09.012
- Shilobreeva, S., Martinez, I., Busigny, V., Agrinier, P., & Laverne, C. (2011). Insights into C and H storage in the altered oceanic crust: Results from ODP/IODP Hole 1256D. *Geochimica et Cosmochimica Acta*, 75(9), 2237-2255. http://10.1016/j.gca.2010.11.027

- Shirey, S. B., Cartigny, P., Frost, D. J., Keshav, S., Nestola, F., Nimis, P., et al. (2013). Diamonds and the Geology of Mantle Carbon. *Carbon in Earth*, 75(1), 355-421. http://10.2138/rmg.2013.75.12
- Sifkovits, M., Smolinski, H., Hellwig, S., & Weber, W. (1999). Interplay of chemical bonding and magnetism in Fe₄N, Fe₃N and zeta-Fe₂N. *Journal of Magnetism and Magnetic Materials*, 204(3), 191-198. http://10.1016/S0304-8853(99)00296-6
- Smith, D., Lawler, K. V., Martinez-Canales, M., Daykin, A. W., Fussell, Z., Smith, G. A., et al. (2018). Postaragonite phases of CaCO₃ at lower mantle pressures. *Physical Review Materials*, 2(1). http://10.1103/PhysRevMaterials.2.013605
- Solopova, N. A., Dubrovinsky, L., Spivak, A. V., Litvin, Y. A., & Dubrovinskaia, N. (2014). Melting and decomposition of MgCO₃ at pressures up to 84 GPa. *Physics and Chemistry of Minerals*, 42(1), 73-81. http://10.1007/s00269-014-0701-1
- Stachel, T., Aulbach, S., Brey, G. P., Harris, J. W., Leost, I., Tappert, R., & Viljoen, K. S. (2004). The trace element composition of silicate inclusions in diamonds: a review. *Lithos*, 77(1-4), 1-19. http://10.1016/j.lithos.2004.03.027
- Stachel, T., & Luth, R. W. (2015). Diamond formation Where, when and how? *Lithos*, 220-223, 200-220. http://10.1016/j.lithos.2015.01.028
- Stagno, V., Cerantola, V., Aulbach, S., Lobanov, S., McCammon, C. A., & Merlini, M. (2019). Carbon-Bearing Phases throughout Earth's Interior. In *Deep Carbon: Past to Present* (pp. 66-88): Cambridge University Press.
- Stagno, V., Ojwang, D. O., McCammon, C. A., & Frost, D. J. (2013). The oxidation state of the mantle and the extraction of carbon from Earth's interior. *Nature*, *493*(7430), 84-88. Article. http://10.1038/nature11679
- Staudigel, H. (2014). Chemical Fluxes from Hydrothermal Alteration of the Oceanic Crust. In *Treatise on Geochemistry* (pp. 583-606).
- Stevenson, D. J. (2001). Mars' core and magnetism. *Nature*, *412*(6843), 214-219. http://10.1038/35084155
- Stixrude, L., & Lithgow-Bertelloni, C. (2011). Thermodynamics of mantle minerals II. Phase equilibria. *Geophysical Journal International*, 184(3), 1180-1213. http://10.1111/j.1365-246X.2010.04890.x
- Sun, C., & Dasgupta, R. (2019). Slab—mantle interaction, carbon transport, and kimberlite generation in the deep upper mantle. *Earth and Planetary Science Letters*, 506, 38-52. http://10.1016/j.epsl.2018.10.028
- Syracuse, E. M., van Keken, P. E., & Abers, G. A. (2010). The global range of subduction zone thermal models. *Physics of the Earth and Planetary Interiors*, 183(1-2), 73-90. http://10.1016/j.pepi.2010.02.004

- Takemura, K., & Dewaele, A. (2008). Isothermal equation of state for gold with a He-pressure medium. *Physical Review B*, 78(10). http://10.1103/PhysRevB.78.104119
- Teng, F.-Z. (2017). Magnesium isotope geochemistry. *Reviews in Mineralogy and Geochemistry*, 82(1), 219-287.
- Teng, F.-Z., Li, W.-Y., Ke, S., Marty, B., Dauphas, N., Huang, S., et al. (2010). Magnesium isotopic composition of the Earth and chondrites. *Geochimica et Cosmochimica Acta*, 74(14), 4150-4166.
- Thompson, S., Komabayashi, T., Breton, H., Suehiro, S., Glazyrin, K., Pakhomova, A., & Ohishi, Y. (2020). Compression experiments to 126 GPa and 2500 K and thermal equation of state of Fe₃S: Implications for sulphur in the Earth's core. *Earth and Planetary Science Letters*, 534. http://10.1016/j.epsl.2020.116080
- Thomson, A. R., Kohn, S. C., Bulanova, G. P., Smith, C. B., Araujo, D., & Walter, M. J. (2016a). Trace element composition of silicate inclusions in sub-lithospheric diamonds from the Juina-5 kimberlite: Evidence for diamond growth from slab melts. *Lithos*, 265, 108-124. http://10.1016/j.lithos.2016.08.035
- Thomson, A. R., Walter, M. J., Kohn, S. C., & Brooker, R. A. (2016b). Slab melting as a barrier to deep carbon subduction. *Nature*, 529(7584), 76-79. Article. http://10.1038/nature16174
- Thomson, A. R., Walter, M. J., Lord, O. T., & Kohn, S. C. (2014). Experimental determination of melting in the systems enstatite-magnesite and magnesite-calcite from 15 to 80 GPa. *American Mineralogist*, 99(8-9), 1544-1554. http://10.2138/am.2014.4735
- Toby, B. H. (2001). EXPGUI, a graphical user interface for GSAS. *Journal of Applied Crystallography*, 34(2), 210-213. http://10.1107/S0021889801002242
- Tschauner, O., Huang, S., Greenberg, E., Prakapenka, V., Ma, C., Rossman, G., et al. (2018). Ice-VII inclusions in diamonds: Evidence for aqueous fluid in Earth's deep mantle. *Science*, 359(6380), 1136-1139.
- van Mierlo, W. L., Langenhorst, F., Frost, D. J., & Rubie, D. C. (2013). Stagnation of subducting slabs in the transition zone due to slow diffusion in majoritic garnet. *Nature Geoscience*, 6(5), 400-403. http://10.1038/ngeo1772
- Vocadlo, L., Brodholt, J., Dobson, D. P., Knight, K. S., Marshall, W. G., Price, G. D., & Wood, I. G. (2002). The effect of ferromagnetism on the equation of state of Fe₃C studied by first-principles calculations. *Earth and Planetary Science Letters*, 203(1), 567-575. http://10.1016/S0012-821x(02)00839-7
- Wang, S. J., Teng, F. Z., & Li, S. G. (2014). Tracing carbonate-silicate interaction during subduction using magnesium and oxygen isotopes. *Nat Commun*, *5*, 5328. Article. http://10.1038/ncomms6328

- Wang, Z., & Becker, H. (2013). Ratios of S, Se and Te in the silicate Earth require a volatile-rich late veneer. *Nature*, 499(7458), 328-331. http://10.1038/nature12285
- Wetzel, M. H., Schwarz, M. R., & Leineweber, A. (2019). High-pressure high-temperature study of the pressure induced decomposition of the iron nitride γ'-Fe₄N. *Journal of Alloys and Compounds*. http://10.1016/j.jallcom.2019.06.078
- Widenmeyer, M., Hansen, T. C., Meissner, E., & Niewa, R. (2014). Formation and decomposition of iron nitrides observed by in situ powder neutron diffraction and thermal analysis. *Zeitschrift fur Anorganische und Allgemeine Chemie*, 640(7), 1265-1274. http://10.1002/zaac.201300676
- Wirth, R., Kaminsky, F., Matsyuk, S., & Schreiber, A. (2009). Unusual micro- and nano-inclusions in diamonds from the Juina Area, Brazil. *Earth and Planetary Science Letters*, 286(1-2), 292-303. http://10.1016/j.epsl.2009.06.043
- Wombacher, F., Eisenhauer, A., Böhm, F., Gussone, N., Regenberg, M., Dullo, W.-C., & Rüggeberg, A. (2011). Magnesium stable isotope fractionation in marine biogenic calcite and aragonite. *Geochimica et Cosmochimica Acta*, 75(19), 5797-5818.
- Wood, B. J., Walter, M. J., & Wade, J. (2006). Accretion of the Earth and segregation of its core. *Nature*, *441*(7095), 825-833. http://10.1038/nature04763
- Workman, R. K., & Hart, S. R. (2005). Major and trace element composition of the depleted MORB mantle (DMM). *Earth and Planetary Science Letters*, 231(1-2), 53-72. http://10.1016/j.epsl.2004.12.005
- Wriedt, H., Gokcen, N., & Nafziger, R. (1987). The Fe-N (iron-nitrogen) system. *Bulletin of Alloy Phase Diagrams*, 8(4), 355-377.
- Yao, C., Wu, Z. Q., Zou, F., & Sun, W. D. (2018a). Thermodynamic and Elastic Properties of Magnesite at Mantle Conditions: First-Principles Calculations. *Geochemistry Geophysics Geosystems*, 19(8), 2719-2731. http://10.1029/2017gc007396
- Yao, X., Xie, C. W., Dong, X., Oganov, A. R., & Zeng, Q. F. (2018b). Novel high-pressure calcium carbonates. *Physical Review B*, 98(1). http://10.1103/PhysRevB.98.014108
- Ye, Y., Smyth, J. R., & Boni, P. (2012). Crystal structure and thermal expansion of aragonite-group carbonates by single-crystal X-ray diffraction. *American Mineralogist*, 97(4), 707-712. http://10.2138/am.2012.3923
- Yoder, C. F., Konopliv, A. S., Yuan, D. N., Standish, E. M., & Folkner, W. M. (2003). Fluid core size of Mars from detection of the solar tide. *Science*, 300(5617), 299-303. http://10.1126/science.1079645
- Zedgenizov, D. A., & Litasov, K. D. (2017). Looking for "missing" nitrogen in the deep Earth. *American Mineralogist*, 102(9), 1769-1770.

- Zhang, W. H., Lv, Z. Q., Shi, Z. P., Sun, S. H., Wang, Z. H., & Fu, W. T. (2012). Electronic, magnetic and elastic properties of ε-phases Fe₃X(X=B, C, N) from density-functional theory calculations. *Journal of Magnetism and Magnetic Materials*, *324*(14), 2271-2276. http://10.1016/j.jmmm.2012.02.114
- Zhang, Z. G., Mao, Z., Liu, X., Zhang, Y. G., & Brodholt, J. (2018). Stability and Reactions of CaCO₃ Polymorphs in the Earth's Deep Mantle. *Journal of Geophysical Research-Solid Earth*, 123(8), 6491-6500. http://10.1029/2018jb015654
- Zhu, F., Li, J., Liu, J. C., Lai, X. J., Chen, B., & Meng, Y. (2019). Kinetic Control on the Depth Distribution of Superdeep Diamonds. *Geophysical Research Letters*, 46(4), 1984-1992. http://10.1029/2018gl080740